



รายงานวิจัยฉบับสมบูรณ์

โครงการการพัฒนาตัวเร่งปฏิกิริยาสำหรับปฏิกิริยาการเปลี่ยน คาร์บอนไดออกไซด์ให้เป็นผลิตภัณฑ์ที่เพิ่มมูลค่า

(Developments in potential catalyst for transformations of CO_2 into the valuable products)

โดย ศ.ดร. ศิริพร จึงสุทธิวงษ์

เมษายน 2565

สัญญาเลขที่ RSA6280055

รายงานวิจัยฉบับสมบูรณ์

โครงการการพัฒนาตัวเร่งปฏิกิริยาสำหรับปฏิกิริยาการเปลี่ยน คาร์บอนไดออกไซด์ให้เป็นผลิตภัณฑ์ที่เพิ่มมูลค่า

(Developments in potential catalyst for transformations of CO_2 into the valuable products)

ศ.ดร. ศิริพร จึงสุทธิวงษ์ มหาวิทยาลัยอุบลราชธานี

สนับสนุนโดยสำนักงานกองทุนสนับสนุนการวิจัย และมหาวิทยาลัยอุบลราชธานี

(ความเห็นในรายงานนี้เป็นของผู้วิจัย สกว. และต้นสังกัด ไม่จำเป็นต้องเห็นด้วยเสมอไป)

Abstract (บทคัดย่อ)

The impacts of climate change on Thailand include prolonged droughts, decreased agricultural and fishery yields, violent flooding, sea level rise and health-related issues are already serious and will likely create or exacerbate a number of additional problems during the next few decades. Greenhouse gases from human activities are the most significant driver of observed climate change since the mid-20th century. Recently, the Thai government has begun implementing interesting strategies to adapt to climate change, to mitigate some of the effects that are already felt across sectors, and to protect farmland, coasts and cities. Owing to the increasing emissions of direct greenhouse gas, CO₂ (carbon dioxide), human life and the ecological environment have been affected by global warming and climate changes. To mitigate the concentration of CO₂ in the atmosphere various strategies have been implemented such as separation, storage, and utilization of CO₂. In this work, the reaction mechanism of CO₂ hydrogenation to formic acid on the metal supported on carbon-based materials have been investigated by using a combined experimental and density functional theory approaches. We addressed the potential catalytic role in CO₂ hydrogenation reaction to formic acid following equation; $CO_2 + H_2 \rightarrow HCOOH$. The insights prevailed in this study will be substantially beneficial for the improvement of broad heterogeneous catalysts for CO₂ hydrogenation to valuable chemicals.

Project Code: RSA6280055

Project Title: Developments in potential catalyst for transformations of CO_2 into the valuable products (การพัฒนาตัวเร่งปฏิกิริยาสำหรับปฏิกิริยาการเปลี่ยนคาร์บอนไดออกไซด์ให้เป็น ผลิตภัณฑ์ที่เพิ่มมูลค่า)

Investigator: Prof. Siriporn Jungsuttiwong, Ubon Ratchathani University

E-mail Address: siriporn.j@ubu.ac.th

Project Period 3 years

Objectives

- 1. To study the structural and energetic properties of newly designed catalyst for CO_2 conversion using computational calculations.
- 2. To study the CO_2 hydrogenation mechanism on newly designed heterogeneous catalyst surface including reliable intermediate and transition-state structures along their pathways.
- 3. To identify the most preferable reaction path and the rate-determining step of CO_2 hydrogenation on the metal supported on carbon-based materials.

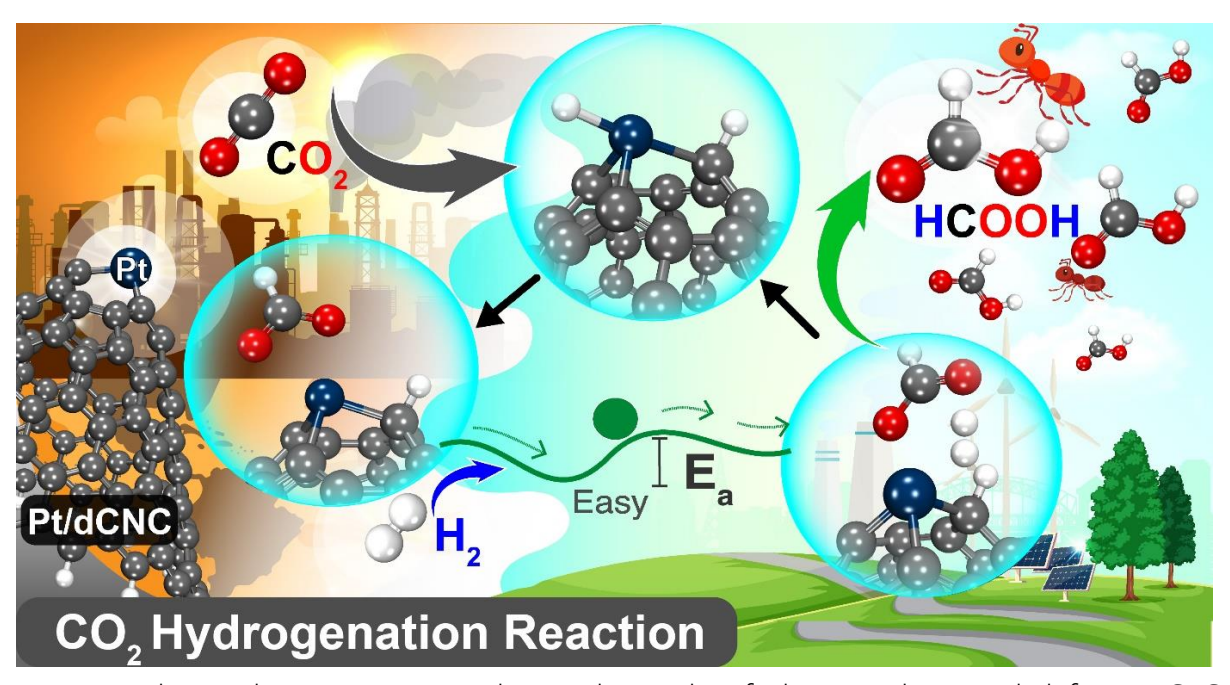
Computational study

Theoretical study using computation calculation will be performed in parallel with experimental work. The highly efficient catalytic route for CO_2 hydrogenation will be theoretically proposed. The insights prevailed in this study will be substantially beneficial for the improvement of various heterogeneous catalysts for CO_2 hydrogenation to valuable chemicals.

In this work, important reaction pathways along with comprehensive elementary step reactions and rate limiting steps will be identified. The insights prevailed in this study will be substantially beneficial for the improvement of various heterogeneous catalysts for CO_2 hydrogenation to formic acid. Herein, the reaction mechanism of CO_2 hydrogenation to formic acid on the metal supported on carbon-based materials by means of the density functional theory (DFT) has been investigated. The reaction mechanisms were proposed.

Results

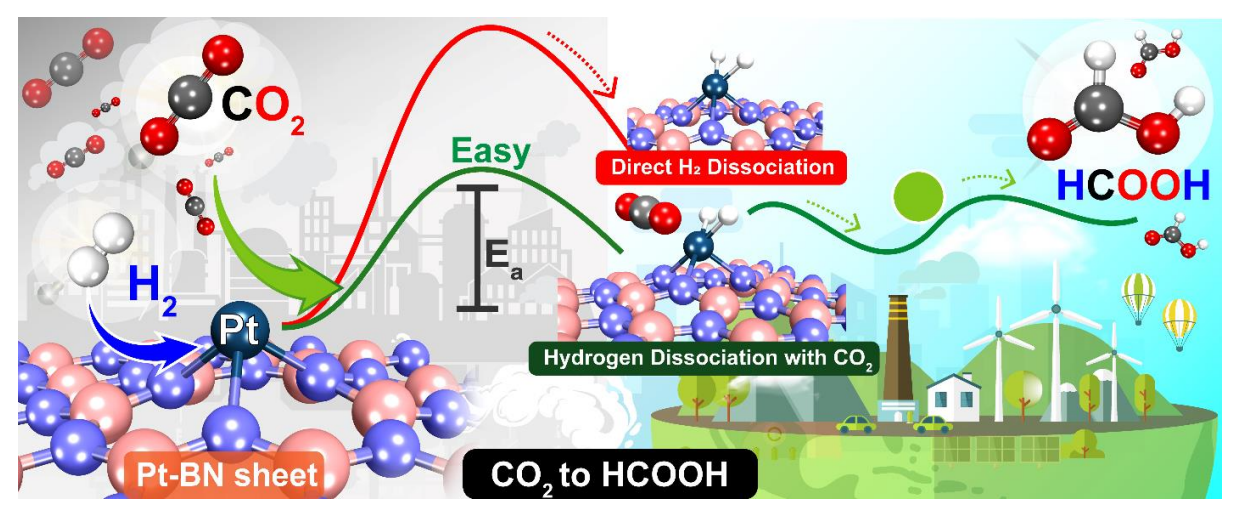
1. DFT Study of Catalytic CO_2 Hydrogenation over Pt-Decorated Carbon Nanocones: Combined H_2 Dissociation with Spillover Mechanism



In this work, we investigate the catalytic role of platinum-decorated defective CNC (Pt/dCNC) in CO₂ hydrogenation to formic acid (FA) by using a density functional theory (DFT) approach. The reaction follows the equation: $CO_{2(g)} + H_{2(g)} \longrightarrow HCOOH_{(g)}$. Combining highly reactive Pt atoms with defective CNC provides Pt/dCNC, a reactive mono-dispersed atomic catalyst for CO_2 hydrogenation. We propose our new mechanism of CO_2 hydrogenation over Pt/dCNC catalyst involving H_2 -dissociation and H-spillover sequence which is energetically favorable. The rate-determining step is formic acid desorption which required energy barrier of 1.11 eV. Furthermore, our findings show that the rate of FA production is dependent on H_2 concentration. Altogether, the theoretical results support the concept of spillover mechanism as a key role to promote CO_2 hydrogenation via a formate intermediate. These results improve our understanding about the mechanism involving H_2 -dissociation with H-spillover process and the catalytic reactions which are very important for the development of highly efficient catalysts for CO_2 conversion to FA.

Keyword: DFT; CO₂ Hydrogenation; Carbon nanocone; Formic acid

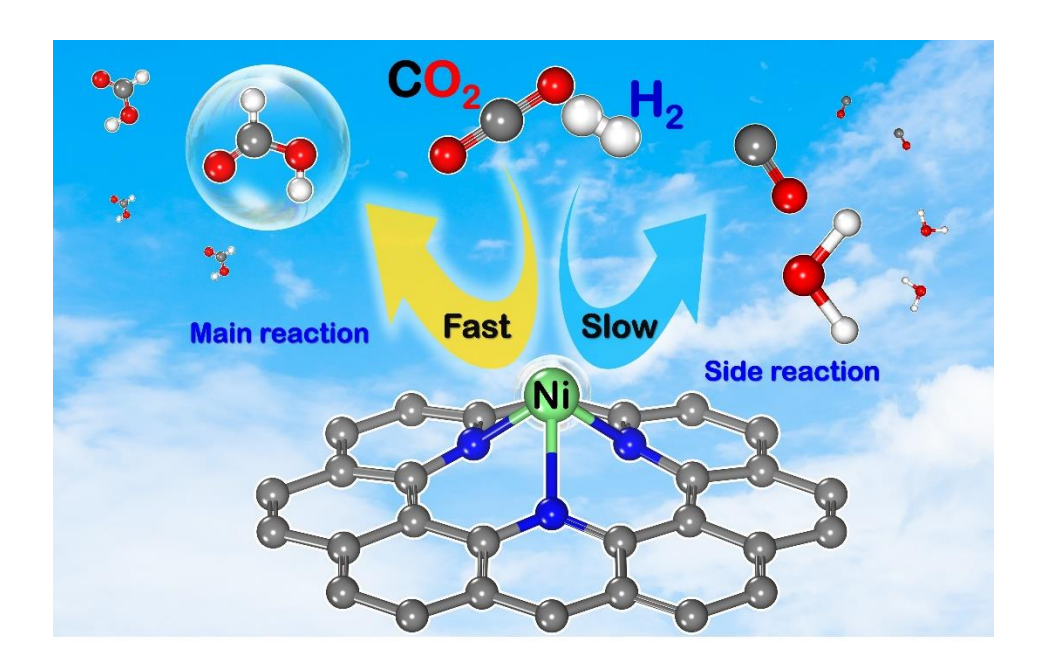
2. Theoretical insights into Catalytic CO₂ Hydrogenation over Single-atom (Fe or Ni) incorporated nitrogen-doped graphene



In this work, we investigated the mechanism of CO₂ hydrogenation over the Pt-doped boron nitride nanosheets (Pt-BNNSs) by using the density functional theory (DFT). It is found that a Pt adatom can be effectively stabilized in boron vacancy site (Pt-BV). Our investigation shows that the reaction mechanisms of CO₂ hydrogenation over Pt-BV can be found in three possible reaction pathways: (i) co-adsorption, (ii) H₂ dissociation, and (iii) co-adsorption together with H₂ dissociation pathways. The co-adsorption together with H₂ dissociation provides the most favorable pathway among of these three proposed mechanisms. The important finding of our study is that the presence of CO₂ in step of hydrogen dissociation plays an important role in producing the FA on the Pt-BV catalyst. Moreover, we found that the hydrogenation of CO₂ via carboxylate (COOH) has the rate-determining step of 0.63 eV in the step of hydrogen dissociation. In addition, the microkinetic modelling suggests that the COOH route is found to be more energetically and kinetically feasible rather than that it is formate route (HCOO) with the reaction temperature at 350 K and pressure of 5 bar. Our calculation results provide an important information for developing Pt-BV catalysts and might shed light on experimental design the novel Pt-BV catalyst for the CO₂ hydrogenation and the conversion of greenhouse gases into value-added products.

Keyword: DFT; CO₂ Hydrogenation; Pt-Boron nitride nanosheets; Formic acid

3. Theoretical insights into Catalytic CO₂ Hydrogenation over Single-atom (Fe or Ni) incorporated nitrogen-doped graphene



Developing highly efficient and cheap catalysts for the CO₂ hydrogenation is the key to achieve CO₂ conversion into clean energy. Herein, periodic density functional theory (DFT) calculations are performed to investigate possible reaction mechanisms for the hydrogenation of CO₂ to formic acid (cis- or trans-HCOOH) product over a single Fe or Ni atom incorporated nitrogen-doped graphene (Fe-N3Gr or Ni-N3Gr) sheets. Our calculations found that the CO₂ hydrogenation proceeds via a coadsorption mechanism to produce cis- or trans-HCOOH over Fe-N3Gr and Ni-N3Gr surfaces, which is classified into 2 steps: (1) the CO₂ hydrogenation to form a formate (HCOO*) intermediate and (2) hydrogen abstraction to produce cis- or trans-HCOOH. The formation of trans-HCOOH over both Fe-N3Gr and Ni-N3Gr surfaces exhibit the obvious superiority due to the low barrier all through the whole channel. The highest energy barriers (E_a) in the case of trans-HCOOH formation on Fe-N3Gr and Ni-N3Gr surfaces are only 0.57 and 0.37 eV, respectively, which indicated that the CO₂ hydrogenation to trans-HCOOH could be realized over these catalysts at low temperatures, especially the Ni-N3Gr surface. On the other hand, our findings show that the competitive reaction that produces CO and H₂O is almost impossible or extremely difficult to proceeds under ambient conditions due to the large E_a for the formation of these side products. Moreover, the microkinetic modeling of the CO₂ hydrogenation on both surfaces was investigated to confirm these results. Thus, the Fe-N3Gr and Ni-N3Gr catalysts reveal excellent catalytic activity and highly selective for CO₂ hydrogenation to trans-HCOOH. This theoretical investigation not only provides a promising catalyst but also gives a deeper understanding of CO₂ hydrogenation reaction.

Keywords: DFT; CO2 Hydrogenation; nitrogen-doped graphene; Formic acid

Outputs

- (1) Yodsin, N.; Rungnim, C.; Tungkamani, S.; Promarak, V.; Namuangruk, S. and Jungsuttiwong, S. DFT Study of Catalytic CO₂ Hydrogenation over Pt-Decorated Carbon Nanocones: H₂ Dissociation Combined with the Spillover Mechanism, **The Journal of Physical Chemistry C**, 2020, 124, 3, 1941-1949. **(Q1, เอกสารแนบ 1)**
- (2) Poldorn, P.; wongnongwa, Y.; Mudchimo, T. and Jungsuttiwong, S. Theoretical insights into Catalytic CO₂ Hydrogenation over Single-atom (Fe or Ni) incorporated nitrogen-doped graphene, Journal of CO₂ Utilization, 48 (2021) 101532. (Tier1, เอกสารแนบ 2)
- (3) Injongkol, Y.; Intayot, R.; Yodsin, N.; Montoya, A. and Jungsuttiwong. S. Mechanistic insight into Catalytic Carbon Dioxide Hydrogenation to Formic Acid over Pt doped Boron Nitride Nanosheets, Submitted to Molecular Catalysis, 2021, 510, 111675. (Q1, เอกสารแนบ 3)

pubs.acs.org/JPCC Article

DFT Study of Catalytic CO₂ Hydrogenation over Pt-Decorated Carbon Nanocones: H₂ Dissociation Combined with the Spillover Mechanism

Nuttapon Yodsin, Chompoonut Rungnim,* Sabaithip Tungkamani, Vinich Promarak, Supawadee Namuangruk, and Siriporn Jungsuttiwong*



Cite This: J. Phys. Chem. C 2020, 124, 1941–1949



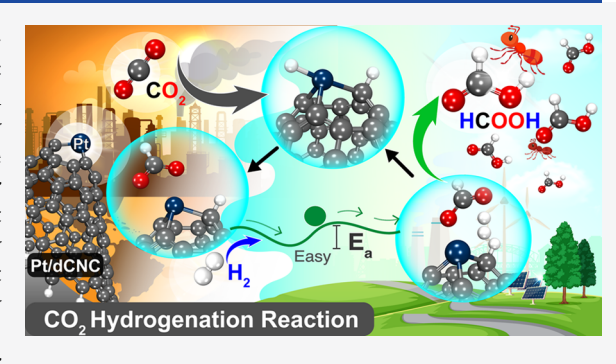
ACCESS

Metrics & More

Article Recommendations

s Supporting Information

ABSTRACT: In this work, we investigate the catalytic role of platinum-decorated defective CNC (Pt/dCNC) in CO₂ hydrogenation to formic acid (FA) by a density functional theory (DFT) approach. The reaction follows the equation $CO_{2(g)} + H_{2(g)} \rightarrow HCOOH_{(g)}$. Combining highly reactive Pt atoms with defective CNC provides Pt/dCNC, a reactive monodispersed atomic catalyst for CO_2 hydrogenation. We propose our new mechanism of CO_2 hydrogenation over the Pt/dCNC catalyst involving a H_2 dissociation and H spillover sequence that is energetically favorable. The rate-determining step is formic acid desorption that requires an energy barrier of 1.11 eV. Furthermore, our findings show that the rate of FA production is dependent on H_2 concentration. Altogether, the theoretical results support the concept of the spillover



mechanism, playing a key role in promoting CO₂ hydrogenation via a formate intermediate. These results improve our understanding of the mechanism involving H₂ dissociation with the H spillover process and the catalytic reactions that are very important for the development of highly efficient catalysts for CO₂ conversion into FA.

1. INTRODUCTION

Increased population size, continuous and rapid development of cities, industrial activities, and transportation all contribute to global CO2 production and have resulted in elevated levels of greenhouse gases in the earth's atmosphere. Most of the current energy production worldwide still comes from fossil fuels such as coal, crude oil, gasoline, and natural gas. The main disadvantages of these fossil fuels are emission of toxic gases, air and water pollution, and toxic waste, and these factors are the principal contributors to global warming and climate change. Carbon dioxide (CO₂) is the predominant greenhouse gas, and this situation must be resolved immediately. Novel technologies have been developed to address atmospheric CO₂ concentration, including carbon capture storage (CCS) and carbon capture utilization (CCU) by conversion into a value-added product. The most important challenge for the CCU process is to find active and costeffective catalysts. Therefore, much effort has been spent on the design and development of new inexpensive catalysts that offer high stability and efficiency for CO2 conversion into valuable products, such as the new proposed mechanism of CO₂ hydrogenation to formic acid (FA), methane, and methanol. Hence, a key benefit of CO₂ conversion is not only to decrease the amount of the greenhouse gas in the atmosphere but also to reduce fossil fuel utilization by the petrochemical industry.

Formic acid (FA) is widely used as a principle reagent for chemical applications, and it has numerous industrial applications. ¹⁻⁶ Many experimental and theoretical studies have investigated CO₂ conversion into FA.⁷⁻²⁴ Catalytic materials for CO₂ hydrogenation into FA are generally highly toxic and expensive and offer low efficiencies for CO₂ conversion. ^{1,9,17,25} Therefore, it is highly desirable to explore and develop a more cost-effective catalyst for CO₂ conversion into FA

Here, we are interested in identifying a carbon-based nanomaterial as a catalytic support because of its advantages such as low cost, high purity, and a large surface area. Carbon nanocones (CNCs) are a novel form of carbon that could provide a suitable support for various metals to form new carbon—metal nanocomposites. These materials could be used in several applications, including supercapacitors, drug delivery, lithium-ion batteries, biofuel cells, energy conversion and storage, and solar cells. CNC use as a new substrate for CCU applications has attracted a great deal of interest over recent years. Therefore, we chose to

Received: September 16, 2019 Revised: December 20, 2019 Published: December 26, 2019



investigate CNCs for use in the catalytic conversion of CO_2 into FA. CNCs offer many advantages, but they are inert and their efficiency is too low for use in catalytic CO_2 hydrogenation. Therefore, we considered decorating the nanomaterial surface with a transition metal coating to enhance CO_2 conversion into FA.

More than 10 years after the first report on carbon nanohorns,²⁷ it became possible to produce high-purity single-walled carbon nanohorns (SWCNHs) directly by pulsed arc-discharge methods to produce materials.³⁸ From the synthesis, the researchers found that the arc-discharge method can synthesize SWNHs with greater than 90% purity. For CO₂ hydrogenation, there are many transition-metal-based materials that can catalyze the reaction on the metal surface, such as from the group 11 elements. 39-42 In an experimental study, the Cu metal surface catalyzed the conversion of CO2 into FA.^{39,41-43} Because of the difficulty in determining reaction mechanisms and the effects of supports, theoretical calculations can help to understand fundamental processes, the structures of reactants, and transition state configurations along the catalytic path. For example, the mechanism of copper-catalyzed CO₂ hydrogenation was determined by performing density functional theory (DFT) calculations. 43 Metal catalysts are generally toxic and relatively expensive. However, one theoretical study reported reducing the amount of copper required for catalysis by depositing atomic copper onto an MOF-5 organic linker to catalyze CO2 hydrogenation and produce FA.11 Sirijaraensre and Limtrakul,14 Esrafili,8 and Nguyen¹³ each showed that a carbon-based catalyst could efficiently catalyze the hydrogenation of CO2 into FA. Moreover, experimental and theoretical studies of other metals were also considered and Pt and Ni metal surfaces were investigated for their CO₂ hydrogenation properties. 9,25,44 In 2017, to reduce the costs associated with using pure metals, researchers developed Pt- and Ni-doped defective graphene for CO₂ hydrogenation into FA.⁸ Interestingly, in 2018, Pt nanoparticle-loaded carbon nanohorns (Pt/CNHs) were synthesized by FA as a reducing agent under mild conditions. Compared with commercial Pt/C, the small size of Pt nanoparticles on Pt/CNH nanocomposites showed improved catalytic activity, electrocatalytic activity, and durability in FA oxidation reactions, when compared with those of Pt/C nanomaterials.³⁶ Recently, Melchionna successfully synthesized inorganic Pd@TiO2/carbon nanohorn electrocatalysts to directly convert CO₂ into FA, at thermodynamic equilibrium.²¹ Their study demonstrated that CNHs can be used with transition metals to provide catalytic support materials for hydrogenation of CO₂ into FA.

In this work, we used DFT calculations to investigate the adsorption of CO_2 and its subsequent hydrogenation reduction into FA over Pt-doped defective CNC (Pt/dCNC). We have reported on the geometry, electronic structure, and catalytic activity of Pt/dCNC materials and compare these with other reported carbon-based materials in detail. To the best of our knowledge, this is the first report on the hydrogenation of CO_2 into FA over Pt/dCNC. Our modeled results illustrate how the CNC spillover mechanism can be helpful for increasing the number of active Pt/dCNC sites. The results of this study help to clarify the chemical and catalytic properties of metal-doped dCNC materials and will aid in the design of highly efficient carbon-based catalysts for the conversion of CO_2 to useful chemicals. As a consequence, this study could be helpful in protecting the environment globally.

2. COMPUTATIONAL METHODOLOGY

All DFT calculations were performed using the Gaussian 09 program package. Geometry optimization and frequency calculations were performed for all complexes using Becke's three-parameter gradient-corrected exchange potential, combined with the Lee–Yang–Parr gradient-corrected correlation potential (B3LYP).^{45–47} In DFT calculations, all atoms were calculated using the 6-31G(d,p) basis set, except for the Pt atom for which we used the LANL2DZ basis set. Energies of all structures were corrected by single-point calculation using the B3LYP functional, including Grimme's D3 dispersion correction (B3LYP-D3)⁴⁸ with the 6-311G(d,p) basis set for C, O, and H atoms and the cc-pVTZ-PP basis set for the Pt atom.

In this work, the CNC cluster model consists of 112 carbon atoms with four pentagonal rings at the cone tip and terminating hydrogen atoms at the cone edge, as suggested in our previous report. Comparing C atoms at the cone tip and the sidewall, defective carbon nanocone complexes (dCNC) were preferably created by removing one carbon atom from the cone tip because the tip site has the strongest reactivity with Pt atom. This result corresponds to the CNC curvature effect suggested from a high pyramidalization angle $(\theta_{\rm P})$ of the C atom that has been found in our previous work. We then placed a Pt atom at only the cone tip resulting vacancy to create the Pt/dCNC substrate. The stability of the Pt atom on the dCNC support was calculated using the equation

$$E_{\rm bind} = E_{\rm Pt/dCNC} - E_{\rm Pt} - E_{\rm dCNC}$$

where $E_{\rm Pt/dCNC}$, $E_{\rm Pt}$ and $E_{\rm dCNC}$ are the total energies of Pt/dCNC, the Pt atom (Pt), and the dCNC substrate, respectively.

Gas adsorption on Pt/dCNC was determined via adsorption energy (E_{ads}) calculations using the equation

$$E_{\rm ads} = E_{\rm gas-Pt/dCNC} - E_{\rm Pt/dCNC} - E_{\rm gas}$$

where $E_{\rm gas-Pt/dCNC}$, $E_{\rm Pt/dCNC}$, and $E_{\rm gas}$ correspond to total energies of the adsorbed gas over Pt/dCNC, the bare Pt/dCNC, and the isolated gas, respectively.

We propose three plausible mechanisms for the CO_2 hydrogenation mechanism over Pt/dCNC. The transition state for each step was confirmed by frequency calculations, which show only one imaginary frequency. The activation energy (E_a) for each step is defined as

$$E_{\rm a} = E_{\rm transition} - E_{\rm reactant}$$

where $E_{\rm transition}$ and $E_{\rm reactant}$ represent total energies of the transition state and the reactant prior to the formation of the transition state, respectively.

3. RESULTS AND DISCUSSION

To understand the catalytic properties of the Pt/dCNC material, we investigated the electronic, structural, and thermodynamic properties of Pt/dCNC. From the optimized Pt/dCNC structure, the metal atom is located at a single vacancy site formed by pentagons of carbon atoms at the CNC cone. The metal forms covalent bonds with three neighboring carbon atoms (Figure S1). The binding energy between Pt and dCNC is approximately -7.12 eV, with a Pt-C bond length of around 1.9 Å, in accordance with our previously reported value. ^{34,49} Pt has a cohesive energy of 5.84 eV/atom, ⁵⁰ and the

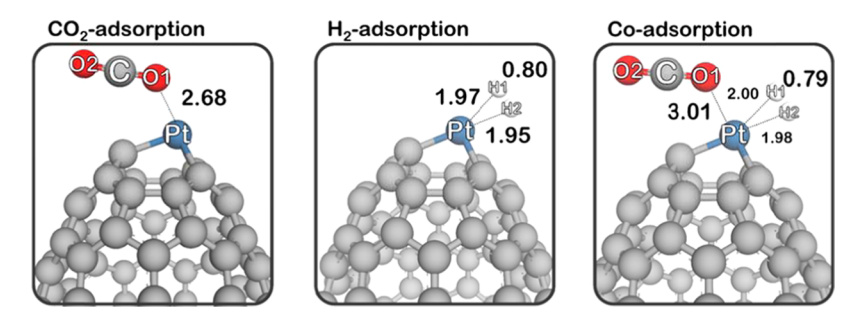


Figure 1. Optimized configurations for gas adsorption on the Pt/dCNC surface: CO_2 , H_2 , and CO_2/H_2 coadsorption complexes. Bond distances are in Å.

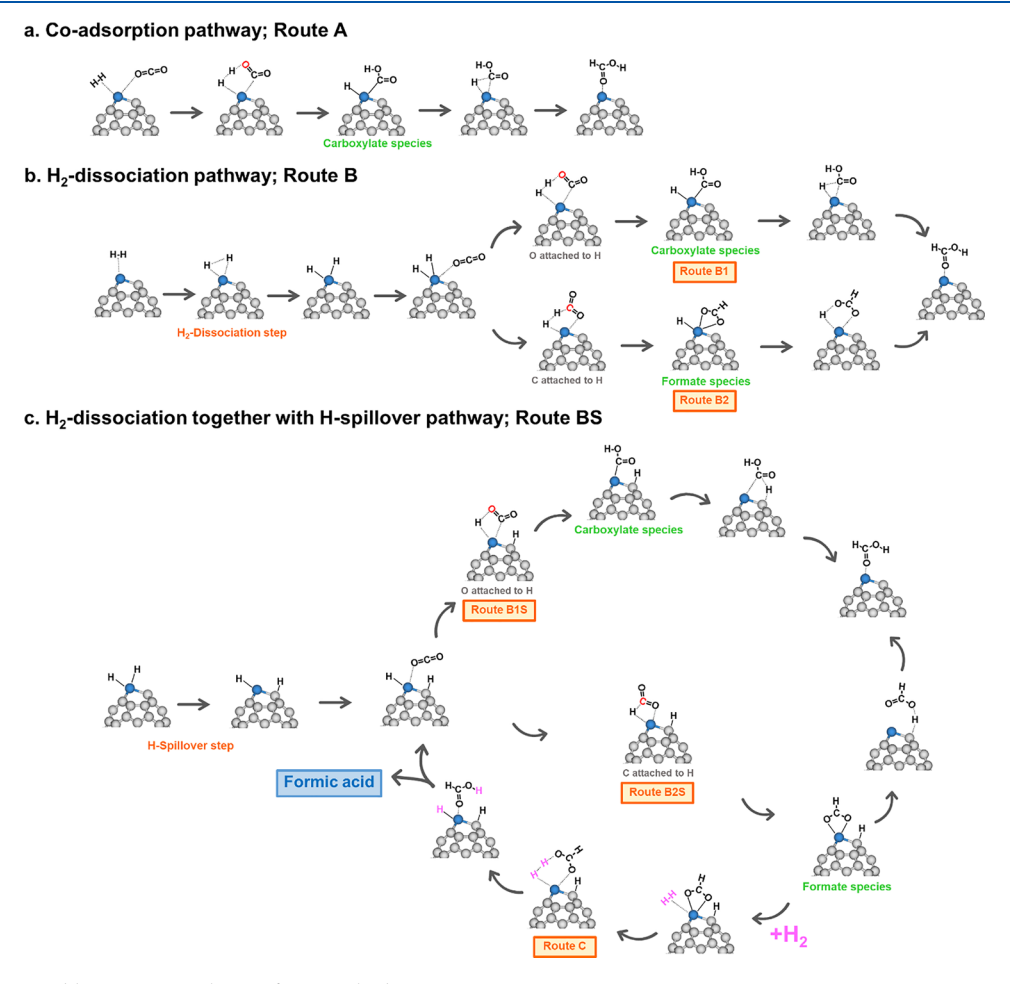


Figure 2. All three possible reaction pathways for CO₂ hydrogenation into FA.

strength of Pt binding at the vacancy site tends to prevent aggregation and formation of Pt metal clusters. According to a Mulliken charge population analysis, the Pt metal atom has a positive charge of 0.618e and the net charge on dCNC is negative (-0.271e, -0.306e, -0.306e), as a consequence of electron transfer from Pt to the carbon support. The reaction gases (H₂ and CO₂) are expected to be very attractive with a strong interaction because of the more positive charge on the Pt atom in the Pt/dCNC complex than that on the neutral Pt atom. Additionally, there is significant hybridization between Pt and dCNC in the lowest occupied molecular orbital (LUMO). More details are available in Figure S2 of the Supporting Information. Thus, the Pt atom behaves like a Lewis acid and it is expected to interact strongly with CO₂ during hydrogenation.

3.1. Adsorption of CO_2 and H_2 Molecules on Pt/dCNC. Here, we focus on the adsorption of CO_2 and H_2 onto Pt/dCNC and discuss possible catalytic mechanisms for hydrogenation of CO_2 to form FA.

To understand the mechanism of CO₂ conversion into FA, we first consider the adsorption of individual CO₂ and H₂ molecules onto the Pt/dCNC surface by varying the position and orientation of the two molecules to find the most stable adsorption mode. Figure 1 shows the most energetically favorable configurations for CO₂, H₂, and coadsorbed CO₂ and H₂.

The adsorption energy for CO_2 on Pt/dCNC is -0.40 eV, which is greater than that for adsorption on the perfect CNC surface (-0.13 eV). Additionally, the Pt-O intermolecular bond distance is approximately 2.68 Å (Figure 1). The CO_2

adsorption energy on Pt/dCNC is slightly greater than that with Pt-decorated single-vacancy graphene, which has different published $E_{\rm ads}$ values of -0.33^8 and -0.23 eV.⁵¹ The H₂ adsorption energy on Pt in Pt/dCNC is equal to -0.44 eV and is therefore more favorable than CO₂ binding to the catalyst.

We also investigated the coadsorption of H_2 and CO_2 gas molecules. Figure 1 shows how CO_2 and H_2 can coadsorb onto Pt/dCNC but the Pt–O and Pt–H bonds are slightly weaker than those for individual adsorption modes. The Pt–O bond distance in the coadsorption mode is lengthened by 0.33 Å (from 2.68 to 3.01 Å). The CO_2 and H_2 adsorption energies are -0.28 and -0.38 eV, respectively, implying that both gas molecules can cover the metal surface when exposed to a CO_2/H_2 reaction mixture. To confirm gas adsorption, we analyzed the gas–Pt/dCNC frontier orbitals. Figure S3 shows that hybridization between the adsorbate gases and the Pt/dCNC substrate is most similar in character to the Pt–O and Pt–H bonds, reflecting the strong interaction of Pt toward CO_2 and H_2 .

3.2. Reaction Mechanism of CO₂ Hydrogenation on the Pt/dCNC Surface. We propose a reaction mechanism for CO₂ hydrogenation into FA and investigate three possible reaction pathways (Figure 2): a coadsorption pathway (Route A), a hydrogen dissociation pathway (Route B), and a dissociation and spillover pathway (Route BS).

3.2.1. CO_2 Hydrogenation on the Pt/dCNC Surface via the CO_2 and H_2 Coadsorption Pathway. We propose a CO_2 hydrogenation reaction, via coadsorption Route A. Following the coadsorption of CO_2 and H_2 , CO_2 hydrogenation converts CO_2 molecules into FA through a carboxylate intermediate. Equations 1–3 outline this process

$$CO_2 + H_2 \cdots Pt/dCNC \rightarrow CO_2/H_2 \cdots Pt/dCNC$$
 (1)

$$CO_2/H_2 \cdots Pt/dCNC \rightarrow H - Pt - COOH/dCNC$$
 (2)

$$H - Pt - COOH/dCNC \rightarrow HCOOH \cdot \cdot \cdot Pt/dCNC$$
 (3)

Figure 3 shows the catalytic pathway and optimized structures for Route A. At the first transition state (TS1-Route A), CO₂ is hydrogenated at oxygen O1 to generate a -COOH ligand (carboxylate intermediate). At the same time, a hydrogen molecule dissociates and the bond distance between H1 and H2 lengthens from 0.79 to 0.95 Å. The H1 atom is located between O1 on CO₂ and H2, at distances of 1.34 and 0.95 Å, respectively. The calculated activation energy barrier (E_a) for the formation of the carboxylic functional group (-COOH) is about 1.49 eV, with a single imaginary frequency of approximately -1425.17 cm⁻¹ (TS1-Route A). This E_a value is close to 1.50 eV for the Cu-deposited graphene surface, 14 but it is significantly less than the reaction on the Ni/graphene material⁸ (2.08 eV), calculated using similar DFT calculations. By following the TS1-Route A step, the carboxylate intermediate H-Pt-COOH (INT1-Route A) attains with a relative energy of around -0.69 eV. Next, H2 transfers from the Pt catalyst to the -COOH ligand via the TS2-Route A transition state, with an energy barrier of 0.78 eV and a single imaginary frequency of -559.23 cm⁻¹. At TS2-Route A, the distance between the carboxyl carbon atom and H2 decreases as HCOOH forms on the Pt/dCNC surface. Finally, FA is produced on the Pt/dCNC complex with an adsorption energy of -0.95 eV. Remarkably, the rate-determining step for the CO₂ and H₂ coadsorption pathway is the formation of the carboxylate intermediate at TS1-Route A (Figure 3). More-

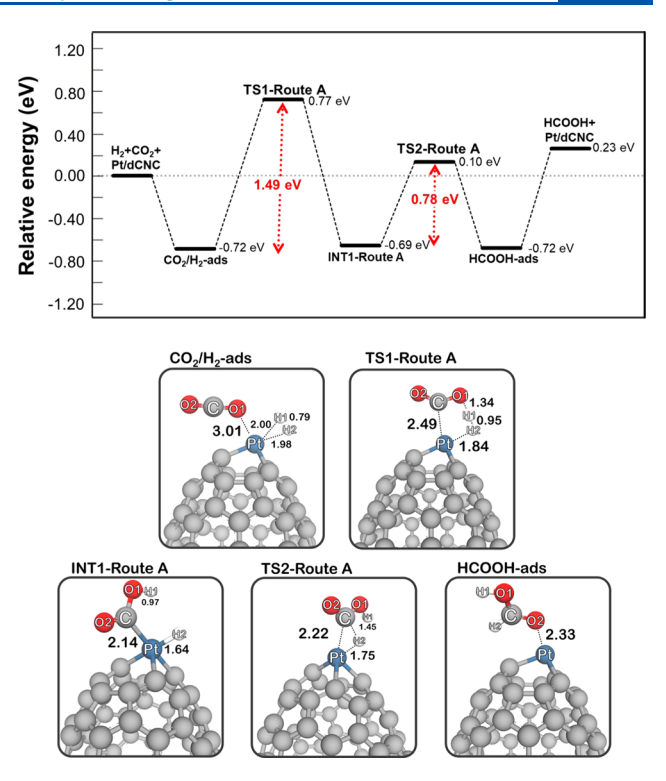


Figure 3. Catalytic reaction pathways (eV) for Pt/dCNC-catalyzed CO_2 hydrogenation into FA, via the CO_2 and H_2 coadsorption pathway (Route A). Distances are given in Å.

over, to elucidate the spin state of the deposited Pt atom on dCNC, we perform the catalytic reaction pathway for CO_2 hydrogenation over Pt/dCNC through the coadsorption pathway with different spin states of the decorated Pt atom. We found that the singlet state on the Pt atom over the dCNC material is the preferred reaction pathway (depicted in Figure S4). Then, the singlet state of the deposited Pt atom is selected for further study.

3.2.2. CO₂ Hydrogenation on the Pt/dCNC Surface via the H_2 Dissociation Pathway. The adsorption of H_2 on Pt/dCNC is slightly more favorable than the adsorption of CO₂. In addition, the H-H bond in the hydrogen molecule is a strong covalent bond with a bond-dissociation energy of 4.51 eV.¹ However, the bond can be easily dissociated on a Pt/dCNC complex with only a small energy barrier of 0.09 eV. Compared to hydrogen dissociation on other materials, the dissociation of H₂ molecules barely proceeds over Pt-Gr (0.29 eV) (Figure S7), Cu-Gr (1.31 eV), ¹⁴ or CoN₃-Gr (0.95 eV), ²⁰ which is in agreement with results of CO2 hydrogenation on other surfaces. 11,14,20,52 Hence, CO₂ hydrogenation either on the Pt/dCNC surface (Route A) or via a hydrogen dissociation pathway (Route B) might be favorable. We found that there are two possible pathways for Route B. The first involves a carboxylate intermediate (-COOH; Route B1), and the second occurs via a formate intermediate (-OOCH; Route B2). These proposed mechanisms are similar to CO₂ hydrogenation over Cu-alkoxide-functionalized MOFs, 11 alkali metal zeolites,⁵³ and Cu-doped graphene.¹⁴

$$H_2 + Pt/dCNC \rightarrow H - Pt - H/dCNC$$
 (4)

$$CO_2 + H - Pt - H/dCNC$$

 $\rightarrow CO_2 \cdots H - Pt - H/dCNC$ (5)

$$CO_2$$
···H - Pt - H/dCNC
 \rightarrow HOOC - Pt - H/dCNC(Route B1) (6.1)

$$CO_2$$
···H – Pt – H/dCNC

$$\rightarrow$$
 HCOO - Pt - H/dCNC(Route B2) (6.2)

$$HOOC - or HCOO - Pt - H/dCNC$$

$$\rightarrow$$
 HCOOH···Pt/dCNC (7)

Figure 4 shows an energy profile for CO₂ hydrogenation via Route B. The sequence begins with the adsorption of hydrogen

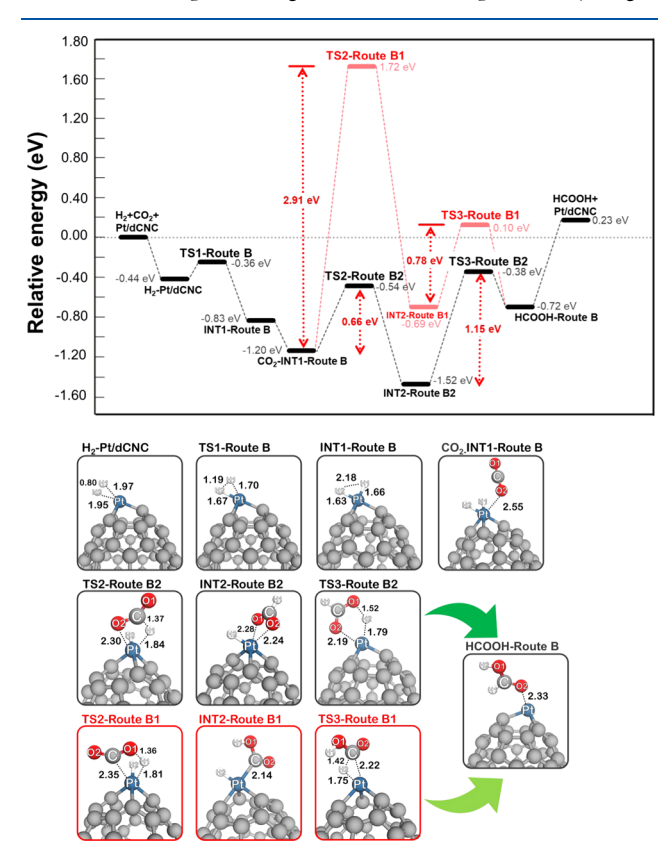


Figure 4. Energy profile showing optimized initial-state geometries, transition states, and the final state for CO_2 hydrogenation on the Pt/dCNC surface via the H_2 dissociation pathway (Route B). All distances are in Å.

gas onto the Pt atom on Pt/dCNC to form the initial state $(H_2-Pt/dCNC)$. Next, the molecule dissociates (TS1-Route B). This step has a very small energy barrier (0.09 eV) and a single imaginary frequency of -953.83 cm⁻¹. After the hydrogen dissociation step, the bond distance between the H_2 hydrogen atoms is significantly longer, lengthening from 0.80 in $H_2-Pt/dCNC$ to 2.18 Å at INT1-Route B. The adsorption of CO_2 onto platinum hydride on the CNC surface forms CO_2 -INT1-Route B.

Route B1 involves a carboxylate intermediate. The Pt-adsorbed CO_2 bends as it interacts with H1 to form a carboxylate species via TS2-Route B1. The formation of the transition state has a large energy barrier of 2.91 eV. Hydrogen H2 transfers from P1 to the carboxylate to form P1 -COOH via TS3-Route P1 with an activation energy of 0.78 eV. We confirmed intermediates TS2-Route P1 and TS3-Route P1 by

frequency analysis, using single imaginary frequencies for each transition state of -1765.73 and -559.23 cm⁻¹, respectively. From this result, hydrogenation of CO₂ on Pt/dCNC is unfavorable and barely proceeds via the carboxylate intermediate in a hydrogen dissociation pathway. The formation of the formate intermediate (-OOCH) has a small activation energy of 0.66 eV and forms via the TS2-Route B2 transition state. Frequency calculations reveal one imaginary frequency of -106.55 cm⁻¹ along the reaction coordinate. At the transition state, C-H1 forms spontaneously, with bond distances for C-H1 and Pt-H1 of approximately 1.37 and 1.84 Å, respectively. Finally, FA forms via TS3-Route B2, with an energy barrier of 1.15 eV. Thus, CO₂ hydrogenation over a Pt/dCNC catalyst via a formate intermediate is thermodynamically more favorable than it is with a carboxylate intermediate. This conclusion is in good agreement with the CO2 hydrogenation reaction on Faujasitesupported Ir₄ clusters.²³

3.2.3. CO₂ Hydrogenation Reaction on the Pt/dCNC Surface via H₂ Dissociation and with the H Spillover Pathway. Another pathway for CO₂ hydrogenation into FA over Pt/dCNC involves a hydrogen spillover mechanism, suggested in our previous work.³⁴ Following the introductory reaction step, proposed by Sirijaraensre and Limtrakul in 2016,¹⁴ CO₂ hydrogenation into FA over Pt/dCNC via a H₂-activated intermediate proceeds via the following steps

$$H_2 \cdots Pt/dCNC \rightarrow H - Pt/H - dCNC$$
 (8)

$$CO_2 + H - Pt/H - dCNC$$

$$\rightarrow CO_2 \cdots H - Pt/H - dCNC$$
 (9)

 CO_2 ···H - Pt/H - dCNC

$$\rightarrow$$
 HOOC - Pt/H - dCNC (Route B1S) (10.1)

 $CO_2 \cdots H - Pt/H - dCNC$

$$\rightarrow$$
 HCOO - Pt/H - dCNC (Route B2S) (10.2)

$$HOOC - or HCOO - Pt/H - dCNC$$

$$\rightarrow$$
 HCOOH···Pt/dCNC (11)

A hydrogen molecule dissociates over Pt/dCNC to generate a metal hydride (INT1-Route B), as described earlier. Following this dissociation step, we explored hydrogen spillover from the Pt atom to its three neighboring carbon atoms (Figure S5, C1, C2, and C3). From our calculations, the energy barriers for H spillover to the carbon atoms are 0.76 (C1), 0.92 (C2), and 0.92 eV (C3). Thus, we selected H spillover to C1 (TS2-Route BS) for further investigation. By comparison with Pt/dG, the activation energy of the H spillover step on Pt atom-deposited dG required a slightly high energy of approximately 0.95 eV, as demonstrated in Figure S7, as well as a very high energy barrier of around 2.721 eV of the H spillover over Pt₄ monocluster decorated on graphene. 54 After H spillover, a C-H bond forms on dCNC (INT2-Route BS). CO2 then adsorbs onto the complex to form CO₂-INT2-Route BS, with an adsorption energy of -0.45 eV.

For the formic reaction pathway, Route B2S, CO_2 hydrogenation occurs via a -OOCH intermediate. At the transition state (TS3-Route B2S), the Pt-H2 bond lengthens from 1.63 to 1.79 Å, as the hydrogen atom forms a covalent bond with the carbon atom on CO_2 . The activation energy for

the -OOCH formation is 0.64 eV. The single imaginary frequency for this transition state is -584.76 cm⁻¹. The formate intermediate INT3-Route B2S then forms from the transition state in a thermodynamically favorable step. Compared with CO_2 hydrogenation without a H spillover step, the activation energy for the formation of a formate intermediate decreases slightly, from 0.66 to 0.64 eV. Thus, the hydrogen spillover mechanism facilitates CO_2 hydrogenation.

Figure 5 and Table 1 provide further information on the adsorption properties of CO₂ gas. Considering the effect of

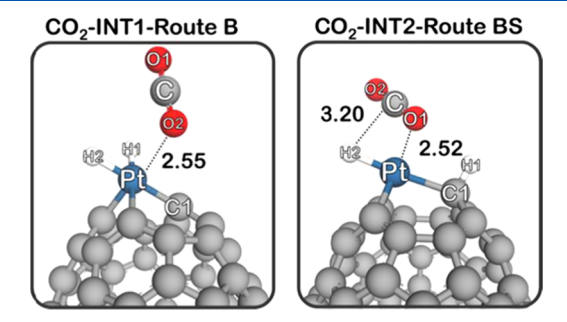


Figure 5. CO₂ adsorption properties on the Pt/dCNC surface, with and without hydrogen spillover. Distances are in Å.

Table 1. Effect of Hydrogen Spillover on CO₂ Adsorption^a

system	CO ₂ -INT1-Route B structure	CO ₂ -INT1-Route BS structure
$E_{\rm ads}$ (eV)	-0.37	-0.45
$E_{\rm a}~({\rm eV})$	0.66	0.64
d(Pt-O)	2.55	2.52
d(C-H)	2.99	3.20

^aDistances are in Å. Energy barrier for formate formation, E_a.

hydrogen spillover on CO_2 adsorption, the first hydrogen spillover onto the dCNC surface increases the CO_2 adsorption energy from -0.37 to -0.45 eV. The Pt-O bond distance is 2.52 Å (CO_2 -INT1-Route BS), while the Pt-O distance in CO_2 -INT1-Route B is slightly greater, being 2.55 Å. The strong interaction between an adsorbed gas and the substrate can reduce the energy barrier to the formation of the formate intermediate. We conclude that Pt/dCNC increases the number of active sites by spillover, displacing one hydrogen atom onto the CNC surface following hydrogen molecule dissociation during the CO_2 hydrogenation reaction.

At INT3-Route B2S, the formate intermediate arranges to a bidentate configuration to give Pt-O1 and Pt-O2 bond distances of 2.27 and 2.26 Å, respectively. The INT3-Route B2S formate species is quite stable, with a relative energy of -2.49 eV.

There are two possible pathways for the formation of the formate group (Figures 6–8). The first is FA formation via protonation from C–H1 on dCNC to an oxygen atom on the HCOO– group via TS4-Route B2S. The bond distance between H1 and C1 atoms on the surface lengthens from 1.10 to 1.55 Å. H1 bonds with O1 in –OOCH with a bond length of 1.14 Å. The transition state has an imaginary frequency of –949.95 cm $^{-1}$. The TS4-Route B2S transition step barrier is equal to 2.24 eV, and this step is the rate-determining step for CO2 hydrogenation in Route B2S.

To shorten the rate-determining step, we imagined a new pathway for FA formation by adding a second hydrogen

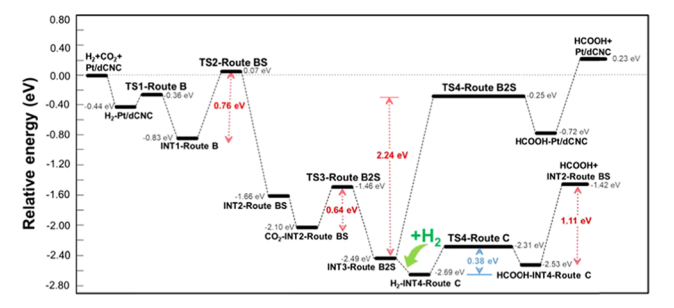


Figure 6. Energy profile (eV) for Pt/dCNC-catalyzed CO_2 hydrogenation into FA through the B2S and C pathways. Distances are in $^{\hat{\Lambda}}$

molecule (Route C), introducing the following sequence of reactions

$$H_2 + HCOO - Pt/H - dCNC$$

 $\rightarrow H_2 \cdots HCOO - Pt/H - dCNC$ (12)

$$H_2$$
···HCOO – Pt/H – dCNC
 \rightarrow HCOOH···H – Pt/H – dCNC (13)

Following hydrogen spillover and formation of the formate intermediate, the platinum atom becomes available for a second hydrogen molecule. Figure 8 shows that the second hydrogen molecule only adsorbs weakly to the -OOCH group on Pt/dCNC (-0.20 eV). In TS4-Route C, the H3-H4 bond length elongates from 0.75 to 0.90 Å, while intermolecular distances of H3-O1 and Pt-H4 decrease to 1.44 and 1.87 Å, respectively. These data confirm the dissociation of a second hydrogen molecule and the formation of FA. There is an associated imaginary frequency of -499.68 cm⁻¹ associated with transition state TS4-Route C, and Figure 6 reveals that the activation energy for this transition state is 0.38 eV. The energy barrier for TS4-Route C is much less than the calculated barrier for direct hydrogenation of formate on the Cu(111) surface $(E_a = 0.91 \text{ eV})$, over Cu-MOF-5 $(E_a = 0.79 \text{ eV})$ eV), 11 or over Cu-doped graphene $(E_a = 0.50 \text{ eV})$.

From these results, we suggest that FA production on Pt/ dCNC would occur following the second hydrogen dissociation on HCOO-Pt/dCNC, rather than by direct H-transfer from the hydrogenated dCNC surface (H1 atom). When FA is released, the catalytic component (H-Pt/H-dCNC) is similar to INT2-Route BS, which provides a catalytically active site for CO₂ hydrogenation into FA in its second cycle. Our results demonstrate that the rate of FA production is controlled by the quantity of H₂ available. At high H₂ pressures, the FA formation rate increases, as a result of the second H₂ dissociation that occurs via TS4-Route C, which requires an activation energy of only 0.38 eV. For the second cycle of FA production, the B2S rate-determining step is formic acid desorption, with an activation energy of 1.11 eV (Figure 2). From our calculated results, Pt/dCNC is an active catalyst for CO₂ hydrogenation into FA via the B2S reaction pathway.

4. CONCLUSIONS

The Pt-decorated, defective, 4-pentagon, carbon nanocone (Pt/dCNC) is a candidate catalytic material for CO_2 conversion into FA. We propose three possible reaction pathways for the catalytic hydrogenation of carbon dioxide, (a) a coadsorption pathway, (b) a H_2 dissociation pathway, and

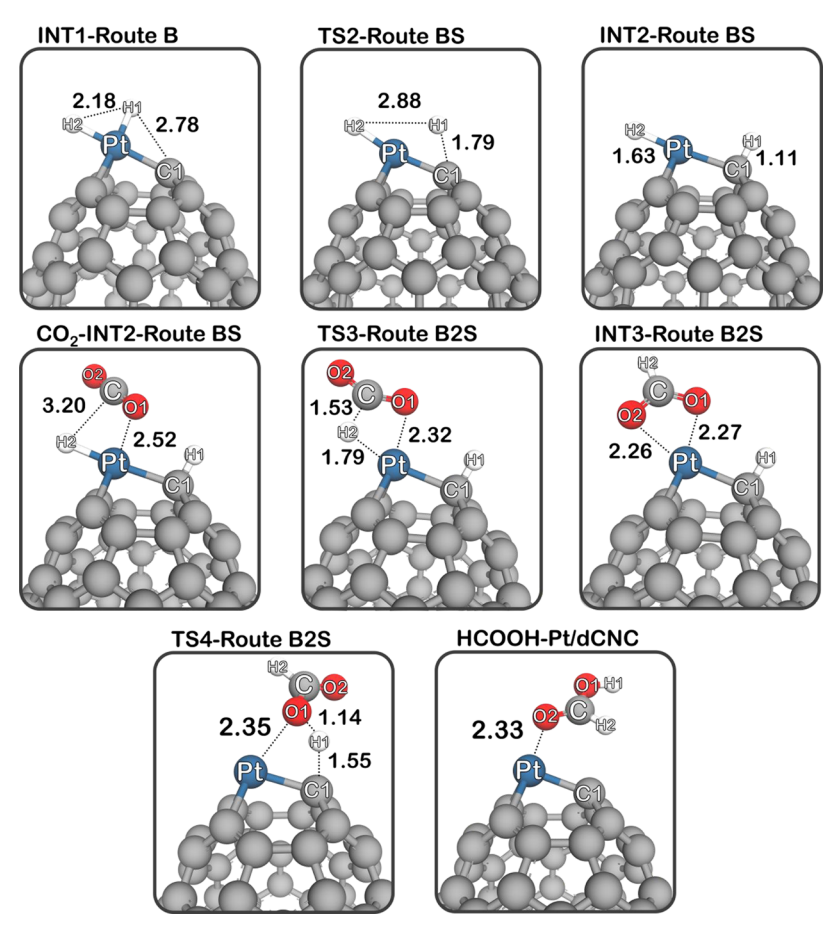


Figure 7. Structural properties during hydrogen dissociation and spillover on the Pt/dCNC composite during FA production via the BS route. Distances are in Å.

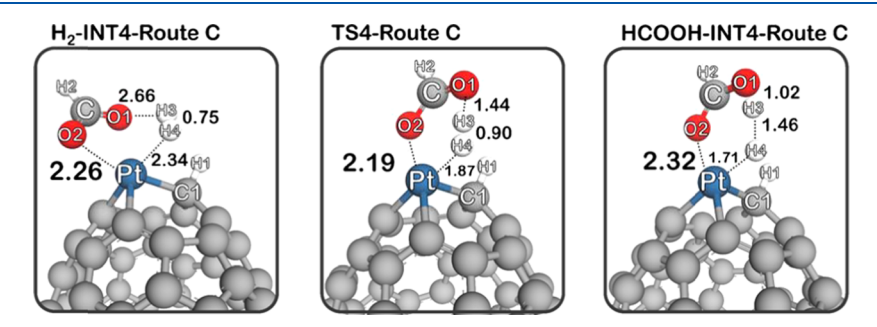


Figure 8. Sequential structural details during CO2 hydrogenation into FA over Pt/dCNC via Route C. Distances are given in Å.

(c) H₂ dissociation combined with a H spillover pathway. The "coadsorption pathway" shows a large energy barrier of 1.49 eV for carboxylate intermediate formation as the rate-determining step. Therefore, the "H2 dissociation pathway" has been investigated that requires a large activation energy of 1.15 eV for formic acid formation as the rate-determining step. Finally, our new mechanism "H2 dissociation combined with a H spillover pathway" has been proposed; the dissociated hydrogen atoms spillover on the carbon surface on dCNC, promoting CO₂ hydrogenation via a formate intermediate. Then, the introduction of a second hydrogen molecule significantly increases FA formation rates and the activation energy for this new pathway is only 0.38 eV. Taken together, Pt/dCNC catalyzes FA production by promoting hydrogen dissociation together with a hydrogen spillover mechanism. Our calculated results provide a very important guideline for

the development of highly efficient catalysts for CO₂ conversion into FA.

ASSOCIATED CONTENT

Supporting Information

The Supporting Information is available free of charge at https://pubs.acs.org/doi/10.1021/acs.jpcc.9b08776.

Optimized structures and atomic charges of the Pt/dCNC materials including frontier orbitals, as well as adsorption behavior of CO_2 , H_2 , and CO_2/H_2 adsorption onto the Pt/dCNC complex; energy profile and structural properties of the possible hydrogen spillover mechanism on the tip of the Pt/dCNC material; additional reaction barriers and energies of the related H_2 dissociation combined with the H spillover reaction; and CO_2 hydrogenation to formic

acid through the B2S and C pathways on the Pt/dG surface (PDF)

AUTHOR INFORMATION

Corresponding Authors

Chompoonut Rungnim — National Electronics and Computer Technology Center, Pathumthani, Thailand; Email: chompoonut.run@nectec.or.th

Siriporn Jungsuttiwong — Ubon Ratchathani University, Ubon Ratchathani, Thailand; ⊚ orcid.org/0000-0001-5943-6878; Email: siriporn.j@ubu.ac.th

Other Authors

Nuttapon Yodsin — Ubon Ratchathani University, Ubon Ratchathani, Thailand; orcid.org/0000-0002-7124-7815

Sabaithip Tungkamani – King Mongkut's University of Technology North Bangkok, Bangkok, Thailand

Vinich Promarak – Vidyasirimedhi Institute of Science and Technology, Rayong, Thailand

Supawadee Namuangruk – National Electronics and Computer Technology Center, Pathumthani, Thailand

Complete contact information is available at: https://pubs.acs.org/10.1021/acs.jpcc.9b08776

Notes

The authors declare no competing financial interest.

ACKNOWLEDGMENTS

The authors are grateful to the Department of Chemistry at Ubon Ratchathani University, Thailand Research Fund (RSA6280055 and RTA6080005), and the Human Resource Development in Science Project Science Achievement Scholarship of Thailand (SAST) for the financial support. The Center of Excellence for Innovation in Chemistry (PERCH-CIC), the office of the Higher Education Commission, and the Ministry of Education are gratefully acknowledged. The research has been also supported by Japan-ASEAN Science, Technology and Innovation Platform (JASTIP) and the National Nanotechnology Center (NANOTEC), Thailand. The authors also thank NSTDA Supercomputer Center (ThaiSC) for computing resources support.

REFERENCES

- (1) Álvarez, A.; Bansode, A.; Urakawa, A.; Bavykina, A. V.; Wezendonk, T. A.; Makkee, M.; Gascon, J.; Kapteijn, F. Challenges in the Greener Production of Formates/Formic Acid, Methanol, and DME by Heterogeneously Catalyzed CO₂ Hydrogenation Processes. *Chem. Rev.* **2017**, *117*, 9804–9838.
- (2) Jeong, K.-J.; Miesse, C. M.; Choi, J.-H.; Lee, J.; Han, J.; Yoon, S. P.; Nam, S. W.; Lim, T.-H.; Lee, T. G. Fuel crossover in direct formic acid fuel cells. *J. Power Sources* **2007**, *168*, 119–125.
- (3) Grasemann, M.; Laurenczy, G. Formic acid as a hydrogen source recent developments and future trends. *Energy Environ. Sci.* **2012**, *5*, 8171–8181.
- (4) Mellmann, D.; Sponholz, P.; Junge, H.; Beller, M. Formic acid as a hydrogen storage material development of homogeneous catalysts for selective hydrogen release. *Chem. Soc. Rev.* **2016**, *45*, 3954—3988.
- (5) Dong, Q.; Yin, T.; Wan, H.; Zhu, G.; Yu, G.; Guo, C. Self-assembly of Pd nanoparticles on anatase titanium dioxide and their application in formic acid fuel cells. *Int. J. Electrochem. Sci.* **2016**, *11*, 804

- (6) Hao, C.; Wang, S.; Li, M.; Kang, L.; Ma, X. Hydrogenation of CO_2 to formic acid on supported ruthenium catalysts. *Catal. Today* **2011**, *160*, 184–190.
- (7) Upadhyay, P.; Srivastava, V. Carbon Sequestration: Hydrogenation of CO₂ to Formic Acid. *Present Environ. Sustainable Dev.* **2016**. *10*. 13.
- (8) Esrafili, M. D.; Sharifi, F.; Dinparast, L. Catalytic hydrogenation of CO₂ over Pt- and Ni-doped graphene: A comparative DFT study. *J. Mol. Graphics Modell.* **2017**, *77*, 143–152.
- (9) Peng, G.; Sibener, S. J.; Schatz, G. C.; Ceyer, S. T.; Mavrikakis, M. CO₂ Hydrogenation to Formic Acid on Ni(111). *J. Phys. Chem. C* **2012**, *116*, 3001–3006.
- (10) Wu, S.-Y.; Ho, J.-J. Adsorption, Dissociation, and Hydrogenation of CO_2 on WC(0001) and WC-Co Alloy Surfaces Investigated with Theoretical Calculations. *J. Phys. Chem. C* **2012**, *116*, 13202-13209.
- (11) Maihom, T.; Wannakao, S.; Boekfa, B.; Limtrakul, J. Production of Formic Acid via Hydrogenation of CO₂ over a Copper-Alkoxide-Functionalized MOF: A Mechanistic Study. *J. Phys. Chem. C* **2013**, *117*, 17650–17658.
- (12) Moret, S.; Dyson, P. J.; Laurenczy, G. Direct synthesis of formic acid from carbon dioxide by hydrogenation in acidic media. *Nat. Commun.* **2014**, *5*, No. 4017.
- (13) Nguyen, L. T. M.; Park, H.; Banu, M.; Kim, J. Y.; Youn, D. H.; Magesh, G.; Kim, W. Y.; Lee, J. S. Catalytic CO₂ hydrogenation to formic acid over carbon nanotube-graphene supported PdNi alloy catalysts. *RSC Adv.* **2015**, *5*, 105560–105566.
- (14) Sirijaraensre, J.; Limtrakul, J. Hydrogenation of CO₂ to formic acid over a Cu-embedded graphene: A DFT study. *Appl. Surf. Sci.* **2016**, 364, 241–248.
- (15) Gassner, F.; Leitner, W. Hydrogenation of carbon dioxide to formic acid using water-soluble rhodium catalyststs. *J. Chem. Soc., Chem. Commun.* **1993**, 1465–1466.
- (16) Chorkendorff, I.; Taylor, P. A.; Rasmussen, P. B. Synthesis and hydrogenation of formate on Cu(100) at high pressures. *J. Vac. Sci. Technol., A* 1992, 10, 2277–2281.
- (17) Fujitani, T.; Choi, Y.; Sano, M.; Kushida, Y.; Nakamura, J. Scanning Tunneling Microscopy Study of Formate Species Synthesized from CO₂ Hydrogenation and Prepared by Adsorption of Formic Acid over Cu(111). *J. Phys. Chem. B* **2000**, *104*, 1235–1240.
- (18) Sredojević, D. N.; Šljivančanin, Ž.; Brothers, E. N.; Belić, M. R. Formic Acid Synthesis by CO₂ Hydrogenation over Single-Atom Catalysts Based on Ru and Cu Embedded in Graphene. *ChemistrySelect* **2018**, *3*, 2631–2637.
- (19) Thongnuam, W.; Maihom, T.; Choomwattana, S.; Injongkol, Y.; Boekfa, B.; Treesukol, P.; Limtrakul, J. Theoretical study of CO_2 hydrogenation into formic acid on Lewis acid zeolites. *Phys. Chem. Chem. Phys.* **2018**, 20, 25179–25185.
- (20) Esrafili, M. D.; Nejadebrahimi, B. Theoretical insights into hydrogenation of CO₂ to formic acid over a single Co atom incorporated nitrogen-doped graphene: A DFT study. *Appl. Surf. Sci.* **2019**, 475, 363–371.
- (21) Melchionna, M.; Bracamonte, M. V.; Giuliani, A.; Nasi, L.; Montini, T.; Tavagnacco, C.; Bonchio, M.; Fornasiero, P.; Prato, M. Pd@TiO2/carbon nanohorn electrocatalysts: reversible CO₂ hydrogenation to formic acid. *Energy Environ. Sci.* **2018**, *11*, 1571–1580.
- (22) Esrafili, M. D.; Dinparast, L. A DFT study on the catalytic hydrogenation of CO₂ to formic acid over Ti-doped graphene nanoflake. *Chem. Phys. Lett.* **2017**, *682*, 49–54.
- (23) Szyja, B. M.; Smykowski, D.; Szczygie, J.; Hensen, E. J. M.; Pidko, E. A. A DFT Study of CO₂ Hydrogenation on Faujasite-Supported Ir₄ Clusters: on the Role of Water for Selectivity Control. *ChemCatChem* **2016**, *8*, 2500–2507.
- (24) Motokura, K.; Kashiwame, D.; Miyaji, A.; Baba, T. Copper-Catalyzed Formic Acid Synthesis from CO₂ with Hydrosilanes and H₂O. Org. Lett. **2012**, *14*, 2642–2645.
- (25) Vesselli, E.; et al. Carbon Dioxide Hydrogenation on Ni(110). *J. Am. Chem. Soc.* **2008**, *130*, 11417–11422.

- (26) Karousis, N.; Suarez-Martinez, I.; Ewels, C. P.; Tagmatarchis, N. Structure, properties, functionalization, and applications of carbon nanohorns. *Chem. Rev.* **2016**, *116*, 4850–4883.
- (27) Harris, P. J.; Tsang, S. C.; Claridge, J. B.; Green, M. L. Highresolution electron microscopy studies of a microporous carbon produced by arc-evaporation. *J. Chem. Soc., Faraday Trans.* **1994**, *90*, 2799–2802.
- (28) Hiralal, P.; Wang, H.; Unalan, H. E.; Liu, Y.; Rouvala, M.; Wei, D.; Andrew, P.; Amaratunga, G. A. Enhanced supercapacitors from hierarchical carbon nanotube and nanohorn architectures. *J. Mater. Chem.* **2011**, *21*, 17810–17815.
- (29) Xu, J.; Yudasaka, M.; Kouraba, S.; Sekido, M.; Yamamoto, Y.; Iijima, S. Single wall carbon nanohorn as a drug carrier for controlled release. *Chem. Phys. Lett.* **2008**, *461*, 189–192.
- (30) Ajima, K.; Yudasaka, M.; Murakami, T.; Maigné, A.; Shiba, K.; Iijima, S. Carbon nanohorns as anticancer drug carriers. *Mol. Pharm.* **2005**, *2*, 475–480.
- (31) Yuge, R.; Tamura, N.; Manako, T.; Nakano, K.; Nakahara, K. High-rate charge/discharge properties of Li-ion battery using carbon-coated composites of graphites, vapor grown carbon fibers, and carbon nanohorns. *J. Power Sources* **2014**, *266*, 471–474.
- (32) Wen, D.; Deng, L.; Zhou, M.; Guo, S.; Shang, L.; Xu, G.; Dong, S. A biofuel cell with a single-walled carbon nanohorn-based bioanode operating at physiological condition. *Biosens. Bioelectron.* **2010**, 25, 1544–1547.
- (33) Liu, Y.; Brown, C. M.; Neumann, D. A.; Geohegan, D. B.; Puretzky, A. A.; Rouleau, C. M.; Hu, H.; Styers-Barnett, D.; Krasnov, P. O.; Yakobson, B. I. Metal-assisted hydrogen storage on Ptdecorated single-walled carbon nanohorns. *Carbon* **2012**, *50*, 4953–4964.
- (34) Yodsin, N.; Rungnim, C.; Promarak, V.; Namuangruk, S.; Kungwan, N.; Rattanawan, R.; Jungsuttiwong, S. Influence of hydrogen spillover on Pt-decorated carbon nanocones for enhancing hydrogen storage capacity: A DFT mechanistic study. *Phys. Chem. Chem. Phys.* **2018**, *20*, 21194–21203.
- (35) Lodermeyer, F.; Costa, R. D.; Casillas, R.; Kohler, F. T.; Wasserscheid, P.; Prato, M.; Guldi, D. M. Carbon nanohorn-based electrolyte for dye-sensitized solar cells. *Energy Environ. Sci.* **2015**, 8, 241–246.
- (36) Zhu, C.; Liu, D.; Chen, Z.; Li, L.; You, T. Superior catalytic activity of Pt/carbon nanohorns nanocomposites toward methanol and formic acid oxidation reactions. *J. Colloid Interface Sci.* **2018**, *511*, 77–83.
- (37) Krungleviciute, V.; Ziegler, C. A.; Banjara, S. R.; Yudasaka, M.; Iijima, S.; Migone, A. D. Neon and CO₂ Adsorption on Open Carbon Nanohorns. *Langmuir* **2013**, *29*, 9388–9397.
- (38) Yamaguchi, T.; Bandow, S.; Iijima, S. Synthesis of carbon nanohorn particles by simple pulsed arc discharge ignited between pre-heated carbon rods. *Chem. Phys. Lett.* **2004**, 389, 181–185.
- (39) Chorkendorff, I.; Taylor, P.; Rasmussen, P. Synthesis and hydrogenation of formate on cu (100) at high pressures. *J. Vac. Sci. Technol., A* **1992**, *10*, 2277–2281.
- (40) Rasmussen, P.; Holmblad, P.; Askgaard, T.; Ovesen, C.; Stoltze, P.; Nørskov, J.; Chorkendorff, I. Methanol synthesis on Cu (100) from a binary gas mixture of CO_2 and H_2 . Catal. Lett. 1994, 26, 373–381.
- (41) Fujitani, T.; Choi, Y.; Sano, M.; Kushida, Y.; Nakamura, J. Scanning tunneling microscopy study of formate species synthesized from CO₂ hydrogenation and prepared by adsorption of formic acid over Cu (111). *J. Phys. Chem. B* **2000**, *104*, 1235–1240.
- (42) Gokhale, A. A.; Dumesic, J. A.; Mavrikakis, M. On the Mechanism of Low-Temperature Water Gas Shift Reaction on Copper. *J. Am. Chem. Soc.* **2008**, *130*, 1402–1414.
- (43) Rasmussen, P. B.; Holmblad, P. M.; Askgaard, T.; Ovesen, C. V.; Stoltze, P.; Nørskov, J. K.; Chorkendorff, I. Methanol synthesis on Cu(100) from a binary gas mixture of CO₂ and H₂. *Catal. Lett.* **1994**, 26, 373–381.
- (44) Grabow, L. C.; Gokhale, A. A.; Evans, S. T.; Dumesic, J. A.; Mavrikakis, M. Mechanism of the Water Gas Shift Reaction on Pt:

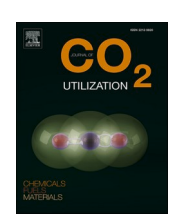
- First Principles, Experiments, and Microkinetic Modeling. J. Phys. Chem. C 2008, 112, 4608–4617.
- (45) Vosko, S. H.; Wilk, L.; Nusair, M. Accurate spin-dependent electron liquid correlation energies for local spin density calculations: a critical analysis. *Can. J. Phys.* **1980**, *58*, 1200–1211.
- (46) Becke, A. D. Density-functional exchange-energy approximation with correct asymptotic behavior. *Phys. Rev. A* **1988**, *38*, 3098–3100.
- (47) Lee, C.; Yang, W.; Parr, R. G. Development of the Colle-Salvetti correlation-energy formula into a functional of the electron density. *Phys. Rev. B* **1988**, *37*, 785–789.
- (48) Grimme, S.; Antony, J.; Ehrlich, S.; Krieg, H. A consistent and accurate ab initio parametrization of density functional dispersion correction (DFT-D) for the 94 elements H-Pu. *J. Chem. Phys.* **2010**, 132, No. 154104.
- (49) Rungnim, C.; Faungnawakij, K.; Sano, N.; Kungwan, N.; Namuangruk, S. Hydrogen storage performance of platinum supported carbon nanohorns: A DFT study of reaction mechanisms, thermodynamics, and kinetics. *Int. J. Hydrogen Energy* **2018**, *43*, 23336–23345.
- (50) Kittel, C. Introduction to Solid State Physics; Wiley, 2004.
- (51) Tawfik, S. A.; Cui, X. Y.; Ringer, S. P.; Stampfl, C. Multiple CO₂ capture in stable metal-doped graphene: a theoretical trend study. *RSC Adv.* **2015**, *5*, 50975–50982.
- (52) Vesselli, E.; et al. Hydrogen-Assisted Transformation of CO_2 on Nickel: The Role of Formate and Carbon Monoxide. *J. Phys. Chem. Lett.* **2010**, 1, 402–406.
- (53) Chan, B.; Radom, L. Zeolite-Catalyzed Hydrogenation of Carbon Dioxide and Ethene. *J. Am. Chem. Soc.* **2008**, *130*, 9790–9799.
- (54) Wu, H.-Y.; Fan, X.; Kuo, J.-L.; Deng, W.-Q. DFT Study of Hydrogen Storage by Spillover on Graphene with Boron Substitution. *J. Phys. Chem. C* **2011**, *115*, 9241–9249.



Contents lists available at ScienceDirect

Journal of CO₂ Utilization

journal homepage: www.elsevier.com/locate/jcou





Theoretical insights into catalytic CO₂ hydrogenation over single-atom (Fe or Ni) incorporated nitrogen-doped graphene

Preeyaporn Poldorn, Yutthana Wongnongwa, Tanabat Mudchimo, Siriporn Jungsuttiwong *

Center for Organic Electronic and Alternative Energy, Department of Chemistry and Center of Excellence for Innovation in Chemistry, Faculty of Science, Ubon Ratchathani University, Ubon Ratchathani, 34190, Thailand

ARTICLE INFO

Keywords: CO₂ hydrogenation DFT Nitrogen-doped graphene

ABSTRACT

Developing highly efficient and cheap catalysts for the CO₂ hydrogenation is the key to achieve CO₂ conversion into clean energy. Herein, periodic density functional theory (DFT) calculations are performed to investigate possible reaction mechanisms for the hydrogenation of CO2 to formic acid (cis- or trans-HCOOH) product over a single Fe or Ni atom incorporated nitrogen-doped graphene (Fe-N3Gr or Ni-N3Gr) sheets. Our calculations found that the CO₂ hydrogenation proceeds via a coadsorption mechanism to produce cis- or trans-HCOOH over Fe-N3Gr and Ni-N3Gr surfaces, which is classified into 2 steps: (1) the CO2 hydrogenation to form a formate (HCOO*) intermediate and (2) hydrogen abstraction to produce cis- or trans-HCOOH. The formation of trans-HCOOH over both Fe-N3Gr and Ni-N3Gr surfaces exhibit the obvious superiority due to the low barrier all through the whole channel. The highest energy barriers (Ea) in the case of trans-HCOOH formation on Fe-N3Gr and Ni-N3Gr surfaces are only 0.57 and 0.37 eV, respectively, which indicated that the CO2 hydrogenation to trans-HCOOH could be realized over these catalysts at low temperatures, especially the Ni-N3Gr surface. On the other hand, our findings show that the competitive reaction that produces CO and H₂O is almost impossible or extremely difficult to proceeds under ambient conditions due to the large E_a for the formation of these side products. Moreover, the microkinetic modeling of the CO₂ hydrogenation on both surfaces was investigated to confirm these results. Thus, the Fe-N3Gr and Ni-N3Gr catalysts reveal excellent catalytic activity and highly selective for CO₂ hydrogenation to trans-HCOOH. This theoretical investigation not only provides a promising catalyst but also gives a deeper understanding of CO₂ hydrogenation reaction.

1. Introduction

The rapid development of cities industrialization and transportation have caused expedited fossil fuel consumption, and has resulted in enormous amounts of carbon dioxide (CO₂) gas emission into the global atmosphere [1]. As well known, CO₂ is a major greenhouse gas, and the massive emission has led to global warming and climate change [2–4]. Hence, it is imperative to control the emission of this hazardous gas to avoid its negative or even irreversible impacts on the climate. Usually, CO₂ is considered as a large carbon source due to its high concentration. If the gas can serve as an available carbon feedstock for the production of a variety of valuable chemicals, then not only would this reduce greenhouse gas emissions, but also the problem of an energy crisis can be solved. Therefore, the development of efficient methods to employ CO₂ as a cheap and abundant carbon feedstock for the production of valuable chemicals is an attractive option.

There are many methods available to reduce or remove CO₂ from the atmosphere [5–10]. Among them, the catalytic conversion of CO₂ into high value-added chemical products seems to be most promising, since it is abundant, cheap, and nontoxic [11-13]. The products of CO2 hydrogenation consist of methanol (CH3OH), methane (CH4), formic acid (HCOOH), and hydrocarbon fuel, depending on the type of catalyst and the reaction conditions. Among these, formic acid is an important raw material with a wide range of industrial applications. More importantly, HCOOH is directly employed as a potential candidate for hydrogen storage, due to its easy transportation, storage, and handling [14-17]. Numerous theoretical and experimental investigations have studied the hydrogenation of CO2 into formic acid [18-30]. In recent years, it was found that using metals or metal oxides as substrate to support single-atom based non-noble transition metals can significantly improve the catalytic activities [31–33], but practical applications are limited by the high cost, highly toxic, and usually need high temperatures for

E-mail address: siriporn.j@ubu.ac.th (S. Jungsuttiwong).

^{*} Corresponding author.

efficient operation of substrate [20,34–36]. Therefore, the most promising substrate could be metal free materials, especially carbon-based materials due to excellent charge delivery ability and structural flexibility.

Single-atom catalysts (SACs) decorating carbon-based catalysts have attracted special attention for the CO2 hydrogenation into formic acid due to their excellent stability, high catalytic activity, high selectivity, and low fabrication cost [19,28,29,37-43]. Recent theoretical studies have also illustrated that a single metal atom incorporated on mono-vacancy defective graphene sheet exhibits great activity and selectivity toward the hydrogenation of CO₂ into HCOOH [19,25,27,29, 44,45]. Sirijaraensre et al. [25] have reported that Cu-embedded graphene shows promising catalytic activity for the direct transformation of formic acid from carbon dioxide and hydrogen molecules with the highest energy barrier (E_a) of 0.85 eV. Esrafili et al. [19] have used Pt- or Ni-doped graphene (Pt-G or Ni-G) as catalyst for the hydrogenation of CO₂ by a hydrogen molecule. They found that Pt-G has a higher catalytic activity than Ni-G one with the highest E_q of 1.25 and 1.97 eV, respectively. Furthermore Yodsin et al. [45] have reported that the Pt-decorated, defective, 4-pentagon, carbon nanocone (Pt/dCNC) is a candidate catalytic material for CO2 conversion into formic acid and requires a large activation energy of 1.15 eV for formic acid formation as the rate-determining step. Therefore, these materials serve as an ideal potential candidate for catalyst support in heterogeneous catalysis [41, 43,46]. However, considering E_a , it is proposed that the hydrogenation of CO2 molecule to formic acid is unlikely to take place over these surfaces under normal conditions.

Recently, the catalytic activity of metal-embedded graphene sheets can be significantly improved by the incorporation of pyridinic nitrogen atoms around the metal atom [28,37,38,40,47-51]. Bai et al. [50] indicated that incorporation of pyridinic nitrogen atoms around a single carbon vacancy in graphene leads to an accumulation of large positive charge on the embedded Fe atom, which enhances the catalytic activity of the surface in the O2 reduction reaction. Based on theoretical study, Wang et al. [51] reported that a single Ni atom decorated over N-doped graphene can be considered as a novel catalyst for the CO oxidation. In addition, Homlamai et al. [52] have reported that a single atom of Fe, Co, Ni and Cu supported on graphitic carbon nitride (g-C₃N₄) might be enhance the catalytic activity for CO₂ hydrogenation. Ma et al. [53] have used a Cu atom embedded C2N monolayer (Cu/C2N) as catalyst for CO2 hydrogenation. They indicate that Cu atom embedded C2N showed the high catalytic activity toward this reaction with the small energy barrier of rate determining step of 0.53 eV. Meng et al. [54] have investigated a series of transition metal dimer and nitrogen codoped graphene (M₂N₆-Gra, M = Cr–Cu) acting as electrocatalysts for CO₂ reduction reaction (CO₂RR). They predicted that Fe₂N₆-Gra is a promising CO₂RR catalyst due to the good selectivity and catalytic activity. Furthermore, Esrafili et al. [28] have illustrated that a single Co atom incorporated in a N-doped graphene matrix could efficiently catalyze the CO2 hydrogenation to form formic acid. Based on these calculation results, a series of non-precious metal embedded N-doped carbon substrates enhance the activity and selectivity toward the CO₂ hydrogenation. Interestingly, the Fe and Ni incorporated nitrogen-doped graphene substrate has been successfully synthesized experimentally [55-59]. Experimental results confirmed that the Fe and Ni embedded in N-doped graphene sheets can exhibit remarkable electrocatalytic activities [60,61]. However, the hydrogenation of CO2 to formic acid over a single Fe and Ni atom incorporated N-doped graphene substrates has never been reported.

Herein, the density functional theory (DFT) calculations were employed to investigate the $\rm CO_2$ adsorption and hydrogenation to formic acid over a single atom of non-precious metal, including Fe, and Ni, incorporated on N-doped graphene (M-N3Gr). The geometry, electronic structure and catalytic performance of Fe-N3Gr and Ni-N3Gr substrate are studied and compare these with other previous carbon-based materials in detail. These theoretical results could be helpful in understanding the chemical and catalytic properties of a single metal atom

incorporated nitrogen-doped graphene sheets and in designing highly efficient carbon-based catalysts for the conversion of CO_2 and other toxic gases to value-added chemical products. In facts, this theoretical investigation could be helpful for cleaning of the human society.

2. Calculation details

2.1. DFT calculations

The DFT calculations were carried out using the Dmol3 package in Material Studio 7.0 [62,63]. The electron exchange-correlation function within the generalized gradient approximation (GGA) of Perdew-Burke-Ernzerhof (PBE) functional [63,64] was used. To describe the ion-electron interactions, the DFT all electron core treatment was used, and all electrons are included in the calculation. A double numerical plus polarization (DNP) function was employed as the basis set, using real-space cutoff radius of 4.3 Å, and a wavefunction smearing energy of 0.005 Ha. The DFT + D method within the Grimme's scheme was used to describe the van der Waals interaction [65,66]. The convergence tolerance for energy change was set to 1×10^{-4} Ha, 0.004 Ha Å $^{-1}$ for maximum force, and 0.005 Å for maximum displacement.

A hexagonal 5×5 sheet containing 50 carbon atoms was employed to simulate the pristine graphene (PGr), with a lattice constant of a=12.3 Å and b=12.3 Å. The single-vacancy defective graphene (DGr) was obtained by removing one carbon atom from the PGr. After that, carbon atoms around the vacancy site were replaced with 1, 2, and 3 nitrogen atoms to obtain nitrogen-doped graphene (NxGr, x=1, 2 and 3) sheets; N1Gr, N2Gr and N3Gr (Fig. 1). Lastly, two non-precious metal atoms including Fe and Ni incorporated NxGr sheets were prepared by putting a Fe or Ni atom on the vacancy site. To avoid any inter-layer interactions of periodic images, a vacuum spacing was set to be 30 Å in the z direction to the sheet. The Brillouin zone integration was sampled using a $5\times5\times1$ Monkhorst-Pack mesh.

In order to find the transition state (TS), a linear synchronous transit (LST) maximum calculation was performed for TS searches. The conjugate gradient (CG) method optimization and a quadratic synchronous transit (QST) maximization method was repeated for subsequent processing until an accurate transitional state was found [67,68]. At the same time, the search for the TS was verified by means of frequency analysis, and only a single imaginary frequency was identified for each TS.

2.2. Energy analysis

The formation energy (E_f) of a DGr and NxGr substrate are given by

$$E_f = E_{substate} - m\mu_C - n\mu_N \tag{1}$$

where $E_{\rm substrate}$ is the total energy of a DGr or NxGr. The terms $\mu_{\rm C}$ and $\mu_{\rm N}$ represent the chemical potential of one single carbon atom in the pristine graphene, and the chemical potential of the nitrogen atom, which is defined as half of the N₂ molecule energy in the gas phase, respectively [28,37,48–50,69]. Terms m and n are the total number of C and N atoms in the substrate. In order to check the stability of M-NxGr, the binding energies ($E_{\rm b}$) of M atom deposition on the N3Gr sheets (M-N₃Gr) were obtained using the following equations:

$$E_b = E_{M-N3Gr} - E_{N3Gr} - E_M (2)$$

where $E_{\text{M-N3Gr}}$, E_{N3Gr} , and E_{M} represent the total energy of the M-doped N3Gr surface, the energy of the optimized N3Gr surface, and the energy of M atom in the gas phase, respectively.

The adsorption energy (E_{ads}) is defined as:

$$E_{ads} = E_{A/M-N3Gr} - E_{M-N3Gr} - E_A (3)$$

where $E_{A/M-N3Gr}$ and E_A are total energies of the adsorbate on M-N3Gr,

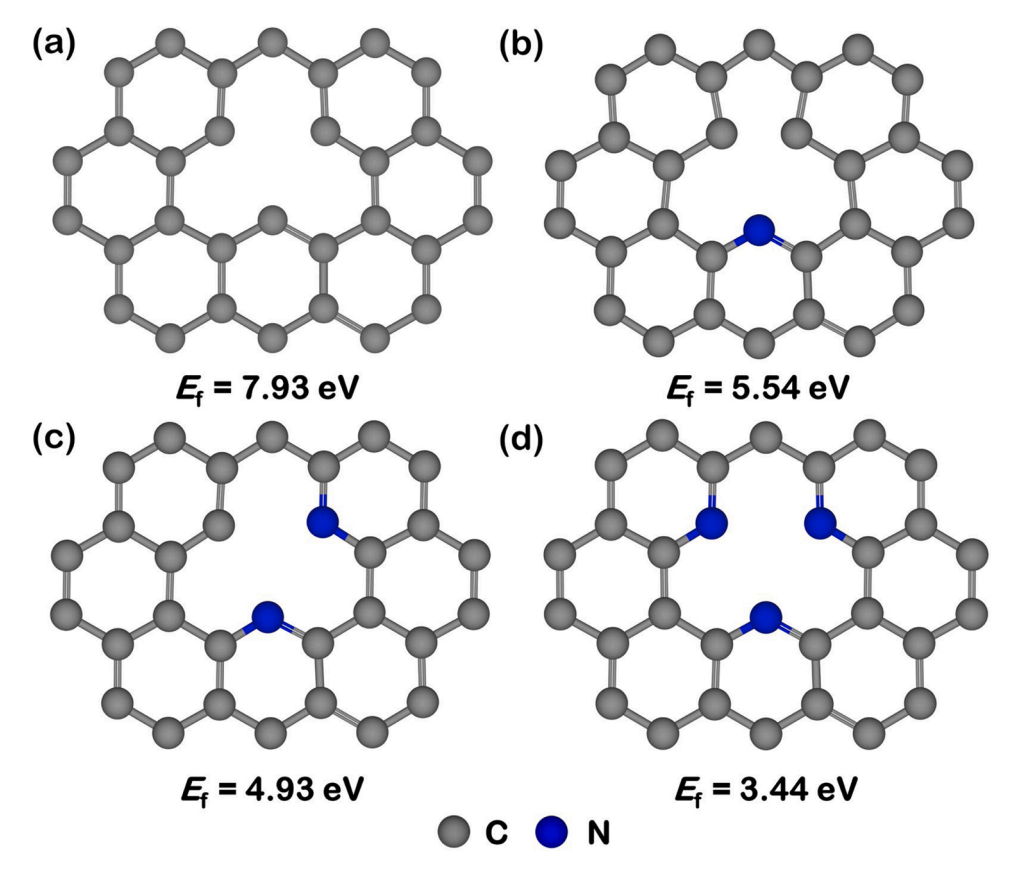


Fig. 1. The optimized structures and related formation energy (E_f) values of (a) DGr, (b) N1Gr, (c) N2Gr and (d) N3Gr surfaces.

and the isolate adsorbate in the gas phase, respectively. The stability of the molecule adsorption on the catalyst increases with the size of the negative value of the $E_{\rm ads}$ between the gas molecules. It should correspond to an energetically favorable and exothermic adsorption process.

2.3. Microkinetic modeling

The CO_2 hydrogenation rate is calculated by the in-house developed MKMCXX microkinetic modeling software [70]. In our simulations, the inlet concentration of gas phase contained a mixture of CO_2 and H_2 in 1:1 ratio at a total pressure of 1 atm. The Eyring equation was used to determine the rate constants for the forward and backward elementary reaction:

$$k = Ae^{\left(\frac{-E_a}{k_B T}\right)} \tag{4}$$

$$A = \frac{k_b T}{h} \frac{Q^{\text{TS}}}{Q} \tag{5}$$

where k, $k_{\rm b}$, T, h, $E_{\rm a}$, $Q^{\rm TS}$, and Q are the reaction rate constant in s⁻¹, Boltzmann constant, Planck's constant, transition-state partition function, and the initial-state partition function, respectively. As an approximation, the pre-factor A was set to $10^{13}\,{\rm s}^{-1}$ for all the elementary reactions.

For non-activated molecular adsorption, the energy barrier was 0. The adsorption of molecule on surface, it undergoes an appreciable change in entropy, which is represented by the partition functions.

$$Q^{TS} = f_{trans}^{(2)} f_{rot}^{(3)} f_{vib}^{(3N-5)}$$
(6)

$$Q = f_{trans}^{(2)} f_{rot}^{(3)} f_{vib}^{(3N-6)}$$
(7)

Formulas for the translational, vibrational, and rotational partition functions can be written as

$$f_{trans} = \frac{L\sqrt{2\pi m k_b T}}{h} \tag{8}$$

$$f_{vib} = \frac{1}{1 - e^{\Theta_t/T}} \tag{9}$$

$$f_{rot} = \frac{8\pi^2 I k_b T}{h^2} \tag{10}$$

The transition state represents the activated molecule, which contains two translational, three rotational and otherwise 3 N - 5 vibrational degrees of freedom. One of the partition functions corresponding to an imaginary frequency in the direction of the reaction coordinate has been cut out.

The initial state represents the molecule in the gas phase, which contains three rotational and three translational degrees of freedom as denoted by the number between round braces. Furthermore, all other 3 N - 6 degree of freedom are vibrational.

Based on above assumptions, the rate of adsorption can derive, which is known in the literature as Hertz-Knudsen [71]. Hence, the molecular adsorption rate constant (k_{ads}) can be expressed as:

$$k_{ads} = \frac{-PA'}{\sqrt{2\pi m k_b T}} S \tag{11}$$

where P, A', m, and S are the partial pressure of the adsorbate in the gas phase, surface area of the adsorption site, mass of adsorbate and sticking coefficient (assumed to be 1.0).

For the desorption process, it is assumed that the transition state comprises three rotational degrees of freedom and two translational degrees of freedom. Accordingly, the desorption rate constant ($k_{\rm des}$) is given by

$$k_{des} = \frac{k_b T^3}{h^3} \frac{A'(2\pi m k_b)}{\sigma \theta_{rot}} \exp(\frac{-E_{des}}{k_b T})$$
 (12)

where, term σ and θ_{rot} are the symmetry number and the characteristic temperature for rotation, respectively. E_{des} is the desorption energy [72].

3. Results and discussion

3.1. Geometry, electronic structure, and stability of the NxGr surfaces

Based on earlier studies, there are mainly three types of nitrogen doping in graphene, pyridinic nitrogen, graphitic nitrogen, and pyrrolic nitrogen [73-75]. Numerous experimental results report a high reactivity of pyridinic nitrogen toward an oxidation and reduction reaction (ORR) [22,76,77]. In addition, when the pyridinic-type nitrogen was annealed at mild temperature, it still kept its structure and properties [78]. Thus, we only focused on pyridinic nitrogen-doped single-vacancy defective graphene. The optimized structures and related E_f values of four different surface models, including a single-vacancy defective graphene (DGr), and a single-vacancy defective graphene with one (N1Gr), two (N2Gr) and three nitrogen (N3Gr) atoms incorporated around the vacancy site are shown in Fig. 1. In the DGr structure (Fig. 1a), carbon atoms around the vacancy will bond together with dangling bonds. The computed E_f of DGr is 7.93 eV, which is in agreement with those of previous studies [39,47]. Replacing the C atom around the single vacancy in DGr with one, two, and three N atoms will form a pyridinic N, namely, N1Gr (Fig. 1b), N2Gr (Fig. 1c) and N3Gr (Fig. 1d), respectively. The E_f of the N1Gr, N2Gr and N3Gr decreases to 5.54, 4.93, and 3.44 eV, respectively. The calculated result indicates that the $E_{\rm f}$ decreases as the number of N coordinates around the vacancy site increases. Accordingly, the incorporation of N atoms in the N3Gr sheet is able to greatly stabilize a single-vacancy defect in graphene, which is consistent with results obtained from other theoretical studies [39,40,47,51,79]. In addition, the Hirshfeld analysis of these surfaces were investigated, which illustrates that the atoms around the single vacancy in N1Gr, N2Gr, and N3Gr have a total charge of -0.106, -0.168, and -0.336 |e|,

respectively. The total charge of atoms around the single vacancy in N3Gr surface is more negative than that in N1Gr and N2Gr surfaces, which indicates that the N3Gr sheet might be the most active surface to trap a Fe or a Ni atom to form Fe-N3Gr and Ni-N3Gr substrates. Hence, we expect that the N3Gr surface can be a supporter of Fe and Ni atoms for the $\rm CO_2$ hydrogenation into formic acid.

3.2. Single metal atom supported on N3Gr (M-N3Gr) surfaces

In this section, a single Fe or Ni atom supported on N3Gr (Fe-N3Gr and Ni-N3Gr) sheets were investigated using DFT calculations to understand the stability of the Fe and Ni atoms on the N3Gr surface. Fig. 2 shows the most stable geometries, related E_b values, and metal charges (Q_M) of the Fe-N3Gr and Ni-N3Gr surfaces. Our calculated result found that the metal atoms can adsorb stably at the vacancy center of the N3Gr sheet, while the metal atom forms bonds with three adjacent nitrogen atoms at the vacancy site. Both metal atoms have an atomic radius that is greater than that of nitrogen, and thus, the metal atom is displaced outward from the N3Gr sheet. As shown in Fig. 2a and b, the E_b of the Fe and Ni atoms incorporated in N3Gr are -5.65 and -4.33 eV, respectively, illustrating good stability and a strong interaction between the metal atom and the N3Gr substrate. The interatomic distance between the metal atoms and the nearest pyridinic N atom are found to be 1.82 (Fe) and 1.88 (Ni) Å, respectively, which correspond to previous works [49-51]. In addition, the Hirshfeld analysis reveals that the electron transfer from metal atoms to the N3Gr sheet leads to a more positive charge of 0.248 to 0.282 |e| accumulated on the metal atoms, which confirms the strong interaction between the metal atoms and the N3Gr sheet. These findings are also consistent with the electron density different (EDD) analysis as shown in Fig. 3, indicating that there is a large electron density accumulation around the metal atoms and single vacancy site of N3Gr surface. Therefore, the Fe-N3Gr and Ni-N3Gr surfaces are very stable and suitable to serve as the active catalytic center for CO2 hydrogenation to formic acid.

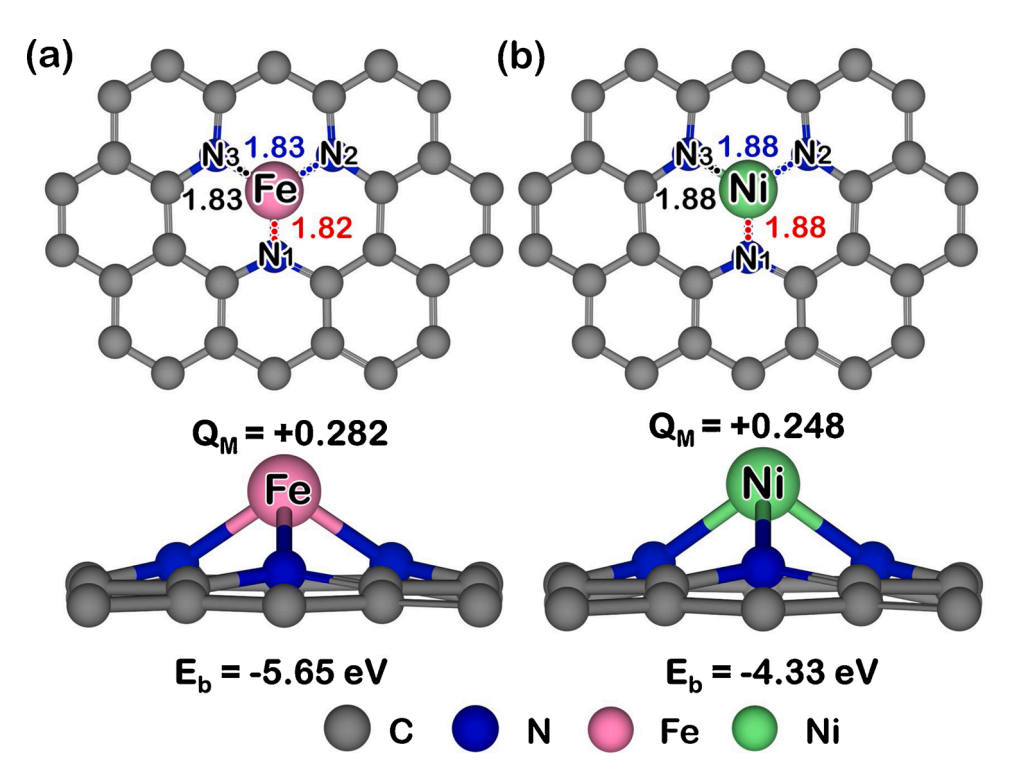


Fig. 2. Optimized structures (top and side views), related binding energies ($E_{\rm b}$), and metal charges ($Q_{\rm M}$) of (a) Fe-N3Gr and (b) Ni-N3Gr surfaces.

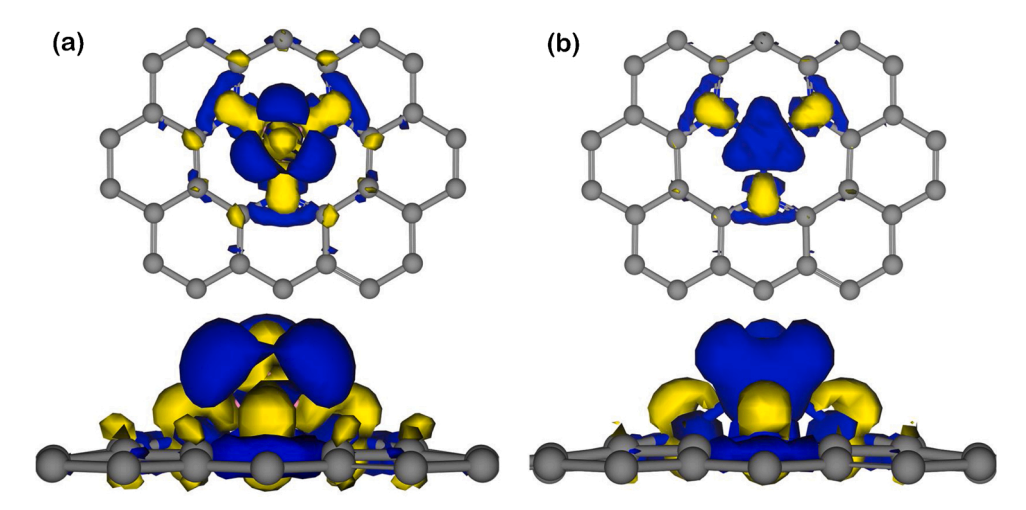


Fig. 3. Electron density different (EDD) maps of (a) Fe-N3Gr, and (b) Ni-N3Gr surfaces. In the EDD plots, the electron density gain regions are shown in blue, and electron density loss regions in yellow. The isovalue for EDD plots is ± 0.03 au.

3.3. Adsorption of CO2 and H2 on Fe-N3Gr and Ni-N3Gr surfaces

In this section, the adsorption of individual CO_2 and H_2 and coadsorption of CO_2 and H_2 are considered on Fe-N3Gr and Ni-N3Gr substrates. To find the most stable adsorption site for CO_2 and H_2 , all the possible adsorption structures were investigated. The most stable structures, related $E_{\rm ads}$ values, and gas charges ($Q_{\rm gas}$) of the CO_2 and H_2

adsorption on Fe-N3Gr and Ni-N3Gr surfaces are displayed in Fig. 4. For CO₂ adsorption, the CO₂ molecule adsorbs on the M site via the M—C and M—OO— bonds, as a bidentate configuration in both M-N3Gr substrates (see Fig. 4a and d). The calculated $E_{\rm ads}$ of the CO₂ adsorption on FeN3Gr and NiN3Gr surfaces are -0.60, and -0.74 eV, respectively. For H₂ adsorption, the most energetically favorable configuration is characterized by having H₂ lay parallel to the surfaces (see Fig. 4b and e).

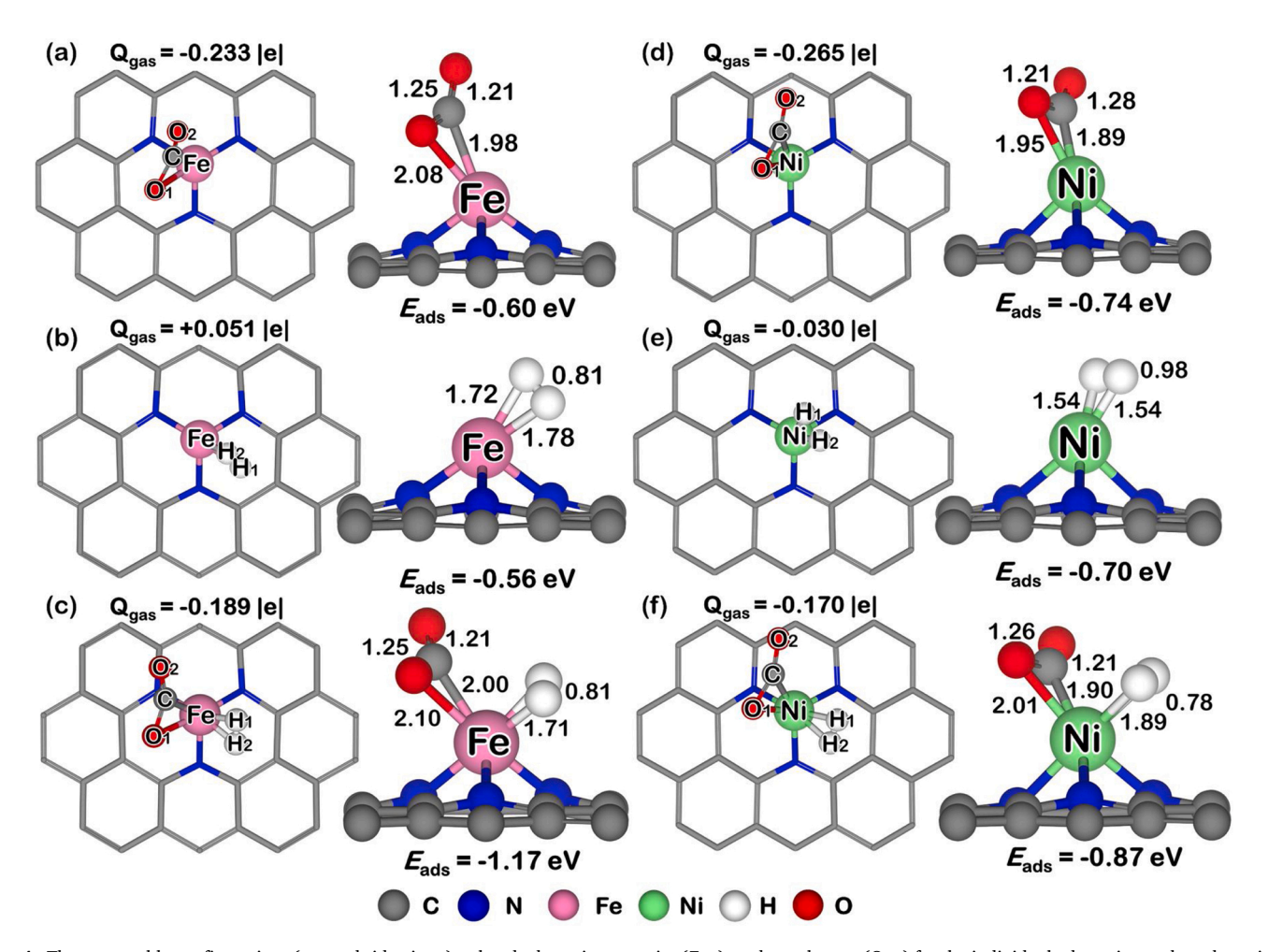


Fig. 4. The most stable configurations (top and side views), related adsorption energies (E_{ads}), and gas charges (Q_{gas}) for the individual adsorption and coadsorption of CO_2 and H_2 on (a-c) Fe-N3Gr and (d-f) Ni-N3Gr surfaces.

The H₂ molecule are adsorbed on FeN3Gr and NiN3Gr surfaces with E_{ads} of -0.56 and -0.70 eV, respectively. Our results show that the $E_{\rm ads}$ value of CO2 and H2 adsorption on the NiN3Gr surface is slightly lower than that on the FeN3Gr surface, which indicated that the CO2 and H2 adsorption on the NiN3Gr surface is a little more stable than that on the FeN3Gr surface. This result corresponds to the Hirshfeld analysis of the individual adsorption, indicating that the Hirshfeld charges of individual CO₂ and H₂ on Ni-N3Gr (-0.265 and -0.030 |e|) are more negative than that on Fe-N3Gr (-0.233 and 0.051 |e|). For CO₂ and H₂ coadsorption, both CO2 and H2 molecules are adsorbed on the metal sites of Fe-N3Gr and Ni-N3Gr surfaces as shown in Fig. 4c and f. The calculated $E_{\rm ads}$ of these molecules on the surfaces are -1.17 and -0.87 eV, respectively, which is larger than the E_{ads} of individual CO_2 and H_2 molecules. It indicated that the coadsorption is stronger than the individual adsorption on both surfaces, which confirms by the EDD analysis of the CO₂ and H₂ coadsorption on the surfaces as shown in Fig. 5. The EDD maps show that there is a large electron density accumulation around the gas molecules and the active site of the both surfaces. In addition, the Eads of CO2 and H2 adsorption on the Fe-N3Gr surface is lower than that on the Ni-N3Gr surface, suggesting that these molecules are more stable on the Fe-N3Gr surface. This result corresponds to the Hirshfeld analysis of the CO₂ and H₂ coadsorption on the surfaces, indicating that the Hirshfeld charge of both gases on Fe-N3Gr (-0.189 | e|) is more negative than that on Ni-N3Gr (-0.170 |e|). Overall, the individual CO2 and H2 adsorption is stronger adsorbed on the Ni-N3Gr surface, while the CO2 and H2 coadsorption is stronger adsorbed on the Fe-N3Gr surface. However, the coadsorption is more stable than the individual adsorption on both surfaces. Therefore, the gases coadsorption on both surfaces were considered in the CO₂ hydrogenation to formic acid.

3.4. CO₂ hydrogenation on the Fe-N3Gr and Ni-N3Gr surfaces

According to previous works [80,81], the CO_2 hydrogenation to formic acid can occur via two pathways, which are the formate intermediate (HCOO*) and the carboxyl intermediate (COOH*) pathways. However, the CO_2 hydrogenation to formic acid on the single metal atom decorated N-doped graphene catalysts have to proceed via the

HCOO* pathway because the COOH* pathway is barely possible on these surfaces [28,37,52,82]. The COOH* pathway is replaced by a side reaction pathway, which generates CO and $\rm H_2O$ molecules. These results indicated that the $\rm CO_2$ hydrogenation to formic acid on these surfaces is classified into 2 pathways, which are the HCOO* and side reaction pathways. In addition, the $E_{\rm ads}$ value of $\rm H_2$ adsorption close to the $E_{\rm ads}$ value of $\rm CO_2$ adsorption on both surfaces, and the $E_{\rm ads}$ values of $\rm CO_2$ and $\rm H_2$ coadsorption over these surfaces are significantly lower than that for the individual gas adsorption (Fig. 3), indicating that these surfaces are covered with both gases. Therefore, we focused on the $\rm CO_2$ hydrogenation to formic acid through a coadsorption mechanism with the HCOO* and side reaction pathways on the Fe-N3Gr and Ni-N3Gr surfaces.

3.4.1. CO₂ hydrogenation via the HCOO* pathway

In this section, we investigated the catalytic CO_2 hydrogenation to formic acid through the coadsorption mechanism with the HCOO* pathway on the Fe-N3Gr and Ni-N3Gr catalysts, which were denoted as **Route-A** and **Route-B** pathways, respectively.

3.4.1.1. Route-A reaction pathway. In Route-A, the CO₂ hydrogenation via the HCOO* pathway on Fe-N3Gr surface was investigated. Fig. 6 shows energy profile and the structures along the reaction pathway. The main reaction of CO2 hydrogenation to cis- or trans-HCOOH over Fe-N3Gr surface is proposed to proceed by a three-step process; first the formation of a HCOO* intermediate, followed by the HCOO* turns around, and finally convert to cis- or trans-HCOOH*. The third step was classified into 2 reaction pathways, which were presented as Route-A1 and Route-A2 pathways, respectively. Route-A1 and Route-A2 pathways represent *cis*- and *trans*-HCOOH formation pathways, respectively. In the first step, the reaction starts with the coadsorption of both CO2 and H_2 molecule on the Fe-N3Gr surface with an E_{ads} of -1.17 eV (CO₂+H₂-coads). Then, a hydrogen atom from the H₂ molecule (H1) reacts with the C-atom from CO2 to form the HCOO* intermediate (IM1a-Route A) on the Fe-N3Gr surfaces, requiring $E_a = 0.57$ eV (TS1-Route A). During this process, the bond length of H₂ molecule elongates from 0.81 Å to 1.56 Å, while the distance between the C-atom of adsorbed CO₂ and H1 decreases form 2.37 Å to 1.50 Å. Subsequently, the

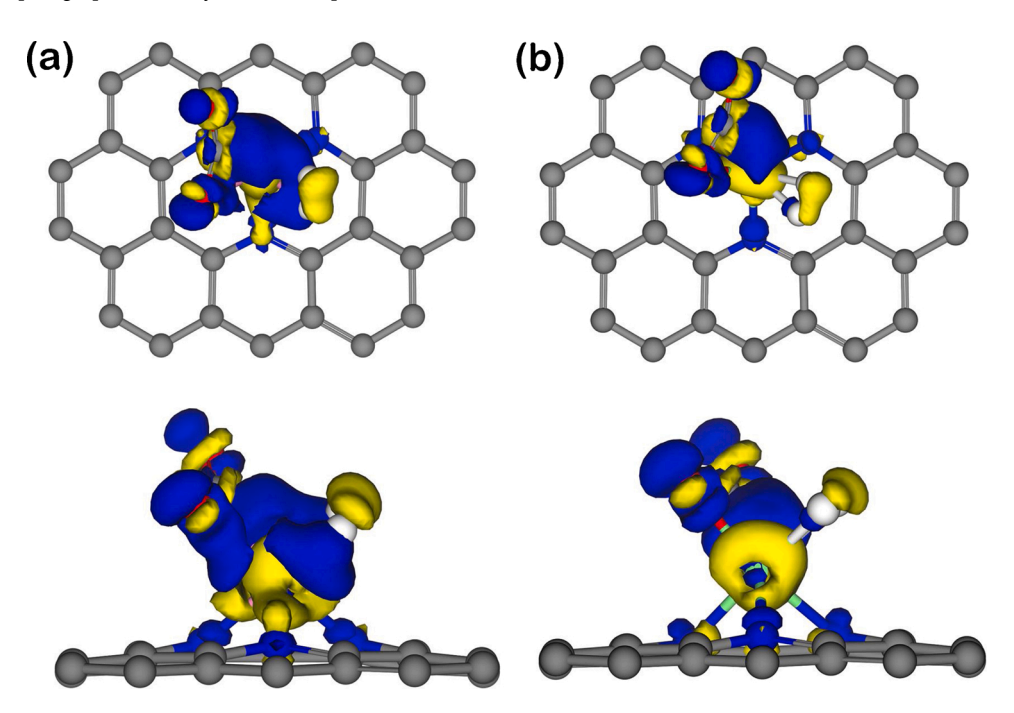


Fig. 5. The EDD maps of CO_2 and H_2 coadsorption on (a) Fe-N3Gr and (b) NiN3Gr surfaces. In the EDD plots, the electron density gain regions are shown in blue, and electron density loss regions in yellow. The isovalue for EDD plots is ± 0.03 au.

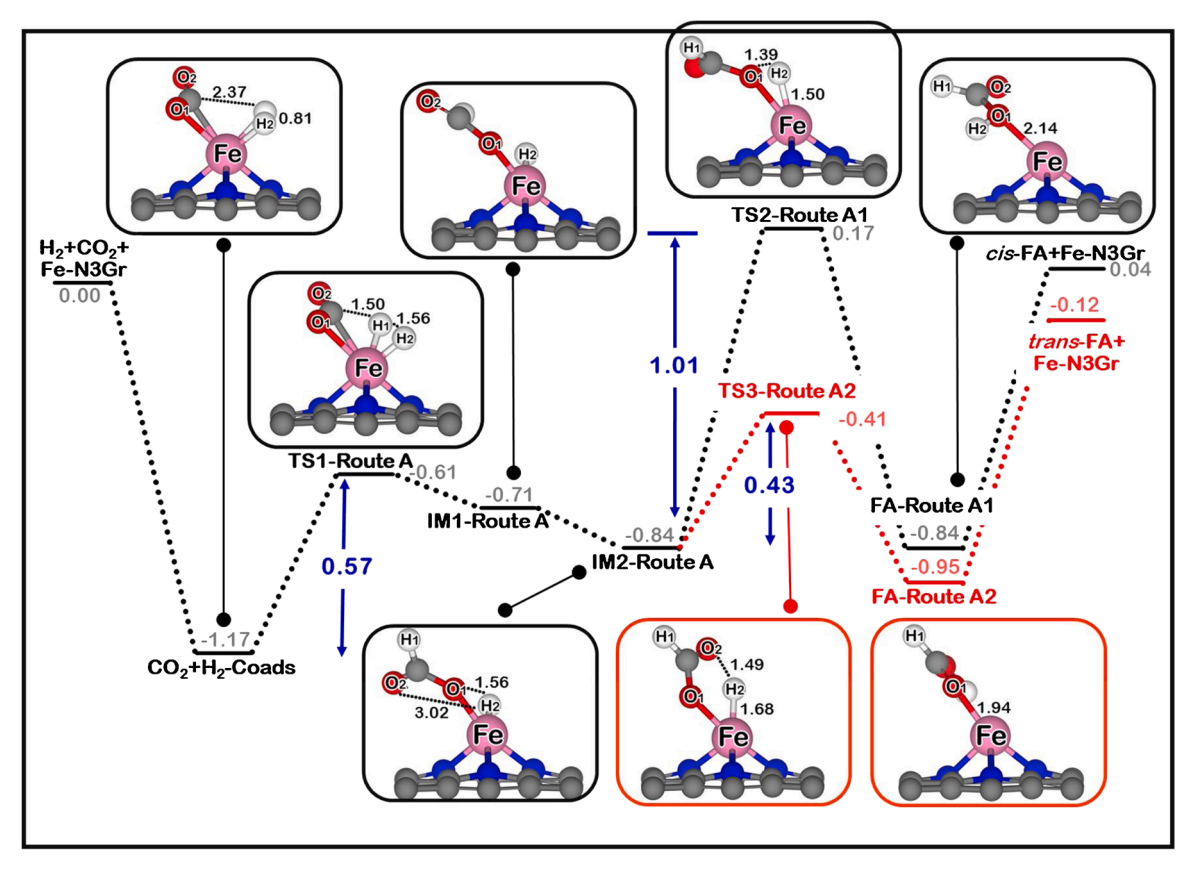


Fig. 6. Catalytic reaction pathways (eV) for CO2 hydrogenation to formic acid over an Fe-N3Gr catalyst, via Route-A. Distances are given in Å.

HCOO* intermediate in **IM1-Route** A state turns around to form **IM2-Route** A state. After that, the HCOO* intermediate undergoes hydrogenation to HCOOH products on Fe-N3Gr via either **Route-A1** or **Route-A2** pathway. In **Route-A1**, the formate intermediate (**IM2-Route** A)

undergoes hydrogenation to *cis*-HCOOH (**FA-Route A1**) through **TS2-Route A1** state with a large E_a of 1.01 eV. Finally, *cis*-HCOOH desorbs from the surface with desorption energy ($E_{\rm des}$) of 0.88 eV. By contrast, **Route-A2** involves the HCOO* hydrogenation to the *trans*-HCOOH

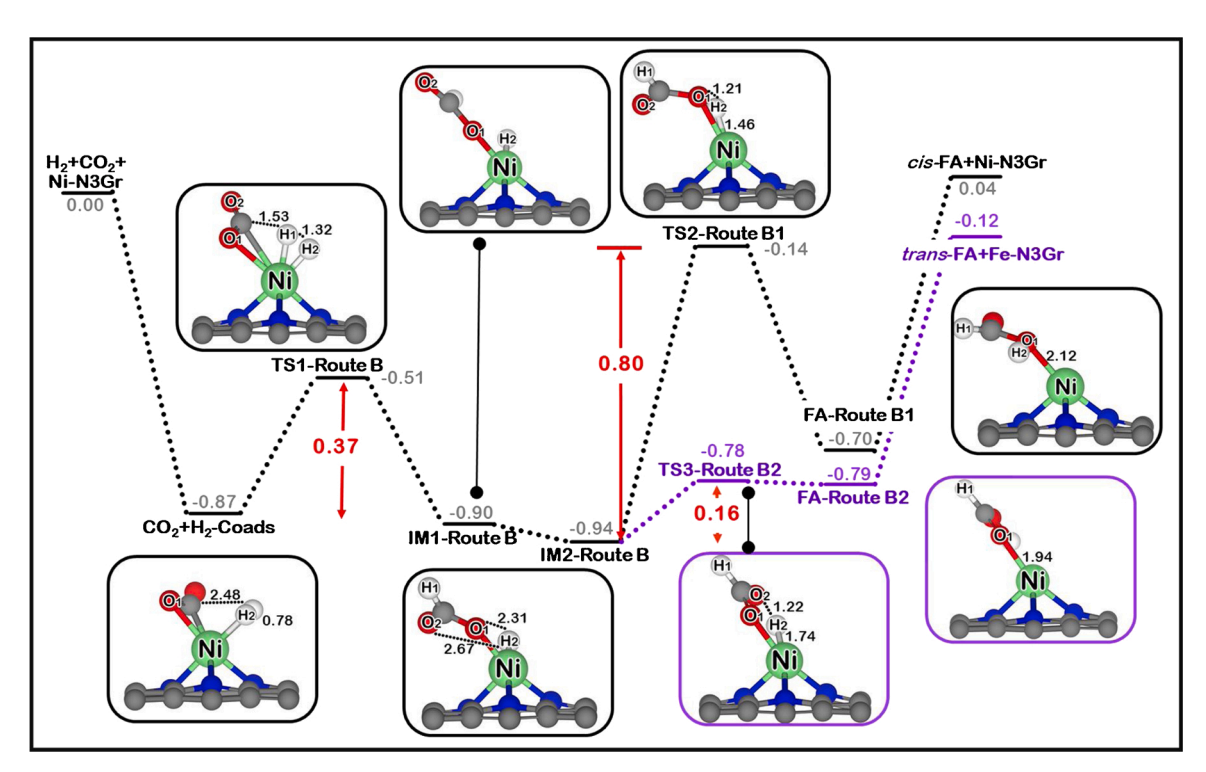


Fig. 7. Catalytic reaction pathways (eV) for CO₂ hydrogenation into formic acid over Ni-N3Gr catalyst, via Route B. Distances are given in Å.

product. The reaction goes through **TS3-Route A2** state to produce a *trans*-HCOOH product (**FA-Route A2**), requiring $E_a = 0.43$ eV. Finally, the *trans*-HCOOH is desorbed to the gas phase with $E_{\rm des}$ of 0.83 eV. Overall, the **Route-A1** pathway is endothermic reaction with reaction energy ($E_{\rm T}$) of 0.04 eV, while the **Route-A2** pathway is exothermic reaction with $E_{\rm T}$ of -0.12 eV. The rate determining steps of **Route-A1** and **Route-A2** pathways are the *cis*-HCOOH and HCOO* formation steps with $E_{\rm A}$ of 1.01 and 0.57 eV, respectively. These results indicated that the CO₂ hydrogenation on Fe-N3Gr is both thermodynamically and kinetically more favorable to produce *trans*-HCOOH than *cis*-HCOOH. Therefore, the main reaction on this surface is the CO₂ hydrogenation to the *trans*-HCOOH product (**Route-A2**).

3.4.1.2. Route-B reaction pathway. In this reaction pathway, the reaction mechanisms of CO2 hydrogenation to formic acid via a HCOO* intermediate over Ni-N3Gr was also studied. Fig. 7 shows energy profile and the structures along the reaction pathway. The main reaction of CO₂ hydrogenation to cis- or trans-HCOOH over the Ni-N3Gr surface is similar to the previous section. The final step of this reaction was classified into 2 pathways, which were presented as Route-B1 and Route-B2 pathways, respectively. Route-B1 and Route-B2 pathways represent cis- and trans-HCOOH formation pathways, respectively. The reaction starts with CO2 and H2 coadsorption on Ni-N3Gr surface (CO2+H2**coads**) with $E_{\rm ads}$ of -0.87 eV. Subsequently, the reaction goes through **TS1-Route B** state to form HCOO* intermediate (**IM2-Route B**) with E_a of 0.37 eV, which is smaller than the rate-determining step of Route-A2 (0.57 eV). Finally, HCOO* (IM2-Route B) reacts with the residual hydrogen atom and proceeds though Route-B1 or Route-B2 pathway to produce cis- and trans-HCOOH. In Route-B1, cis-HCOOH* (FA-Route **B1**) is formed over the Ni-N3Gr surface via **TS2-Route B1** state with E_a of 0.80 eV. Consequently, cis-HCOOH* desorbs to the gas phase, requiring E_{des} of 0.74 eV. In another pathway, the HCOO* intermediate (IM2-Route B) subsequently reacts with the residual hydrogen atom (H2), and trans-HCOOH* forms (FA-Route B2) over the Ni-N3Gr surface via TS3-Route B2 state. This step has a very small E_a of 0.16 eV, less than that obtained for Fe-N3Gr surface. Moreover, the Eads of formic acid is about -0.67 eV, illustrating that the formic acid would desorb spontaneously from the Ni-N3Gr surface, and the catalyst can be reused for the new catalytic cycle. In summary, the CO₂ hydrogenation to the cis-HCOOH product on the Ni-N3Gr surface is unfavorable and hardly proceeds. Noteworthy, the CO2 hydrogenation proceeds via Route-B2 much more easily due to a very small E_a of the reaction. The ratedetermining step for the CO2 hydrogenation via Route-B2 is the formation of the formate intermediate at **TS1-Route B** state, with E_a of 0.37 eV, also similar to Fe-N3Gr surface. Thus, the CO₂ hydrogenation on Ni-N3Gr to produce trans-HCOOH is both thermodynamically and kinetically more favorable than the cis-HCOOH product. Based on these findings, we conclude that the Ni-N3Gr surface displays a higher reactivity toward CO2 hydrogenation to formic acid than the Fe-N3Gr surface does (0.37 vs 0.57 eV).

For comparison, the four reaction pathways shown in Figs. 6 and 7 represent *trans*- and *cis*-HCOOH formation pathways on the Fe-N3Gr and Ni-N3Gr surfaces. In each surface, the *trans*-HCOOH formation is more favorable than the *cis*-HCOOH formation. The first hydrogenation step is key to determining the *trans*-HCOOH product of the CO₂ hydrogenation on both surfaces. The rate-determining step of *trans*-HCOOH formation in the **Route-B2** pathway (0.37 eV) is slightly lower than that for **Route-A2** (0.57 eV). However, the trans-HCOOH formation can occur on the Fe-N3Gr and Ni-N3Gr surfaces.

3.4.2. CO₂ hydrogenation via side reaction pathway

Another possible reaction pathway on both surfaces was considered as an important competing reaction in the formation of CO and H_2O molecules ($CO_2 + H_2 \rightarrow CO + H_2O$). **Route-C** and **Route-D** pathways presented the CO_2 hydrogenation to formic acid via carboxyl

intermediate over Fe-N3Gr and Ni-N3Gr, respectively.

3.4.2.1. Route-C reaction pathway. In this section, the CO₂ hydrogenation via side reaction pathway on Fe-N3Gr surface was investigated. The energy profile and the structures along the reaction pathway are shown in Fig. 8. This reaction starts with the coadsorption of CO₂ and H₂ molecules over the Fe-N3Gr surface (CO2+H2-Coads), followed by conversion to the OH* and CO* intermediate (IM1-Route C) though the transition state (TS1-Route C) with a high E_a of 1.40 eV, which is much larger than the rate-determining step of Route-A in the CO2 hydrogenation to formic acid (0.57 eV). Then, H1 transfers from the Fe atom to O1 (TS2-Route C), with Ea of 0.61 eV. Finally, the CO* and H2O* molecule is produced and absorbs on the Fe at the Fe-N3Gr surface (H2O + **CO-ads**) with E_{ads} of -2.78 eV, which illustrates that these molecules cannot be easily released from the reactive site of the catalyst at room temperature. Overall, this process is almost impossible or proceeds with great difficulty. The formation of the CO and H₂O molecules (H₂O + CO-ads) are strongly absorbed on the Fe atom. These results indicate that the reduction of CO2 to CO is less competitive compared with the CO2 hydrogenation to formic acid. Therefore, the Fe-N3Gr surface indicates the high selectivity towards the CO2 hydrogenation to formic acid.

3.4.2.2. Route-D reaction pathway. In **Route-D** pathway, the reduction of CO₂ over Ni-N3Gr was also considered, and the reaction mechanism is similar to that for Fe-N3Gr (Route-C). Fig. 9 shows energy profile and the structures along the reaction pathway. As mentioned before, the CO2 and H₂ molecules co-adsorb on Ni at the Ni-N3Gr surface, with E_{ads} of -0.87 eV (CO₂+H₂-Coads). They are next converted to the OH* and CO* intermediates (IM1-Route D) via TS1-Route D state with E_a of 0.78 eV, which is higher than that for the CO₂ hydrogenation via Route-B2 (0.37 eV). After that, the H2 atom reacts with O1 (TS2-Route D) to form CO* and H_2O^* products ($H_2O + CO$ -ads), with a small E_a of 0.38 eV. Finally, the CO and H2O molecules are adsorbed over the Ni-N3Gr surface with $E_{\rm ads}$ of -2.28 eV, suggesting that this product cannot be easily released from the active site of the catalyst at room temperature. In summary, the rate-determining step of this reaction is the OH* and CO* formation with E_a of 0.78 eV, which is higher than that for the CO_2 hydrogenation via Route-B2 (0.37 eV). The products are strongly absorbed on the Ni-N3Gr surface with a high E_{ads} of -2.28 eV. These results indicate that the reduction of CO₂ to CO is also less competitive compared with the CO₂ hydrogenation to formic acid. Thus, the Ni-N3Gr surface exhibits high selectivity towards the CO2 hydrogenation to formic acid.

For comparison, the two reaction pathways shown in Figs. 8 and 9 display CO and $\rm H_2O$ formation pathway on the Fe-N3Gr and Ni-N3Gr surfaces. Our calculations show that the first hydrogenation step is the rate-determining step of CO and $\rm H_2O$ formation on both surfaces. The CO and $\rm H_2O$ formation on Ni-N3G surface (Fig. 9) is more energetically favorable than that on Fe-N3G surface shown in Fig. 8 (0.78 vs 1.40 eV). However, the rate-determining step of this reaction on the Fe-N3Gr and Ni-N3Gr surfaces are very higher than that for the $\rm CO_2$ hydrogenation via **Route-A2** and **Route-B2** (0.57 and 0.37 eV).

Summary, the $\rm CO_2$ hydrogenation on both surfaces are classified into 3 pathways, which are (I) the *trans*-HCOOH formation, (II) the *cis*-HCOOH formation, and (III) the CO and H₂O formation pathways as shown in Figs. 6–9. Our results show that the *trans*-HCOOH formation is both thermodynamically and kinetically more favorable than the *cis*-HCOOH and side products (CO and H₂O) formation. Therefore, the main reaction of $\rm CO_2$ hydrogenation on both surfaces are the *trans*-HCOOH formation in **Route-A2** and **Route-B2**.

3.5. Microkinetic modeling for CO₂ hydrogenation

From the previous section, the electronic energy profile of the CO₂

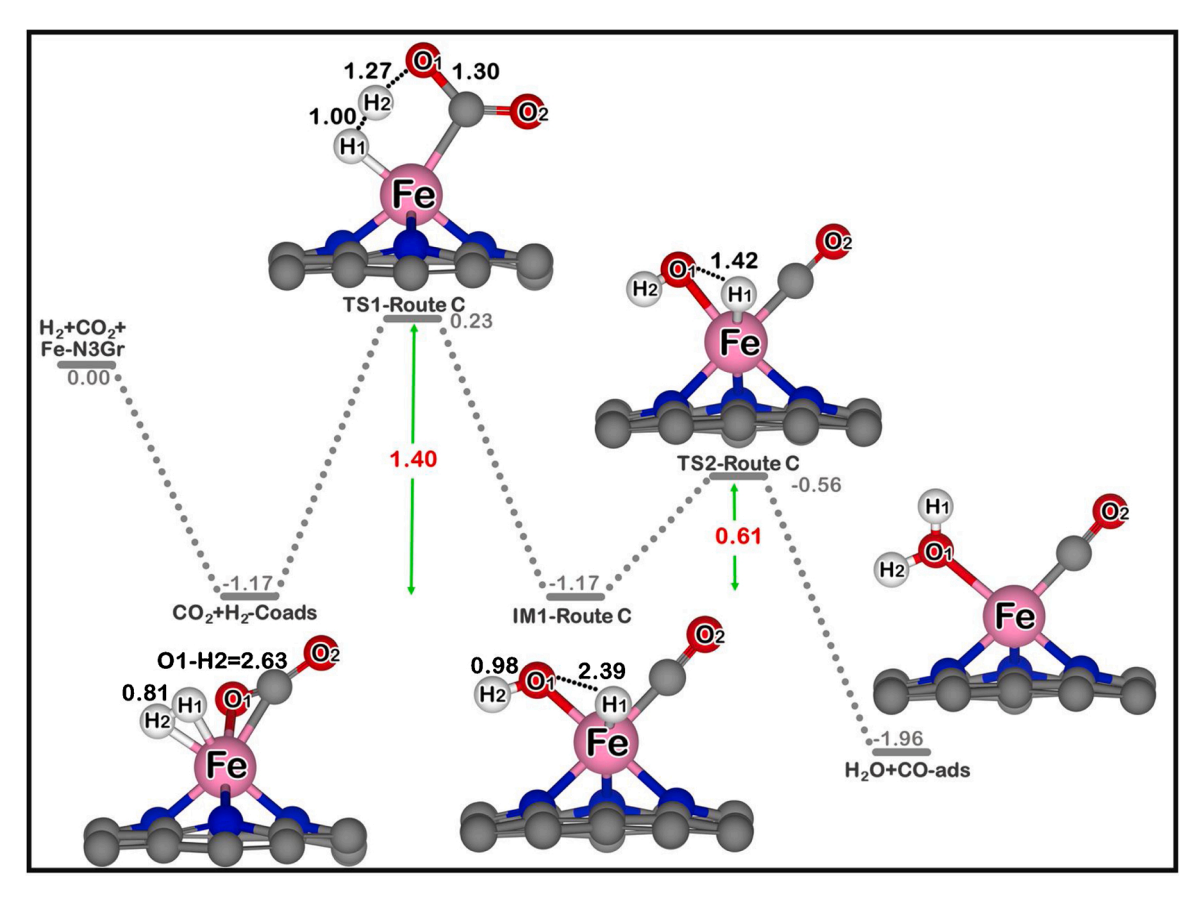


Fig. 8. Energy profile and the optimized stationary points for the CO_2 hydrogenation on Fe-N3Gr though Route-C. Distances are in Å.

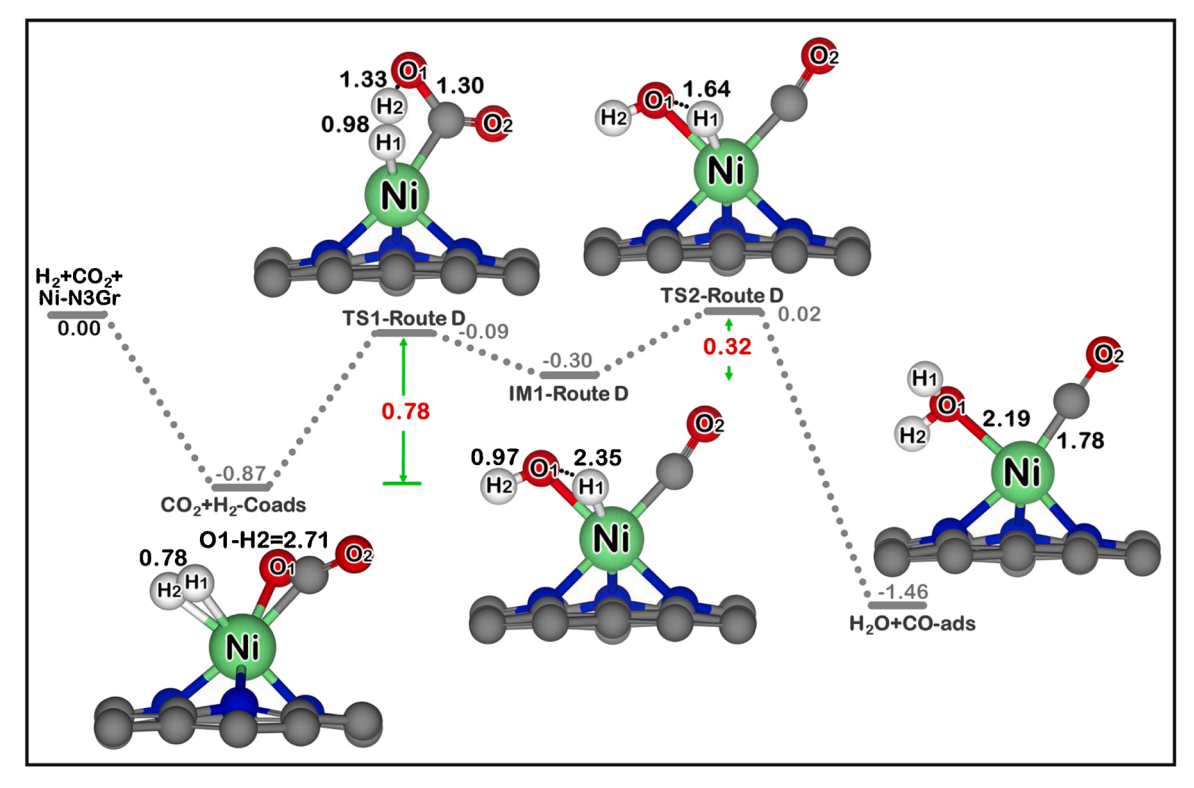


Fig. 9. Energy profile and the optimized stationary points for the CO_2 hydrogenation on Ni-N3Gr though Route-D. Distances are in Å.

hydrogenation was investigated to explore the mechanism of CO₂ conversion to formic acid on both surfaces and identify the most preferable reaction path and the rate-determining step. In this section, the microkinetic modeling was performed to calculate production rates of the CO2 hydrogenation on the surfaces under the experimental conditions. The total pressure in the current microkinetic modeling was set to 1 atm and a CO₂/H₂ ratio of 1 was used. The production rates of the CO₂ hydrogenation on the Fe-N3Gr and Ni-N3Gr catalysts as a function of temperature are presented in Fig. 10. The results show that the CO2 hydrogenation to trans-HCOOH displays the highest production rate with a maximum rate of 2.23 \times 10^2 and 2.30 \times $10^4\,s^{-1}$ at 450 and 350 K for Fe-N3Gr (Fig. 10a) and Ni-N3Gr (Fig. 10d) catalysts, respectively, indicating that the trans-HCOOH formation on Ni-N3Gr surface at 350 K is more favorable than that for Fe-N3Gr surface at 450 K. In addition, the maximum production rate of cis-HCOOH formation on both surfaces (Fig. 10b and e) are 6.67×10^{-3} and 6.86×10^{-3} s⁻¹ at 475 and 380 K, respectively, suggesting that the cis-HCOOH formation on the Ni-N3Gr surface can occur more favorable at lower temperatures. On the other hand, the optimum reaction temperature for the side products formation over the Fe-N3Gr (Fig. 10c) and Ni-N3Gr (Fig. 10f) catalysts are 550 and 500 K with a maximum rate of 1.09×10^{-6} and 2.80×10^{-3} s⁻¹, respectively, implying that the CO₂ reduction to CO is less competitive compared with the CO2 hydrogenation to trans-HCOOH at low temperatures. Our microkinetic modeling confirmed that CO2 hydrogenation to trans-HCOOH reaction is high activity and selectivity, especially NiN3Gr catalyst. However, the Fe-N3Gr and Ni-N3Gr catalysts reveal excellent catalytic activity and highly selective for the ${\rm CO_2}$ hydrogenation to trans-HCOOH.

Overall, we conclude that the *trans*-HCOOH formation is most likely to proceed better in low temperatures, while the *cis*-HCOOH and side products formation are most likely to proceed better in high temperatures. However, the $\rm CO_2$ reduction to side products (CO and $\rm H_2O$) is almost impossible due to the large E_a and low production rate. Thus, the Fe-N3Gr and Ni-N3Gr catalysts provide excellent reactivity and selectivity toward the $\rm CO_2$ hydrogenation to *trans*-HCOOH at low temperatures.

4. Conclusion

In this work, we used periodic DFT calculations to study the possible mechanisms for the $\rm CO_2$ catalytic hydrogenation to formic acid over the Fe-N3Gr and Ni-N3Gr surfaces. Our findings show that the $\rm CO_2$ hydrogenation on both surfaces are divided into 3 pathways, which are (I) the *trans*-HCOOH formation, (II) the *cis*-HCOOH formation, and (III) the CO and $\rm H_2O$ formation pathways. The *trans*-HCOOH formation is both thermodynamically and kinetically more favorable than the *cis*-HCOOH and side products formation. The rate-determining step of *trans*-HCOOH formation on the Fe-N3Gr (**Route-A2**) and Ni-N3Gr (**Route-B2**) are 0.57 and 0.37 eV, respectively, indicating that the catalytic activity on the Fe-N3Gr and Ni-N3Gr catalysts are higher than that for other catalysts, [25,

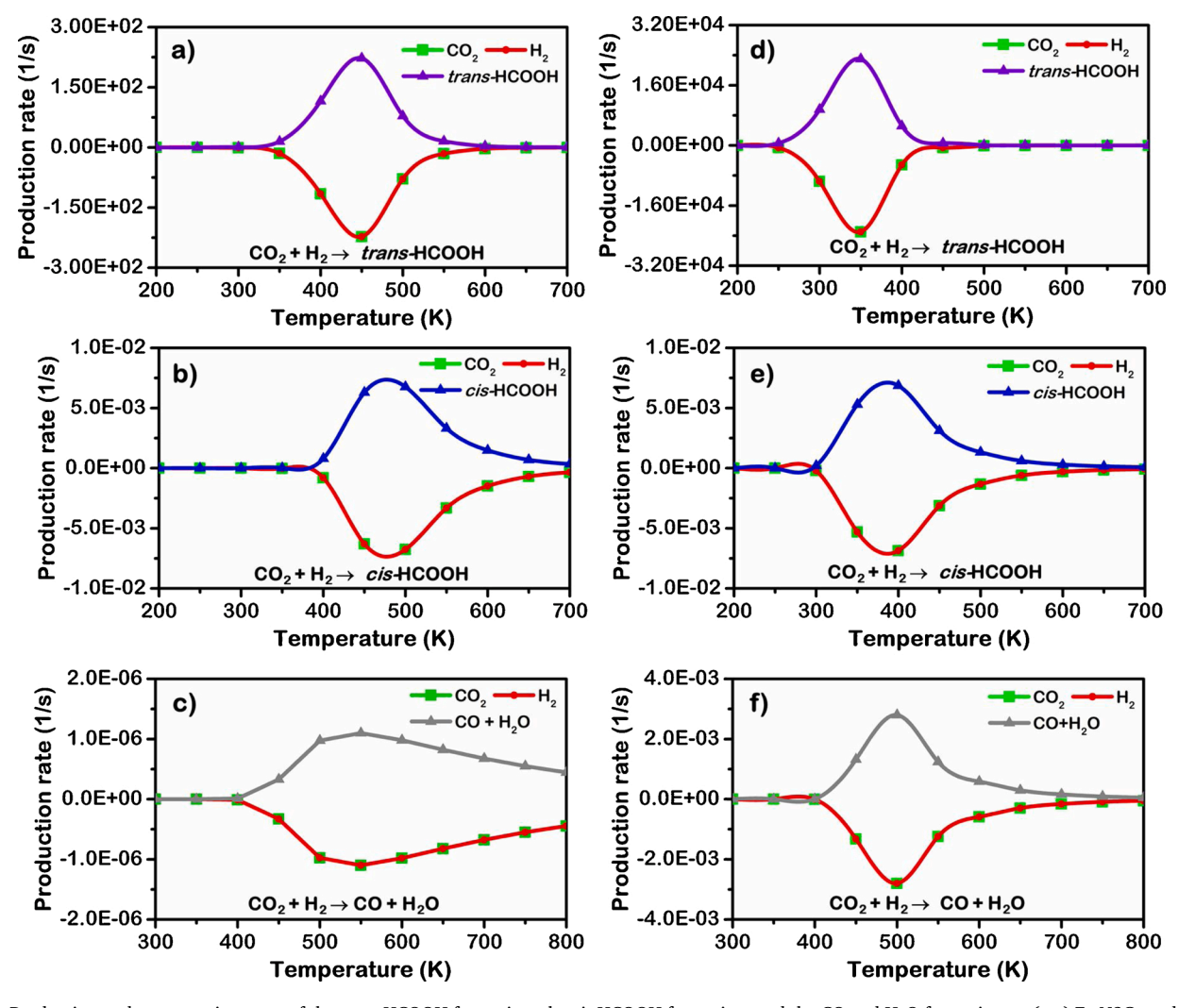


Fig. 10. Production and consumption rates of the *trans*-HCOOH formation, the *cis*-HCOOH formation, and the CO and H₂O formation on (a-c) Fe-N3Gr and (d-f) Ni-N3Gr surfaces as a function of temperatures.

27-29] [44,45,52,53,83], especially the Ni-N3Gr catalyst. The Ni-N3Gr has a highest catalytic activity for the CO2 hydrogenation to trans--HCOOH product. On the other hand, the CO₂ reduction to side products is almost impossible due to the large E_a value. The difference E_a between trans-HCOOH formation and side products formation on both surfaces are 0.83 and 0.41 eV, respectively, suggesting that the FeN3Gr and Ni-N3Gr surface provides excellent selectivity toward the CO₂ hydrogenation to trans-HCOOH product, especially the Fe-N3Gr surface. Moreover, our microkinetic modeling shows that the trans-HCOOH formation is most likely to proceed better in low temperatures, while the cis-HCOOH and side products formation are most likely to proceed better in high temperatures. Our calculation results suggest that the Fe-N3Gr and Ni-N3Gr catalysts provide excellent catalytic activity and is highly selective for CO₂ hydrogenation to trans-HCOOH. This theoretical investigation may shed light on other similar catalytic CO2 hydrogenation mechanisms to form value-added chemicals.

CRediT authorship contribution statement

Preeyaporn Poldorn: Data curation, Writing- Original draft preparation. Yutthana Wongnongwa: Methodology, Software, Validation. Tanabat Mudchimo: Reviewing and Editing. Siriporn Jungsutiwong: Conceptualization, Designing catalyst, Supervision, Writing- reviewing and editing.

Declaration of Competing Interest

The authors declare that they have no known competing financial interests or personal relationships that could have appeared to influence the work reported in this paper.

Acknowledgments

The authors would like to thank the Department of Chemistry, Faculty of Science, Ubon Ratchathani University, the National e-Science Infrastructure Consortium, and NANOTEC for their provision of computing resources. The authors also express their gratitude for financial support from the Royal Golden Jubilee PhD program (PHD/ 0203/2558) and Thailand Science Research and Innovation (RSA6280055). Financial support from the Center of Excellence for Innovation in Chemistry (PERCH-CIC), Ministry of Higher Education, Science, Research and Innovation is gratefully acknowledged.

References

- [1] Y. Liu, J. Zhao, Q. Cai, Phys. Chem. Chem. Phys. 18 (2016) 5491.
- [2] A. Tatar, A. Barati, A. Yarahmadi, A. Najafi, M. Lee, A. Bahadori, Int. J. Greenh. Gas Control. 47 (2016) 122.
- [3] D.A. Lashof, D.R. Ahuja, Nature 344 (1990) 529.
- [4] G. Centi, E.A. Quadrelli, S. Perathoner, Energy Environ. Sci. 6 (2013) 1711.
- [5] H. Liu, V.R. Cooper, S. Dai, D.-e. Jiang, J. Phys. Chem. Lett. 3 (2012) 3343.
- [6] V. Chandra, S.U. Yu, S.H. Kim, Y.S. Yoon, D.Y. Kim, A.H. Kwon, M. Meyyappan, K. S. Kim, Chem. Commun. 48 (2012) 735.
- [7] H.J. Yoon, J.H. Yang, Z. Zhou, S.S. Yang, M.M.-C. Cheng, Sens. Actuators B: Chem. 157 (2011) 310.
- [8] N.R. Stuckert, R.T. Yang, Environ. Sci. Technol. 45 (2011) 10257.
- [9] C.S. Martavaltzi, A.A. Lemonidou, Microporous Mesoporous Mater. 110 (2008)
- [10] C. Descamps, C. Bouallou, M. Kanniche, Energy 33 (2008) 874.
- [11] J.H. Cvejić, M. Rohmer, Phytochemistry 53 (2000) 21.
- A.G. Nasibulin, D.P. Brown, P. Queipo, D. Gonzalez, H. Jiang, E.I. Kauppinen, [12] Chem. Phys. Lett. 417 (2006) 179.
- [13] J. Lee, J. Kim, T. Hyeon, Adv. Mater. 18 (2006) 2073.
 [14] G. Centi, S. Perathoner, Catal. Today 148 (2009) 191.
- [15] K. Tedsree, T. Li, S. Jones, C.W.A. Chan, K.M.K. Yu, P.A. Bagot, E.A. Marquis, G. D. Smith, S.C.E. Tsang, Nat. Nanotechnol. 6 (2011) 302.
- [16] B. Loges, A. Boddien, F. Gärtner, H. Junge, M. Beller, Top. Catal. 53 (2010) 902.
- [17] F. Joó, ChemSusChem 1 (2008) 805.
- [18] P. Upadhyay, V. Srivastava, Present. Environ. Sustain. Dev. 10 (2016) 13.
 [19] M.D. Esrafili, F. Sharifi, L. Dinparast, J. Mol. Graph. Model. 77 (2017) 143.
- [20] G. Peng, S. Sibener, G.C. Schatz, S.T. Ceyer, M. Mavrikakis, J. Phys. Chem. C 116 (2012) 3001.

- [21] S.-Y. Wu, J.-J. Ho, J. Phys. Chem. C 116 (2012) 13202.
- [22] T. Maihom, S. Wannakao, B. Boekfa, J. Limtrakul, J. Phys. Chem. C 117 (2013) 17650.
- [23] S. Moret, P.J. Dyson, G. Laurenczy, Nat. Commun. 5 (2014) 4017.
- [24] L.T.M. Nguyen, H. Park, M. Banu, J.Y. Kim, D.H. Youn, G. Magesh, W.Y. Kim, J. S. Lee, RSC Adv. 5 (2015), 105560.
- J. Sirijaraensre, J. Limtrakul, Appl. Surf. Sci. 364 (2016) 241.
- [26] I. Chorkendorff, P. Taylor, P. Rasmussen, J. Vac. Sci. Technol. A: Vac. Surf. Films 10 (1992) 2277.
- [27] D.N. Sredojević, Ž. Šljivančanin, E.N. Brothers, M.R. Belić, ChemistrySelect 3 (2018) 2631.
- M.D. Esrafili, B. Nejadebrahimi, Appl. Surf. Sci. 475 (2019) 363.
- [29] M.D. Esrafili, L. Dinparast, Chem. Phys. Lett. 682 (2017) 49.
- [30] K. Motokura, D. Kashiwame, A. Miyaji, T. Baba, Org. Lett. 14 (2012) 2642.
- V. Mazumder, M. Chi, M.N. Mankin, Y. Liu, On. Metin, D. Sun, K.L. More, S. Sun, Nano Lett. 12 (2012) 1102.
- [32] M.A. Matin, J.-H. Jang, Y.-U. Kwon, J. Power Sources 262 (2014) 356.
- [33] D.E. Fein, I.E. Wachs, J. Catal. 210 (2002) 241.
- [34] E. Vesselli, L. De Rogatis, X. Ding, A. Baraldi, L. Savio, L. Vattuone, M. Rocca, P. Fornasiero, M. Peressi, A. Baldereschi, J. Am. Chem. Soc. 130 (2008) 11417.
- [35] T. Fujitani, Y. Choi, M. Sano, Y. Kushida, J. Nakamura, J. Phys. Chem. B 104
- [36] R. Zhang, M. Yang, M. Peng, L. Ling, B. Wang, Appl. Surf. Sci. 465 (2019) 730.
- [37] M.D. Esrafili, P. Mousavian, Int. J. Quantum Chem. 119 (2019), e25857.
- [38] S. Kattel, P. Atanassov, B. Kiefer, Phys. Chem. Chem. Phys. 15 (2013) 148.
- [39] S. Liu, S. Huang, Carbon 115 (2017) 11.
- [40] X. Liu, Y. Sui, T. Duan, C. Meng, Y. Han, Catal. Sci. Technol. 5 (2015) 1658.
- [41] A.K. Geim, K.S. Novoselov, Nanoscience and Technology: a Collection of Reviews From Nature Journals, World Scientific, 2010, p. 11.
- [42] Balandin, A.; Ghosh, S.; Bao, W.; Calizo, I.; Teweldebrhan, D.; Miao, F.; Lau, C. arXiv preprint arXiv:0802.1367 2008.
- A. Balandin, S. Ghosh, D. Teweldebrhan, I. Calizo, W. Bao, F. Miao, C. Lau, in: 2008 IEEE Silicon Nanoelectronics Workshop, IEEE, 2008, p. 1.
- [44] G. Yan, Z. Gao, M. Zhao, W. Yang, X. Ding, Appl. Surf. Sci. (2020), 146200.
- [45] N. Yodsin, C. Rungnim, S. Tungkamani, V. Promarak, S. Namuangruk, S. Jungsuttiwong, J. Phys. Chem. C 124 (2019) 1941.
- [46] A.A. Balandin, S. Ghosh, W. Bao, I. Calizo, D. Teweldebrhan, F. Miao, C.N. Lau, Nano Lett. 8 (2008) 902.
- [47] M.D. Esrafili, S. Asadollahi, Appl. Surf. Sci. 463 (2019) 526.
- [48] S. Kabir, K. Artyushkova, B. Kiefer, P. Atanassov, Phys. Chem. Chem. Phys. 17 (2015) 17785.
- [49] S. Kattel, P. Atanassov, B. Kiefer, Phys. Chem. Chem. Phys. 16 (2014) 13800.
- [50] X. Bai, E. Zhao, W. Wang, Y. Wang, K. Li, L. Lin, J. Yang, H. Sun, Z. Wu, RSC Adv. 7 (2017) 23812.
- [51] M. Wang, Z. Wang, RSC Adv. 7 (2017) 48819.
- [52] K. Homlamai, T. Maihom, S. Choomwattana, M. Sawangphruk, J. Limtrakul, Appl. Surf. Sci. 499 (2020), 143928.
- [53] J. Ma, H. Gong, T. Zhang, H. Yu, R. Zhang, Z. Liu, G. Yang, H. Sun, S. Tang, Y. Qiu, Appl. Surf. Sci. 488 (2019) 1.
- [54] Y. Meng, K. Li, D. Xiao, Y. Yuan, Y. Wang, Z. Wu, Int. J. Hydrogen Energy (2020).
- [55] Q. Zhao, J. Sun, S. Li, C. Huang, W. Yao, W. Chen, T. Zeng, Q. Wu, Q. Xu, ACS Catal. 8 (2018) 11863.
- [56] H.B. Yang, S.-F. Hung, S. Liu, K. Yuan, S. Miao, L. Zhang, X. Huang, H.-Y. Wang, W. Cai, R. Chen, Nat. Energy 3 (2018) 140.
- [57] H.R. Byon, J. Suntivich, Y. Shao-Horn, Chem. Mater. 23 (2011) 3421.
- [58] K. Artyushkova, A. Serov, S. Rojas-Carbonell, P. Atanassov, J. Phys. Chem. C 119 (2015) 25917.
- [59] P. Su, K. Iwase, S. Nakanishi, K. Hashimoto, K. Kamiya, Small 12 (2016) 6083. [60] S. Liu, C. Deng, L. Yao, H. Zhong, H. Zhang, J. Power Sources 269 (2014) 225.
- [61] A. Morozan, V. Goellner, Y. Nedellec, J. Hannauer, F. Jaouen, J. Electrochem. Soc. 162 (2015) H719.
- [62] B. Delley, J. Chem. Phys. 92 (1990) 508.
- [63] B. Delley, J. Chem. Phys. 113 (2000) 7756.
- [64] B. Delley, Phys. Rev. B 66 (2002), 155125.
- [65] S. Grimme, J. Comput. Chem. 25 (2004) 1463.
- [66] S. Grimme, J. Comput. Chem. 27 (2006) 1787.
- [67] T.A. Halgren, W.N. Lipscomb, Chem. Phys. Lett. 49 (1977) 225.
- N. Govind, M. Petersen, G. Fitzgerald, D. King-Smith, J. Andzelm, Comput. Mater. Sci. 28 (2003) 250.
- [69] S. Kattel, P. Atanassov, B. Kiefer, J. Phys. Chem. C 116 (2012) 8161.
- [70] I.A. Filot, R.A. van Santen, E.J. Hensen, Angew. Chemie 126 (2014) 12856.
- [71] P. Nitoń, A. Żywociński, M. Fiałkowski, R. Hołyst, Nanoscale 5 (2013) 9732.
- [72] A.P.J. Jansen, An Introduction to Kinetic Monte Carlo Simulations of Surface Reactions, Vol. 856, Springer, 2012.
- [73] S. Zhang, S. Tsuzuki, K. Ueno, K. Dokko, M. Watanabe, Angew. Chemie Int. Ed. 54 (2015) 1302.
- [74] L. Zhao, R. He, K.T. Rim, T. Schiros, K.S. Kim, H. Zhou, C. Gutiérrez, S. Chockalingam, C.J. Arguello, L. Pálová, Science 333 (2011) 999.
- [75] H. Gao, L. Song, W. Guo, L. Huang, D. Yang, F. Wang, Y. Zuo, X. Fan, Z. Liu, W. Gao, Carbon 50 (2012) 4476.
- [76] C.V. Rao, C.R. Cabrera, Y. Ishikawa, J. Phys. Chem. Lett. 1 (2010) 2622.
- T. Xing, Y. Zheng, L.H. Li, B.C. Cowie, D. Gunzelmann, S.Z. Qiao, S. Huang Y. Chen, ACS Nano 8 (2014) 6856.
- H. Liu, Y. Liu, D. Zhu, J. Mater. Chem. 21 (2011) 3335.
- [79] X. Zhang, Z. Lu, Z. Yang, J. Mol. Catal. A: Chem. 417 (2016) 28.

- [80] Y. Yang, J. Evans, J.A. Rodriguez, M.G. White, P. Liu, J. Chem. Soc. Faraday Trans. 12 (2010) 9909.
 [81] L. Grabow, M. Mavrikakis, ACS Catal. 1 (2011) 365.

- [82] G. Gao, Y. Jiao, E.R. Waclawik, A. Du, J. Am. Chem. Soc. 138 (2016) 6292. [83] Z. Ou, C. Qin, J. Niu, L. Zhang, J. Ran, Int. J. Hydrogen Energy 44 (2019) 819.

\$ SUPER

Contents lists available at ScienceDirect

Molecular Catalysis

journal homepage: www.journals.elsevier.com/molecular-catalysis





Mechanistic insight into catalytic carbon dioxide hydrogenation to formic acid over Pt-doped boron nitride nanosheets

Yuwanda Injongkol^a, Ratchadaree Intayot^a, Nuttapon Yodsin^a, Alejandro Montoya^b, Siriporn Jungsuttiwong^{a,*}

a Department of Chemistry and Center of Excellence for Innovation in Chemistry, Faculty of Science, Ubon Ratchathani University, Ubon Ratchathani 34190, Thailand

ARTICLE INFO

Keywords: DFT CO₂ Hydrogenation Pt-Boron nitride nanosheets Formic acid

ABSTRACT

In this work, we investigated the mechanism of CO_2 hydrogenation over the Pt-doped boron nitride nanosheets (Pt-BNNSs) by using the density functional theory (DFT). It is found that a Pt adatom can be effectively stabilized in boron vacancy site (Pt-BV). Our investigation shows that the reaction mechanisms of CO_2 hydrogenation over Pt-BV can be found in three possible reaction pathways: (i) co-adsorption, (ii) H_2 dissociation, and (iii) co-adsorption together with H_2 dissociation pathways. The co-adsorption together with H_2 dissociation provides the most favorable pathway among of these three proposed mechanisms. The important finding of our study is that the presence of CO_2 in step of hydrogen dissociation plays an important role in producing the FA on the Pt-BV catalyst. Moreover, we found that the hydrogenation of CO_2 via carboxylate (COOH) has the rate-determining step of 0.63 eV in the step of hydrogen dissociation. In addition, the microkinetic modelling suggests that the COOH route is found to be more energetically and kinetically feasible rather than that it is formate route (HCOO) with the reaction temperature at 350 K and pressure of 5 bar. Our calculation results provide an important information for developing Pt-BV catalysts and might shed light on experimental design the novel Pt-BV catalyst for the CO_2 hydrogenation and the conversion of greenhouse gases into value-added products.

1. Introduction

Carbon dioxide is one of the main greenhouse gases released by industry, power plants, fuel combustion, and other human activities, and is involved in environmental issues, including drought, haze, rising food prices, rising sea levels, rising temperature, and melting glaciers. [1–3] The conversion of CO2 to valuable chemicals such as formic acid (HCOOH), formaldehyde (HCOH), methanol (CH₃OH) and methane (CH₄) have received large attention from environmental and industrial sectors. In 2016, Kattel and co-worker[4] investigated the CO2 hydrogenation over Pt nanoparticles supported on SiO₂ and TiO₂ to produce the HCOOH, CO, HCOH, CH₃OH, and CH₄ products on both experimental and theoretical study. Moreover, Liu and co-worker [5] reported methanol synthesis from CO2 hydrogenation on PdCu3(111) surface by DFT study. The typical possible mechanisms to produce valuable products have been proposed including (i) Reverse Water Gas Shift (RWGS) + CO-hydro pathways (ii) formate pathways (iii) carboxyl pathway. Among valuable chemicals, FA is important reactant for numerous applications, for the example, in the production of plastics, plywood, paints, explosives, and petrochemicals.[6,7] Furthermore, FA is an effective hydrogen storage material for an excellent fuel cells[8,9] that can play an instrumental role in the overall implementation of a hydrogen economy because It has a hydrogen density of 53 g. of H₂ per liter, low toxicity, and as a smallest organic hydrogen carrier (LOHC). Currently, commercial processes for formic acid production involve hydrolysis of methyl formate or direct synthesis from carbon monoxide and water. These traditional methods consume large quantities of energy and produce hazardous waste. Thus, the development of a clean method for FA synthesis is a high priority. CO₂ is a cheap and abundant source of carbon, and hydrogenation of CO₂, as shown by the equation $CO_2 + H_2 \rightarrow HCOOH$, provides a possible strategy to synthesize FA using CO2 as a raw material. Numerous catalysts have been reported to be active material for catalytic conversion of CO2, such as on zeolites, [10, 11] metal-organic frameworks (MOFs), [12-15] transition metal-based catalysts, such as Co, Ni, Cu, Pd, Ru, and Pt, [16-22] bimetallic clusters, [23-25], transition metal-graphene catalysts, [26-33] and

E-mail address: siriporn.j@ubu.ac.th (S. Jungsuttiwong).

^b School of Chemical and Biomolecular Engineering, The University of Sydney, Sydney, NSW 2006, Australia

^{*} Corresponding author

metal-boron nitride catalysts [34–44]. Noble metals such as Pt, Rh, and Pd are used as effective catalysts, [45,46] For instance, the electrochemical reduction of CO_2 on a Pt(111) surface has a small activation energy for proton–electron transfer.

Nowadays, a single-atom catalyst (SACs) have become a hot issue due to their significant advantages of reduced atomic utilization, gain much higher activity with excellent stability and selectivity, as well as improved its activity over conventional pure metal surfaces. As an analogue of graphene, hexagonal boron nitride nanosheets (h-BN) have been studied either theoretically or experimentally [34-43]. Owing to their useful properties, including high chemical stability, thermal conductivity, mechanical stiffness, wide optical bandgaps, strong ultraviolet emission spectra, and inert chemical substance, [47-49] h-BN nanomaterials have been used as a superior supporter with a high catalytic activity through doping various transition metals by electron beam irradiation [50] or solvent exfoliation [51]. Currently, single-TM-doped BN nanomaterials have been published as efficient catalysts in numerous reactions such as CO oxidation, [37-40,52-54] and oxygen reduction reaction [55,56]. Pt single atom catalyst is a powerful with excellent performance, cost reduction and notable catalytic activity and selectivity, while surface atoms of suitable supports, which not only maximize the atomic efficiency of metals, but also provide an alternative to tune the activity and selectivity of catalytic reactions. Interestingly, there is a theoretical investigation for the stability and activity of a single atomic Pt atom bonded to h-BN (Pt-BN) via CO oxidation to produce CO₂ for air treatment application. The Pt atom can stabilize on the boron vacancy site. Pt-BV also showed a strong interaction that confirms by formation energy, binding energy and partial density of state [38]. In addition, Du and coworkers reported that a boron monovacancy provides a lower formation energy than a nitrogen monovacancy does, resulting in the boron vacancy on h-BN was the preferable one [57]. Recently, researchers investigated a metal-doped boron nitride monolayer as a promising single-atom electrocatalyst for CO2 conversion [34,58]. The DFT study provided an understanding of how single transition metal atoms such as Sc to Zn, Mo, Rh, Ru, Pd, Ag, Pt, and Au supported on a boron monovacancy monolayer, function as electrocatalysts for CO₂ reduction to CH₄. The study reveals that Fe, Co, Pt on defective BN provide outstanding electrocatalytic activities for electrocatalytic reduction (ECR) of CO2 to CH4. The superior catalytic activity of BN nanomaterials in various applications have inspired us to investigate whether the materials can be efficient catalysts for CO2 hydrogenation to FA. To answers the question, we then report a theoretical investigation into the structures, energetics, stability, and properties of Pt-BNNSs, Pt-NV, and Pt-BV, as well as their performances in the hydrogenation of CO2 to formic acid. To the best of our knowledge, the results provided insight and guidance to experimentalists in the fields of low cost, high efficiency SACs for converting CO2 to useful hydrocarbon

Herein, we report theoretical investigations into the structures, energetics, stability, and properties of Pt-BNNSs. This manuscript is the first investigation of the hydrogenation of CO_2 over Pt-BNNSs. Also, we studied the mechanisms of CO_2 hydrogenation on Pt-BNNSs in the details. The reactions mechanisms were proposed within three possible reaction pathways, namely, co-adsorption, H_2 dissociation and co-adsorption together with H_2 dissociation pathways. Our studied results show how the CO_2 in the step of hydrogen dissociation can be helpful for decreasing the energy barrier of the CO_2 hydrogenation reaction. In addition, the microkinetics simulation for CO_2 hydrogenation on Pt-BNNSs were discussed. Consequently, this study might be helpful to preserve the environment.

2. Computational details

2.1. DFT calculations

All structural optimizations were performed using density functional

theory (DFT) with the DMol³ module in the Materials Studio software package (version 7.0) [59,60]. Exchange and correlation interactions were based on a generalized gradient approximation (GGA) using the Perdew-Burke-Ernzerhof (PBE) functional [61]. We applied the density functional all electron for the relativistic effects of transition metal atoms [34,38,39,62]. The localized double numerical basis set combined with polarization functions (DNP) was applied for all atoms to expand the Kohn-Sham orbitals. The DNP basis set is comparable to 6-31G** Gaussian basis sets; [63] providing better accuracy for a similarly sized basis set. The DFT-D correction method was applied by using the Tkatchenko-Scheffler (TS) scheme [64]. All calculations were performed with a real-space global orbital cutoff radius of 4.0 Å and the convergence tolerances for geometry optimization were set to 10⁻⁵ Ha for a given energy, a force of 0.004 Ha/Å, and a displacement of 0.005 Å. The electronic SCF tolerance was set to 10^{-5} Ha. A k-point set $5\times5\times1$ was used for supercell calculations, while 15×15×1 grid was used for the electronic properties. The Hirshfeld charge density analysis [65] was used to calculate atomic charges and charge-transfer values. The complete linear synchronous transit (LST)/quadratic synchronous transit (QST) calculations were performed to locate transition states (TS) [53]. The 5×5 bare hexagonal boron nitride (h-BN) supercells was used in a periodic system with a vacuum of 24 Å.

To confirm the stability of the mono-vacancy on BNNSs, we then have calculated the formation energy (E_f) of the nitrogen vacancy (NV) and the boron vacancy (BV) on BN, which can be performed by using the equation:

$$E_f(V_i) = E(V_i) - E(P) + \mu_i$$

where, $E_f(V_i)$ is the total energy of the supercell containing the vacancy BN, E(P) is the total energy of the pristine BNNSs, and μ_i is a chemical potential of atom i (B or N). Chemical potential of N and B atoms are obtained by N₂ molecule and metallic α -B phase, respectively. Moreover, the calculated binding energies (E_b) and adsorption energies (E_{ads}) are defined as:

$$E_{\rm b} = E_{\rm (system)} - E_{\rm (BNNSs)} - E_{\rm (Pt)}$$

where, $E_{(\text{BNNSs})}$ is the total energy of Pt-BNNSs. $E_{(\text{BNNSs})}$ is energy of pristine BNNSs and $E_{(\text{Pt})}$ is the energy of atomic Pt.

Gas adsorption on Pt-BNNSs surfaces are determined through the adsorption energy (E_{ads}) calculations using the equation

$$E_{\rm ads} = E_{\rm (complex)} - E_{\rm (Pt-BNNSs)} - E_{\rm (adsorbate)}$$

where $E_{({\rm complex})}$, $E_{({\rm Pt-BNNSs})}$, and $E_{({\rm adsorbate})}$ are the total energies of adsorbate molecules adsorbed on BNNSs, Pt-BNNSs surfaces and adsorbate molecules, respectively. According to these expressions, a more negative value of $E_{\rm b}$ and $E_{\rm ads}$ means stronger interactions.

2.2. Microkinetic simulations

All Microkinetic simulations of CO₂ hydrogenation pathways were carried out by means of the MKMCXX software package [66,67]. For surface reactions, the rate constants for the forward and backward elementary reactions were given by the Eyring equation.

$$k = A e^{-\frac{E_a}{k_b T}}$$

where $k,\,k_b,\,T,$ and E_a are the reaction rate constant, Boltzmann constant temperature in Kelvin, and the activation barrier, respectively. The prefactor A can be obtain by

$$A = \frac{k_B T}{h} \times \frac{Q_{vib}^{\ddagger (3N-7)}}{Q_{vib}^{(3N-6)}}$$

where h and k_B are the Plank and Boltzmann constants, respectively. $Q_{vib}^{\dagger(3N-7)}$ and $Q_{vib}^{(3N-6)}$ are the vibrational partition functions of the tran-

sition state and initial state in the surface reaction, respectively. Based on the manual of MKMCXX software, pre-factor for all surface elementary reaction steps is approximately $10^{13}~{\rm s}^{-1}$.

For non-activated molecular, the gas surface adsorption and desorption rates are described by the Hertz-Kundsen equation [68]

$$k_{ads} = S \frac{PA}{\sqrt{2\pi m k_b T}}$$

$$k_{des} = A \frac{k_b T^3}{h^3} \frac{2\pi k_b}{\sigma \theta_{rot}} exp \left(\frac{-E_{des}}{RT} \right)$$

Here A, m, σ , $\theta_{\rm rot}$, S, and P represent the area of the surface site to be adsorbed upon, the mass of the molecule, the symmetry number, the characteristic temperature for rotation, the sticking coefficient (assumed to be 1.0), and the partial pressure of adsorbate in the gas, respectively. For desorption, it is assumed that there are three rotational degrees of freedom and two translational degrees of freedom in the transition state.

3. Results and discussion

3.1. Structural and electronic properties of Pt-BNNSs, Pt-NV and Pt-BV catalyst

Fig. 1 shows optimized structures for the 5×5 supercell of (a) boron nitride nanosheets (BNNSs) (b) nitrogen vacancy (NV), (c) boron vacancy (BV). Our calculation provides the calculated in-plane lattice parameter for the relaxed hexagonal primitive unit cell is 2.51 Å (a=b), which is in agreement with the experimental value of 2.505 Å. The corresponding B–N, B–B, and N–N bond distances are 1.45, 2.53, and 2.53 Å for BNNSs, NV and BV surfaces, respectively [69]. For pristine BNNSs, all possible sites of Pt adatom on BNNSs are obtained to yield a stable Pt-BNNSs configuration. The site of interest consists of top N and B sites, bridge site (B), and hollow site (H), as demonstrated in Fig. 1a. From the geometry optimization, we found that the most stable Pt binding site on BNNSs sheet is located at N1 site with the binding energy of -0.73 eV. The calculated Pt–N is approximately 2.37 Å (Fig. 2a). The

hollow and top boron sites are also studied as shown in Fig. S1. To understand interaction between metal and substrates, the partial density of states (PDOS) projected on the 4*d*-orbital of Pt atom and 2*p*-orbitals of atop N atom are given in Fig. 2b. Moreover, the structural properties of the most stable Pt-BNNSs are illustrated in Table 1. The Hirshfeld atomic charges of Pt is 0.077*e* while the nearest N atom are detected around –0.169*e*, suggesting that the Pt atom transfer electrons to nitrogen atom. A similar phenomenon was found in the previous work [43,70]. This charge transfer provides an active site of Pt for further reaction mechanism.

The E_f of NV and BV are calculated to be 7.70 eV and 11.28 eV, respectively. These results indicate that the vacancy of BV is more difficult to form compared to NV. However, our calculation results are in good agreement with the formation energy of previous theoretical studies (E_f of BV > E_f of NV) [71–73]. Additionally, in term of experiment, the vacancy sites in boron nitride nanostructures can be synthesized by electronic irradiation [73,74] or solvent exfoliation [51]. The electron beam or electronic irradiation processing is the process that involves using the electrons of high energy to treat an object for a variety of proposes. For the example, the defects in boron nitride monolayer created by irradiation damage, such as the boron and nitrogen monovacancies (V_B and V_N) [50]. The single layer of BNNSs can be prepared by electron beam irradiation at 120 kV inside the TEM. During the electron beam thinning process, many lattice defects such as vacancies have been formed. Therefore, both BV and NV have been already synthesized.

We generated the mono-vacancy on BNNSs by removing B or one N atom from the BNNSs, so-called boron vacancy (BV) and nitrogen vacancy (NV), respectively. Then, we initially put Pt atom on vacant site of N atom connecting to three neighboring B atoms. Form the calculation, the Pt atom is preferably located on N hole in NV sheet with the strong binding energy of -3.66 eV, confirming the formation via chemical bonding between Pt adatom and neighboring N atoms on the surface. The average bond distances between the Pt atom and three B atoms are around 2.14 Å (Fig. 2c). To explain why the Pt atom gives a strong binding capability on BV rather than BNNSs, we have investigated

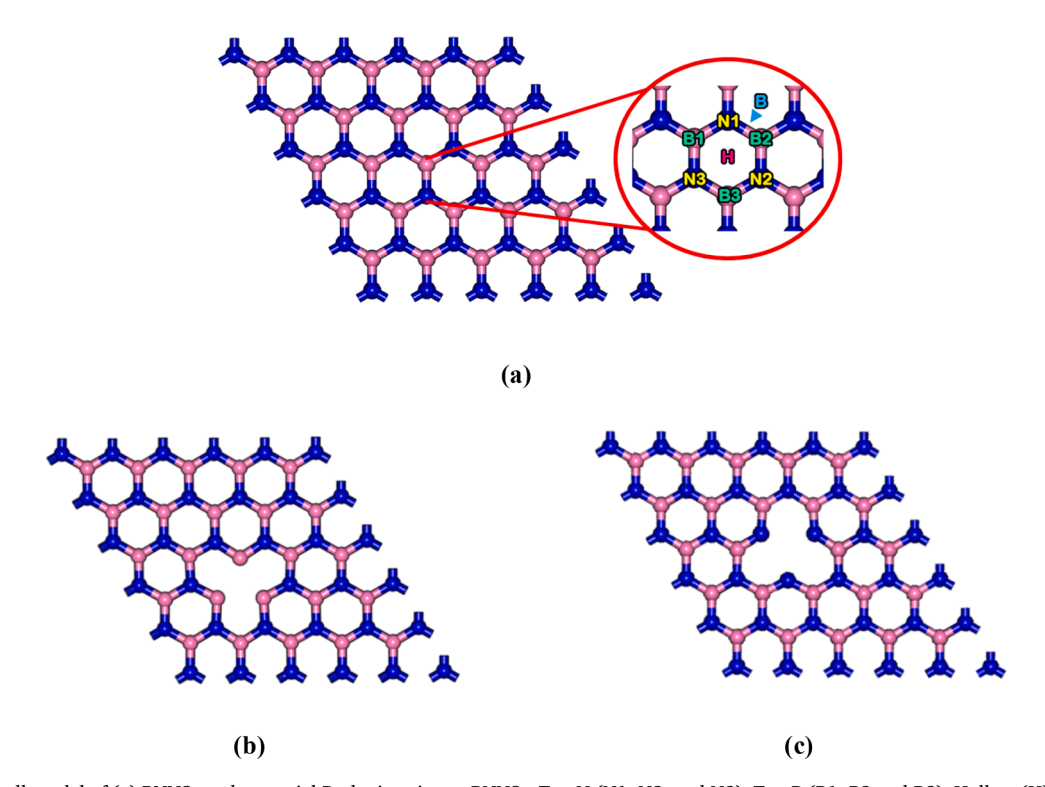


Fig. 1. 5 × 5 supercell model of (a) BNNSs and potential Pt doping site on BNNSs: Top N (N1, N2, and N3), Top B (B1, B2 and B3), Hollow (H), and Bridge (B), (b) NV, and (c) BV. The pink and blue balls represent B and N atoms, respectively.

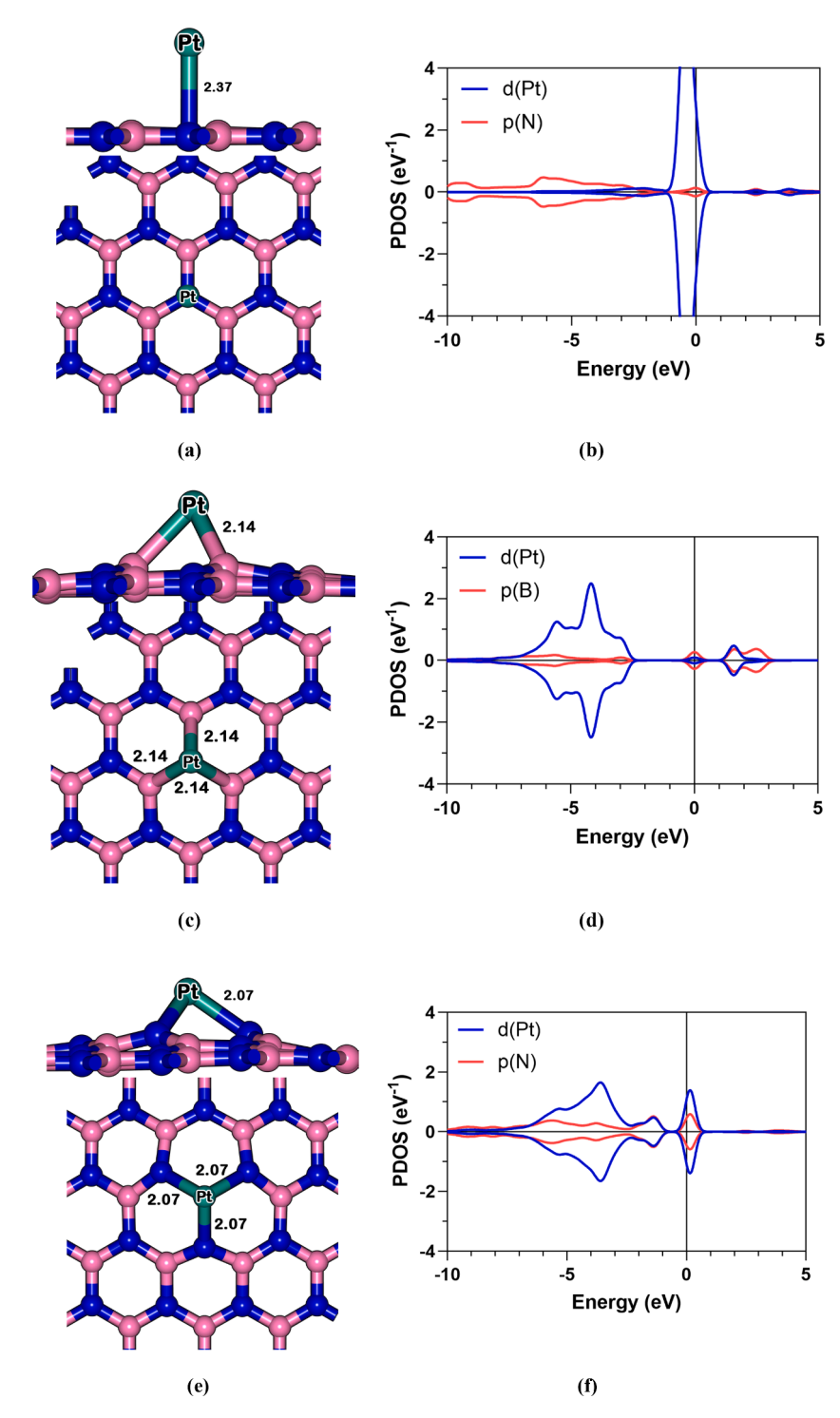


Fig. 2. The optimized structures and PDOS of (a, b) Pt-BNNSs, (c, d) Pt-NV and (e, f) Pt-BV.

Table 1 Binding energies ($E_{\rm b}$), geometric parameters, and Hirshfeld atomic charges for Pt doped on various substrates ($\Delta Q_{\rm Pt.}$

Surfaces	E _b (eV)	d _{Pt-B} (Å)	d _{Pt-N} (Å)	ΔQ _{Pt} (e)
BNNSs	-0.73	-	2.37	0.0768
NV	-3.66	2.14	-	0.1573
BV	-4.41	-	2.07	0.4668

density of state calculation. The partial density of state (PDOS) of Pt-NV are provided in Fig. 2d. Compared to Pt-BNNSs, we found more strong electronic coupling between the 4d state of Pt and the p orbitals of NV substrate for Pt-NV, as depicted by more overlap peak. In the case of Pt-BV structure, the single Pt atom stably adsorbs on three unsaturated N atoms with slightly high binding energy of -4.41 eV. The three Pt-N bond length are calculated to be approximate 2.07 Å, which is similar to published works [70,75]. Remarkably, in Pt-BV system the orbital hybridization between Pt 4d state and 2p orbitals of N are more strongly overlapped than that in Pt-NV, indicating the stable formation of Pt-N bond. To gain more in-depth insight into the charge transfer for catalytic

prediction, the simulated Hirshfeld atomic charges are tabulated in Table 1. We found the positive charge of Pt atom on either NV or BV, providing that the Pt atom on monovacancy BNNSs would give a catalytic site for further CO_2 hydrogenation reaction. In addition, we predict that the Pt atom on Pt-BV might be the most active site for the reaction as found in previous studies either experimental or theory [50,57].

In general, the strong interaction between 3d-orbitals of the Pt and 2p-orbitals of the N atoms make very stable of Pt-BV. Therefore, Pt-BV may exhibit higher reactivity in activation of adsorbed ${\rm CO}_2$ and ${\rm H}_2$ for ${\rm CO}_2$ hydrogenation.

3.2. Adsorption of CO₂ and H₂ and co-adsorbed CO₂ and H₂ on Pt-BV

Next, we initially study all possible adsorption configurations of ${\rm CO}_2$, ${\rm H}_2$, and co-adsorbed ${\rm CO}_2$ and ${\rm H}_2$ to obtain the most stable configurations over Pt-BV. The most energetically feasible adsorption configurations of all gasses are shown in the Fig. 3. The adsorption energy of ${\rm CO}_2$ on Pt-BV material is -0.34 eV, which is larger than that it is the adsorption on perfect BNNSs (-0.21 eV). In addition, the Pt-O intermolecular bond is measured to be 2.62 Å. This interaction is confirmed by PDOS (Fig. 3b). We found Pt *d*-orbitals overlap *p*-orbitals of ${\rm CO}_2$ in the range of -4.0 to -10.0 eV below the Fermi level, resulting in a strong interaction between

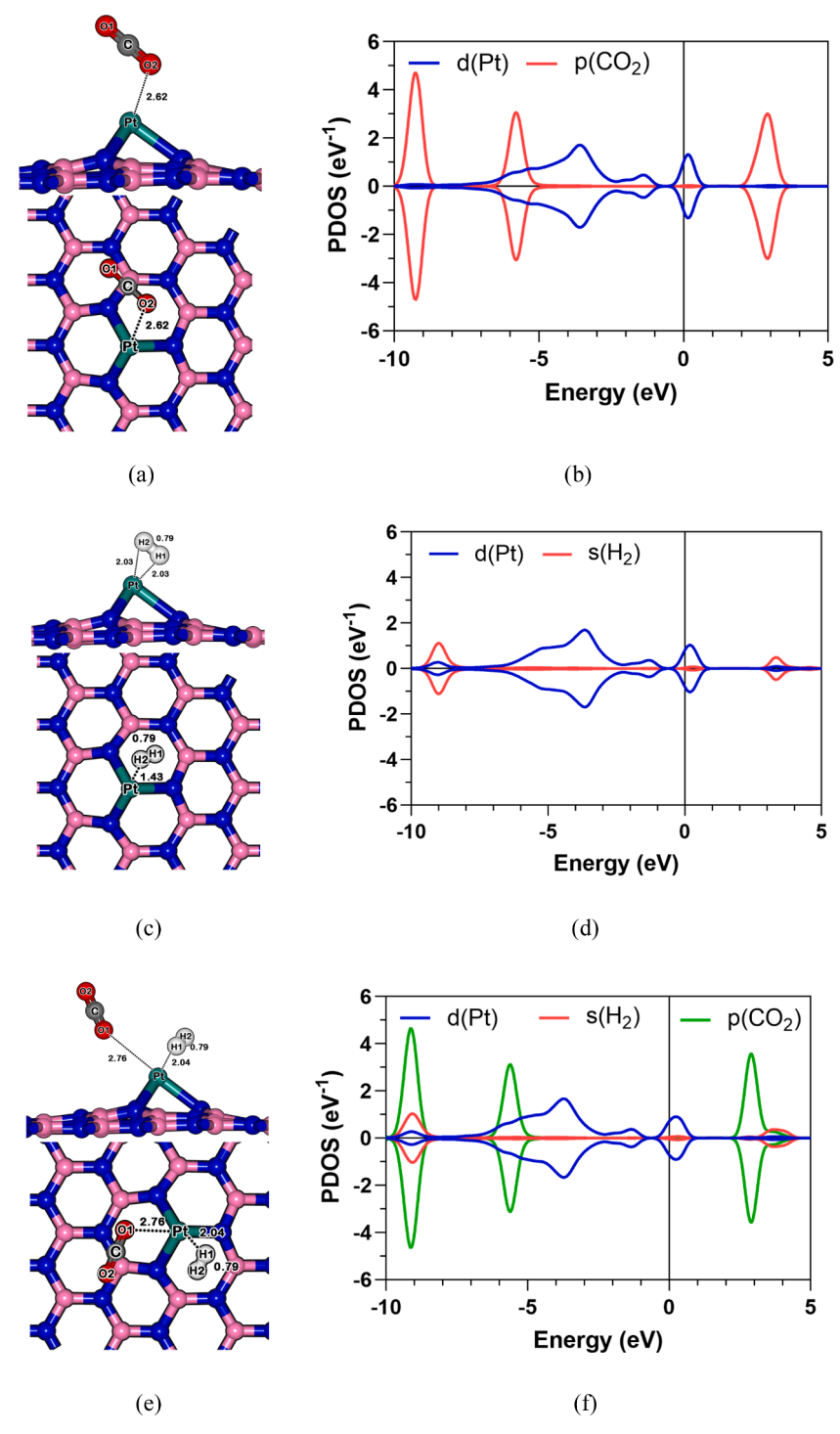


Fig. 3. Optimized structures, some geometric parameters and PDOS for (a, b) CO2, (c, d) H2 (e, f) and CO2 with H2 co-adsorbed on Pt-BV.

the Pt and CO $_2$ molecule. In case of H $_2$ adsorption, the adsorption energy of H $_2$ is equal to -0.29 eV with the Pt–H bond length of 2.03 Å as illustrated the optimized structure in Fig. 3c. The H1–H2 bond distance is 0.79 Å, implying the K-mode adsorption [76]. According to Fig. 3d, PDOS plots reveals orbital hybridization between H s-orbital and d-orbitals of Pt atom at -8.0 to -10.0 eV, which is the characteristic K-mode adsorption peak[76]. Moreover, we also considered the co-adsorption of H $_2$ and CO $_2$ gas molecules. Compared to individual gas adsorptions, the co-adsorption mode is slightly higher than those. The computed Pt–O and Pt–H are 2.76 and 2.04 Å, respectively. The co-adsorption energy is calculated to be -0.48 eV. To see the interaction insight, we analyzed the PDOS (see in Fig. 3f). It is found a strong hybridization between s- and p-orbital of the adsorbate gases and d-orbital of Pt atom on BV sheet in range of -10.0 to 0.0 eV, confirming that either H $_2$ or CO $_2$ can cover the catalyst for further reaction.

One possibility of defective BNNSs surface is the Pt-NV system. The activity of CO_2 or H_2 on Pt-BV and Pt-NV are clearly compared in Table S1. From our simulation, we are strongly sure that the adsorption properties of Pt-NV provide a lower activity rather than that of Pt-BV due to its smaller gas adsorption energies. The CO_2 gas is adsorbed on a catalytic Pt site on Pt-BV with a tiny adsorption energy of only -0.28

eV. The calculated Pt-O intermolecular bond distance is calculated to be 3.66 Å, which is larger than in the case of CO₂ adsorption on Pt-BV. In addition, there is small electron transfer from the CO2 to Pt-NV substrate compared to Pt-BV obtained by Hirshfeld charge analysis as showed Table S1. The hydrogen adsorption energy on BV is calculated to be -0.29 eV with Pt-H bond length of 2.03 Å, which is higher than the adsorption of H₂ on NV ($E_{ads} = -0.15$ eV). Moreover, the electron transfer from hydrogen gas to Pt-NV is only |0.004|e, which is smaller than that it is Pt-BV. At the same manner in co-adsorbed CO2 and H2 on Pt-NV, the adsorption energy is lower by 0.10 eV. The computed Pt-O and Pt-H intramolecular bond are 3.32 and 2.15 Å, respectively, providing longer than the reaction on Pt-BV surface. From our evidences, we found that the adsorption energies of CO2, H2, and coadsorbed on Pt-BV are higher than that of Pt-NV, which are corresponding to either structural or electronic properties. Therefore, due to a higher gas adsorption energy over Pt-BV surface, we then use this catalyst for further calculation with expectation that the reaction would feasibly occur on Pt-BV rather than it is Pt-NV.

(a) a co-adsorption mechanism

(b) a H₂ dissociation and a co-adsorption together with H₂ dissociation

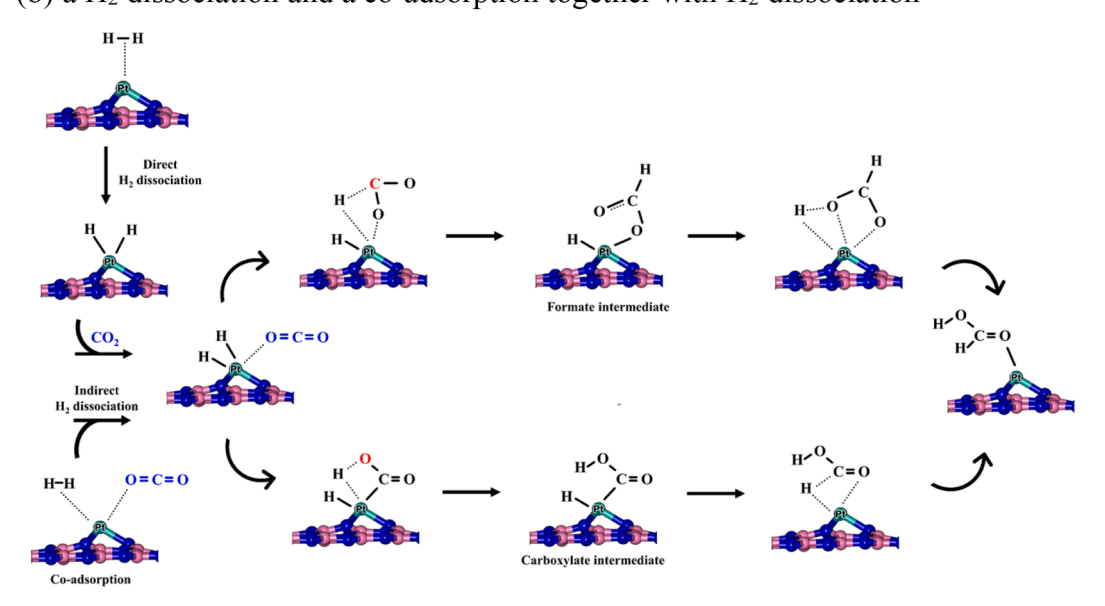


Fig. 4. All possible reaction mechanisms of CO2 hydrogenation into formic acid.

3.3. CO₂ hydrogenation to formic acid on the Pt-BV catalyst

Recently, the CO_2 interaction and its hydrogenation reaction on Pt-BV has not previously been considered by means of a theoretical point of view. Herein, we then investigated the reaction mechanism to predict the rate of reactions, kinetics and thermodynamics. We have broken down the reaction mechanisms of the CO_2 hydrogenation to formic acid (FA) into two main possible reaction pathways; (a) a co-adsorption mechanism, (b) a H_2 dissociation and a co-adsorption together with H_2 dissociation as showed in Fig. 4.

3.3.1. CO2 hydrogenation on Pt-BV via Co-adsorption mechanism

The hydrogenation CO₂ to FA through co-adsorption pathway begins with the co-adsorption of CO2 and H2 at the Pt catalytic site with the adsorption energy of -0.48 eV. Then, the CO2 is hydrogenated into FA via two main different intermediates, namely, formate- and carboxylateintermediate. Fig. 5 provides energetic profiles of formate and carboxvlate route as well as geometric parameters for the reactant, transition state, and products. For the reaction via formate intermediate, the carbon atom of CO2 is hydrogenated to generate formate intermediate (IM1). At the first transition state, a hydrogen molecule dissociates, and its bond lengthen from 0.79 to 1.05 Å. The H1 atom moves close to C of the adsorbed CO2 and locates between C on CO2 and H2, at distances of 1.33 and 1.05 Å, respectively. At the same time, the H2 transfers to Pt atom to form Pt-H2 with bond length of 1.84 Å. The calculated activation energy for the formation of the formate functional group (-OOCH) is 1.23 eV, with a single imaginary frequency of 1426.2*i* cm⁻¹. According to TS1, the formate intermediate H-Pt-OOCH (IM1) provides a relative energy of approximately 0.30 eV. The $E_{\rm rel}$ is slightly high with respect to IS1, implying endothermic formate formation step. Next, the H2 transfers to O2 of formate ligand to produce FA through TS2. This step requires energy barrier of 0.72 eV, using single imaginary frequency for transition state of 1022.6i cm⁻¹. At TS2, the distance between formate oxygen atom and H2 on Pt atom shortens from 2.09 to 1.63 Å.

Finally, the FA is formed and adsorbed on the Pt-BV catalyst with an adsorption energy of -0.38 eV. Then, FA is desorbed from the surface by a requirement desorption energy of 0.62 eV. The reaction via carboxylate intermediate is found to be one of possible paths. The H1 hydrogenates to the O1 of CO2 to yield carboxyl ligand (-COOH) with the requirement energy of 0.79 eV. Frequency calculations reveal one imaginary vibrational frequency of 2940.8i cm⁻¹ along with the reaction coordinate. The carboxylate is then formed with the $E_{\rm rel}$ of 0.03 eV, which is more thermodynamically favorable than that of formate formation. The second step of this route is production of FA via hydrogenation of H2 to C of carboxylate ligand. The activation energy of this step is calculated to be 0.19 eV. There is an associated imaginary frequency of 772.4i cm⁻¹ associated with transition state **TS4**, indicating that H2-Pt bond breaking and FA forming happen simultaneously. At TS4, The Pt-H2 and H2-C are 1.71 and 1.69 Å, respectively. Lastly, the FA, called as final product, is then adsorbed on the Pt active site with relative energy of -0.59 eV. The desorption of final product from the catalytic site requires the energy barrier of 0.42 eV. From our investigation, the rate determining step of CO2 hydrogenation through carboxyl intermediate has a small requirement energy of 0.79 eV. By comparison, the reaction via carboxyl intermediate is more feasible rather than via formate intermediate.

3.3.2. CO_2 hydrogenation on Pt-BV via H_2 dissociation and co-adsorption together with H_2 dissociation pathways

According to the previous study, they provided the reaction mechanism for FA production from CO_2 over metal oxide[77], MOFs [14,15], and Cu-Gra [29], starting with H_2 dissociation on the active site ($H_2 \rightarrow 2H^*$) followed by CO_2 hydrogenation ($2H^* + CO_2 \rightarrow HCOOH$). Hence, hydrogen dissociation mechanism is also investigated on Pt-BV surface.

In this section, we proposed two possible reaction pathways, which are H₂ dissociation without CO₂ and with CO₂, namely, H₂ dissociation and co-adsorption together with H₂ dissociation pathways, respectively. Fig. 6 represents the energetic profiles and optimized structures for

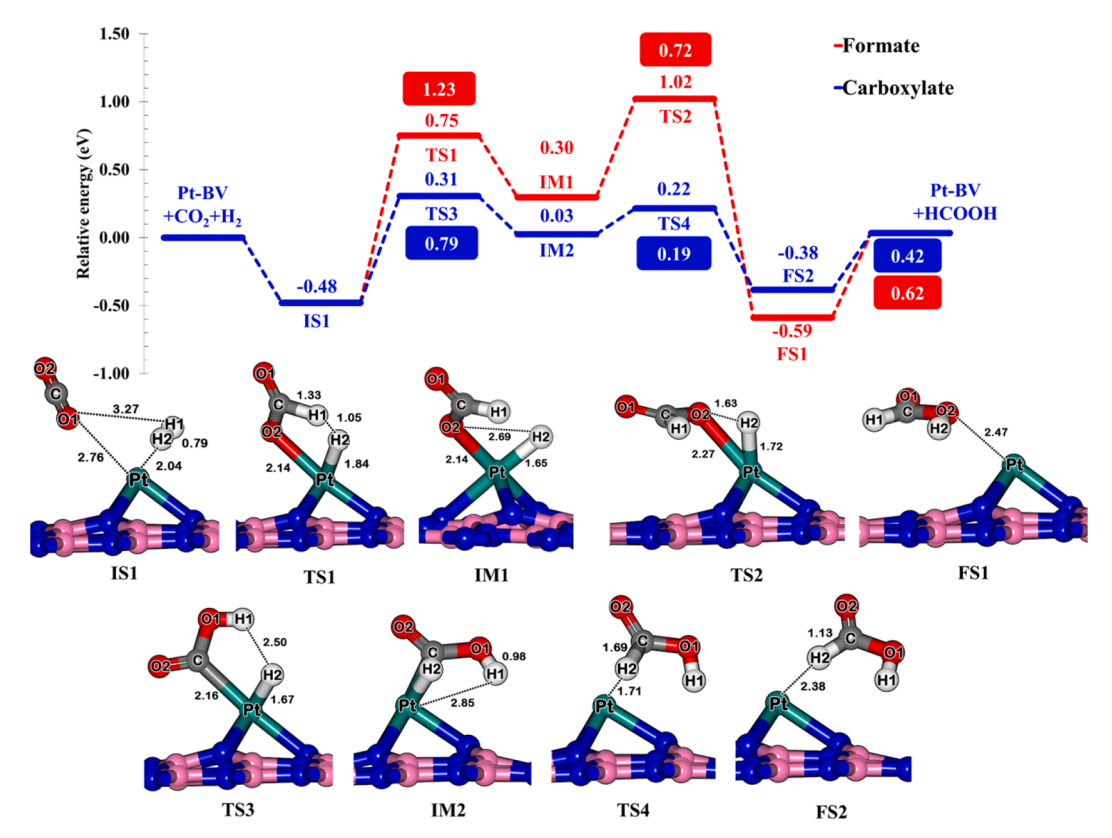


Fig. 5. Energetic profile and optimized structures for reactant, transition state, and product of CO2 hydrogenation via the co-adsorption pathway on Pt-BV.

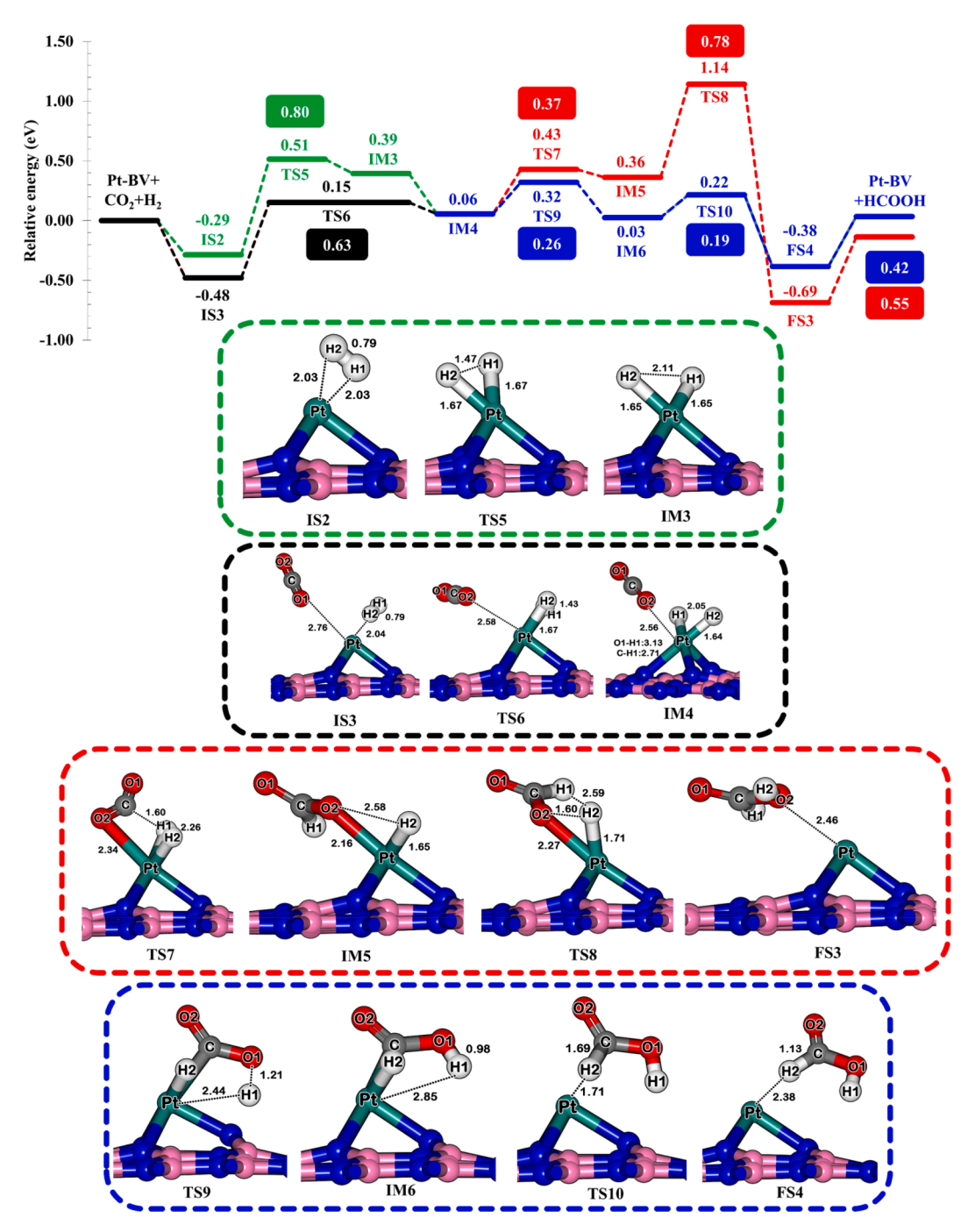


Fig. 6. Energy profile and optimized structures for reactants, transition states, and products in the H₂ dissociation (green line) and co-adsorption together with H₂ dissociation pathways (black line) on Pt-BV. Red and blue lines represent CO₂ hydrogenation via formate and carboxylate pathway, respectively.

reactants, transition states, and products on Pt-BV for all pathways. For the $\rm H_2$ dissociation pathway, the reaction begins with the hydrogen adsorption onto the Pt-BV to form initial state (**IS2**) with the adsorption energy of -0.29 eV, followed by dissociation of $\rm H_2$ into deposited H atoms on the Pt atom. The E_a of molecular $\rm H_2$ separation is 0.80 eV to yield Pt dihydride (**IM3**). At the **TS5**, H1–H2 bond is lengthened from 0.79 to 1.47 Å, which confirmed by one imaginary frequency of 986.0 $^{\rm i}$ cm $^{-1}$. Then, $\rm CO_2$ molecule is sequentially flowed onto the catalyst with the adsorption energy of -0.33 eV. By following the **IM3**, the $\rm CO_2$ adding step attains the relative energy of 0.06 eV. Next, dissociated H then transfers to two targeted sites, which are C and O atom of $\rm CO_2$ molecule to form formate and carboxylate intermediate, respectively. The formation of formate ligand proceeds via Pt–H1 bond breaking along with

C–H1 forming (TS7), with an energy barrier of 0.37 eV and single imaginary frequency of 703.3i cm⁻¹. The relative energy of the formate intermediate (IM5) is 0.36 eV, resulting in slightly high endothermic step. The formate intermediate is further hydrogenated by transferring the H2 to O2 to produce FA. The activation energy has slightly high around 0.78 eV. Finally, the FA is generated and adsorbed on an active Pt site with the $E_{\rm rel}$ of -0.69 eV, indicating a highly exothermic reaction. The desorption of FA requires the energy approximately 0.55 eV. One of possible reaction route is CO₂ hydrogenation via carboxylate intermediate. At the TS9, the hydrogenation to O1 of CO₂ is more likely than C with smaller E_a by 0.11 eV. The TS9 structure is confirmed by single imaginary vibrational frequencies of 697.3i cm⁻¹. After that, the carboxylate intermediate is formed with the $E_{\rm rel}$ of 0.03 eV, implying

that the formation of carboxylate is more favorable rather than it is formate intermediate. To produce the FA, a deposited H2 on Pt moves to C atom to yield adsorbed FA on the catalyst. The H2 locates between Pt and C atom with the bond distance of 1.71 and 1.69 Å, respectively. Remarkably, the activation energy of production FA via carboxylate species is only 0.19 eV, with a single imaginary frequency of 772.4i cm $^{-1}$ corresponding to the H2 movement along the reaction coordinate via H2–Pt bond breaking and H2–C bond forming (see **TS10**). The FA then forms on Pt-BV, with an adsorption energy of –0.38 eV. To refresh the used catalyst, the step of FA desorption needs to be considered. The desorption of from Pt-BV has a requirement energy of 0.42 eV. Thus, CO₂ hydrogenation over a Pt-BV catalyst through a carboxylate intermediate is thermodynamically more favorable than that with a formate intermediate. This summary is in line with the hydrogenation of CO₂ on Pt-Gra [28].

According to reaction mechanism via H₂ dissociation pathway, the rate determining step of this route is the step of hydrogen dissociation with the energy barrier of 0.80 eV, which is slightly higher than the coadsorption pathway (0.79 eV). Therefore, we attempt to decrease the rate determining step by adding CO₂ into the hydrogen dissociation step, called as the co-adsorption together with H₂ dissociation pathway, demonstrating in black line (Fig. 6). Form our results, it is found that the step of H2 dissociated with an adsorbed CO2 molecule can decreased the activation energy from 0.80 to 0.63 eV. This our finding can be explained by PDOS and charge transfers as shown in Fig. 7 and Table 2. We then consider the effect of hydrogen dissociation with CO2 coadsorption in the details. For the hydrogen dissociation step, we found the decreased negative partial charge of hydrogen gas from 0.052e to -0.170e. Therefore, there are electron transfers from a deposited Pt atom to the adsorbed hydrogen gas to generate dihydride-form. When Pt-BV adsorbs CO2 on the catalytic Pt site, the adsorbed CO2 associate hydrogen dissociation step by giving electron to Pt. The Pt atom has become more negative charge by 0.033e, providing that the elongation and dissociation of H-H bonds to form Pt hydride with co-adsorbed CO2

Table 2Charge of the CO₂ hydrogenation on Pt-BV via the H₂ dissociation and coadsorption with H₂ dissociation pathways

Species	Q(eV)					
	Gas molecules		Pt	N1	N2	N3
	H_2	CO_2				
IS2	0.052	-	0.449	-0.220	-0.229	-0.206
TS5	-0.087	-	0.438	-0.178	-0.222	-0.234
IM3	-0.170	-	0.434	-0.170	-0.230	-0.231
IS3	0.042	0.057	0.440	-0.209	-0.240	-0.213
TS6	-0.090	0.086	0.405	-0.239	-0.224	-0.189
IM4	-0.169	0.080	0.411	-0.237	-0.231	-0.182

are stably occurred with the lower relative energy rather than that without CO_2 . From this observation, the Pt atom act as electron reservoirs to achieve electron from CO_2 and pay electron to hydrogen for dissociation. We also confirm the interaction between CO_2 and Pt-BV of all states in the step of hydrogen dissociation by PDOS. It is show that p-orbital of CO_2 continuously hybridize with d-orbital of Pt on BV surface, confirming the stable adsorption in all states. Remarkably, the dissociated H_2 with co-adsorbed CO_2 is preferably found rather than that it is without CO_2 (see Fig. 6). We confirm the stable these configurations by PDOS. For IM4, the hybridization of broadening d-orbital of Pt and s-orbital of hydrogen is found at -6.0 to -2.0 eV, while d-orbital of Pt atom of hydrogen dissociation without CO_2 adsorption (IM3) vanishes at the same range. As a result, it is clear that the presence of CO_2 plays a significant role for the H_2 dissociation to decrease hydrogen dissociation barrier over Pt-BV material.

From these results, we suggest that the production of FA on Pt-BV would occur by adding the $\rm CO_2$ gas in the step of hydrogen dissociation, rather than direct $\rm H_2$ dissociation without $\rm CO_2$ adsorption in this step. The lower activation energy is due mainly to more active Pt in the Pt-BV site for assisting the cleavage of strong H–H bond. After FA is released from the catalyst, the refresh catalyst is prompt to be used as a catalytically active site for hydrogenation of $\rm CO_2$ in the second cycle.

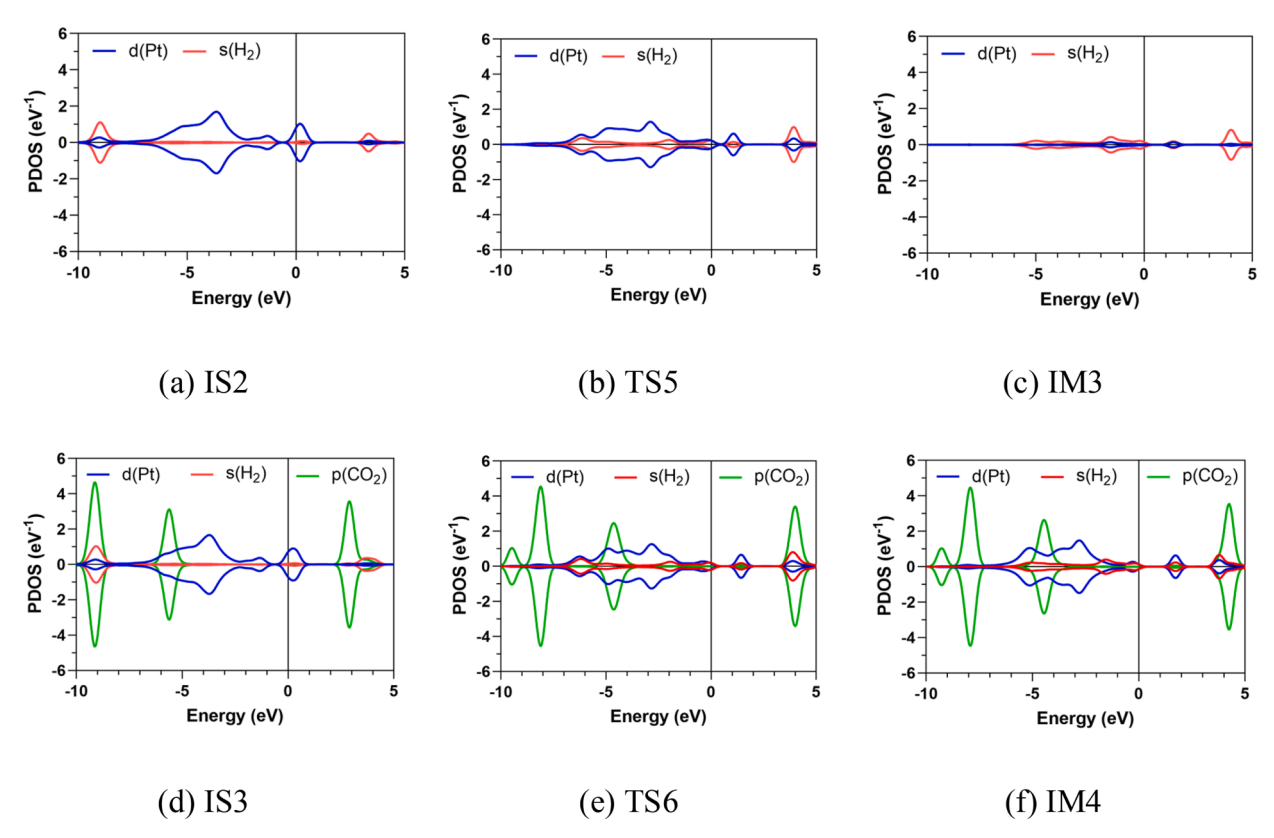


Fig. 7. Partial density of states (PDOS) of (a) IS2, (b) TS5, (c) IM3, (d) IS3, (e) TS6 and (f) IM4 for H2 dissociation and H2 dissociation with CO2 adsorption steps.

Our finding predicts that the appearance of CO_2 at the first step might be helpful for producing FA via CO_2 hydrogenation over Pt-BV. Consequently, the FA production via CO_2 hydrogenation prefers co-adsorption together with H_2 dissociation pathways rather than the others in terms of either kinetically or thermodynamically.

Nowadays, numerous catalysts have been investigated for CO_2 hydrogenation to FA via either formate or carboxylate intermediate. Table 3 lists the rate-determining steps of CO_2 hydrogenation to FA on the various low-cost catalysts. We not only compared the reactivity of metal (Pt, Cu and Ti) but also the effect of the supporter between boron nitride and carbon-based catalyst such a graphene or carbon nanocones. By comparison, our proposed Pt-BV catalysts provide the lowest rate determining step among of the lists via co-adsorption together with H_2 dissociation pathway. Hence, it could be summed up that Pt-BV provides a good candidate catalyst for FA production through CO_2 hydrogenation with kinetically and thermodynamically favorable.

3.4. Microkinetic modelling for CO₂ hydrogenation

We investigated microkinetic simulations to calculate the rates of the reaction via co-adsorption together with H2 dissociation pathways, and to guide the design of the proposed Pt-BV catalysts for optimal condition in practical CO₂ hydrogenation to FA. The temperature effects were also simulated. Fig. 8 shows reaction rates for CO₂ hydrogenation via the formate and carboxylate intermediate routes, as a function of temperature. Corresponding to Figure S4, we found the pressure of maximum production rate and the rate of the reaction is at 5 bar. Then, the rate production and rate of reaction have been calculated in the range of 200-1000 K with a total pressure of 5 bar. From the calculation, the rate production and rates of carboxylate route is much higher than the formate route at temperature around 300-500 K. Therefore, the reaction for FA production through carboxyl intermediate illustrates much greater activity compared to formate intermediate, and so is the dominant reaction mechanism. Furthermore, the optimal temperature for CO₂ hydrogenation via the carboxyl intermediate is approximately 350 K, which are corresponding to previous works [79,80]. and the optimal pressure is only 5 bar that lower than the Pd/g-C₃N₄ (40 bar), [81] metal oxide supported Pd catalysts (14 bar) [80] and PdNi/CNT-GR (50 bar) [82]. Consequently, the CO₂ hydrogenation via carboxylate intermediate is more likely than the formate intermediate through the co-adsorption together with H₂ dissociation pathway.

From our findings, we found three things important that correlated with the experimental data. Firstly, FA can be produced via carboxylate pathway, which corresponding with the other catalysts such as $Pt_n@MIL$, [83] Cu, [84] RhW Nanocrystals [85] and Pt_nCo [86,87] catalysts. Secondly, on carboxylate pathway the RDS is the step of H_2 dissociation. We found the H_2 dissociation via homolytic cleavage and formed hydride species on Pt-BV that the same behavior over the metallic nanoparticles like Pt-BV Rule Pt-BV in the same behavior over the metallic nanoparticles like Pt-BV Rule Pt-BV in the same behavior over the metallic nanoparticles like Pt-BV Rule Pt-BV Rule

optimal condition from microkinetic modelling for CO₂ hydrogenation over Pt-BV at temperature 350K that very close to the CO₂ hydrogenation on Pd-bulk carbon nitride (Pd-BCN) at temperature of 313K [89].

4. Conclusions

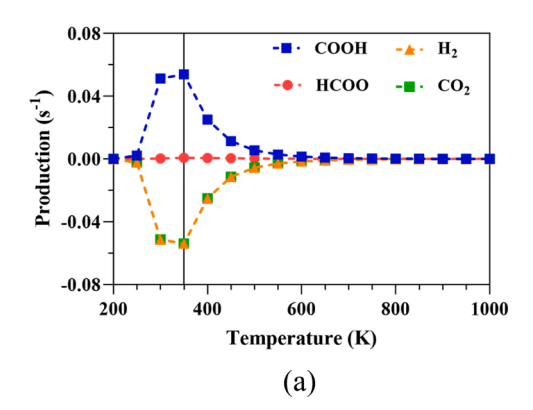
We investigated the reaction mechanism on a single Pt atom decorated on boron vacancy site (Pt-BV) catalyzed CO2 hydrogenation to formic acid by using DFT calculations at the GGA-PBE level of theory. We identified three possible pathways, which are a co-adsorption, a H₂ dissociation and a co-adsorption together with H2 dissociation pathways. The hydrogenation of CO₂ can produce formic acid via either a formate (OOCH) or a carboxylate (COOH) intermediate. The coadsorption with H2 dissociation pathways via carboxylate intermediate on Pt-BV provides the most preferable route with the lowest rate determining step of 0.63 eV. Remarkably, we found that the CO₂ coadsorption play an important role for the hydrogen dissociation step confirmed by PDOS and charge analysis. In addition, microkinetic modelling is also investigated to understand the hydrogenation rate and production rate of the reaction. Form the calculation, the reaction is preferable to proceed via COOH intermediate rather than OOCH species for co-adsorption together with H2 dissociation pathway, and the optimal temperature and pressure for this route are 350 K and 5 bar, respectively. In summary, the proposed theoretical mechanistic insight results for CO₂ hydrogenation on Pt-doped BNNSs is the most agreement with experimental results in terms of not only key intermediate and CO₂/H₂ activation but also the optimal condition for the practical system. Our finding provided theoretical guidelines the design of highlyactive Pt-BV catalysts for the reaction of CO2 hydrogenation, which are involved in the reduction and conversion of greenhouse gases into valuable products (Table 3).

Credit author statement

Yuwanda Injongkol: Data curation, Writing- Original draft

Table 3 The CO_2 hydrogenation to formic acid on various catalysts.

Catalysts	Pathways	Key Intermediate	E _a for RDS (eV)
Pt-BV (this work)	Co-adsorption with H ₂ dissociation	carboxyl	0.63
Pt-doped graphene [28]	Co-adsorption	carboxyl	0.90
Cu-doped graphene [29]	H ₂ dissociation with second H ₂ molecule	formate	0.85
Ti-doped graphene nanoflake [26]	Co-adsorption	formate	0.85
Pt-doped carbon nanocones [78]	H ₂ dissociation with H spillover	formate	0.76



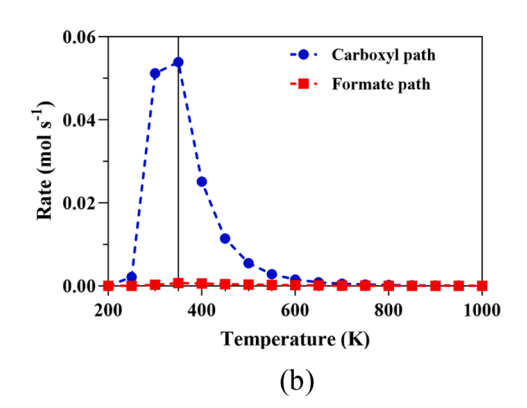


Fig. 8. The (a) production and (b) rate of co-adsorption with H₂ dissociation via formate (HCOO) and carboxylate (COOH) pathways.

preparation. Ratchadaree Intayot: Methodology, Software, Validation. Nuttapon Yodsin: Reviewing and Editing. Alejandro Montoya: Reviewing and Editing. Siriporn Jungsutiwong: Conceptualization, Designing catalyst, Supervision, Writing-Reviewing and Editing.

Declaration of Competing Interest

The authors declare that they have no known competing financial interests or personal relationships that could have appeared to influence the work reported in this paper.

Acknowledgments

The authors are grateful for the financial support received from the Department of Chemistry at Ubon Ratchathani University and Thailand Science Research and Innovation (RSA6280055). Y. I. acknowledges partially financial support from the Royal Golden Jubilee Ph.D. Program (PHD/0187/2559). N. Y. thanks to the Science Achievement Scholarship of Thailand (SAST). The authors also thank The Center of Excellence for Innovation in Chemistry (PERCH-CIC) and the Ministry of Higher Education, Science, Research, and Innovation.

Supplementary materials

Supplementary material associated with this article can be found, in the online version, at doi:10.1016/j.mcat.2021.111675.

References

- [1] A.M. Appel, J.E. Bercaw, A.B. Bocarsly, H. Dobbek, D.L. DuBois, M. Dupuis, J. G. Ferry, E. Fujita, R. Hille, P.J.A. Kenis, C.A. Kerfeld, R.H. Morris, C.H.F. Peden, A. R. Portis, S.W. Ragsdale, T.B. Rauchfuss, J.N.H. Reek, L.C. Seefeldt, R.K. Thauer, G. L. Waldrop, Chem. Rev. 113 (2013) 6621.
- [2] M.Z. Jacobson, J. Geophys. Res. 107 (2002) ACH 16.
- [3] E.V. Kondratenko, G. Mul, J. Baltrusaitis, G.O. Larrazábal, J Pérez-Ramírez, Energy Environ. Sci. 6 (2013) 3112.
- [4] S. Kattel, B. Yan, J.G. Chen, P. Liu, J. Catal. 343 (2016) 115.
- [5] L. Liu, H. Yao, Z. Jiang, T. Fang, Appl. Surf. Sci. 451 (2018) 333.
- [6] A. Behr, K. Nowakowski, Advances in Inorganic Chemistry, 66, Elsevier, 2014, p. 223.
- [7] G.H. Gunasekar, K. Park, K.-D. Jung, S. Yoon, Inorganic Chem. Frontiers 3 (2016) 882.
- [8] J.r. Eppinger, K.-W. Huang, ACS Energy Lett. 2 (2017) 188.
- [9] X. Yu, P.G. Pickup, J. Power Sources 182 (2008) 124.
- [10] B. Chan, L. Radom, J. Am. Chem. Soc. 130 (2008) 9790.
- [11] W. Thongnuam, T. Maihom, S. Choomwattana, Y. Injongkol, B. Boekfa, P. Treesukol, J. Limtrakul, PCCP 20 (2018) 25179.
- [12] T. Maihom, S. Wannakao, B. Boekfa, J Limtrakul, J. Phys. Chem. C 117 (2013) 17650.
- [13] C. Raksakoon, T. Maihom, M. Probst, J. Limtrakul, J. Phys. Chem. C 119 (2015) 3564.
- [14] J. Ye, J.K. Johnson, ACS Catal. 5 (2015) 6219.
- [15] J. Ye, J.K. Johnson, ACS Catal. 5 (2015) 2921.
- [16] C. Hao, S. Wang, M. Li, L. Kang, X. Ma, Catal. Today 160 (2011) 184.
- [17] C. Liu, T.R. Cundari, A.K. Wilson, J. Phys. Chem. C 116 (2012) 5681.
- [18] G. Peng, S. Sibener, G.C. Schatz, S.T. Ceyer, M. Mavrikakis, J. Phys. Chem. C 116 (2012) 3001.
- [19] M. Qiu, H. Tao, Y. Li, Y. Li, K. Ding, X. Huang, W. Chen, Y. Zhang, Appl. Surf. Sci. 427 (2018) 837.
- [20] C. Shi, C.P. O'Grady, A.A. Peterson, H.A. Hansen, J.K. Nørskov, PCCP 15 (2013) 7114.
- [21] S.-T. Zhang, H. Yan, M. Wei, D.G. Evans, X. Duan, RSC Adv. 4 (2014) 30241.
- [22] D.-B. Cao, Y.-W. Li, J. Wang, H. Jiao, Surf. Sci. 603 (2009) 2991.
- [23] X. Jiang, N. Koizumi, X. Guo, C. Song, Appl. Catal. B 170 (2015) 173.
- [24] J. Niu, J. Ran, Z. Ou, X. Du, R. Wang, W. Qi, P. Zhang, J. CO2 Utilization 16 (2016) 431.
- [25] Z. Ou, C. Qin, J. Niu, L. Zhang, J Ran, Int. J. Hydrogen Energy 44 (2019) 819.
- [26] M.D. Esrafili, L. Dinparast, Chem. Phys. Lett. 682 (2017) 49.
- [27] M.D. Esrafili, B. Nejadebrahimi, Appl. Surf. Sci. 475 (2019) 363.
- [28] M.D. Esrafili, F. Sharifi, L. Dinparast, J. Mol. Graph. Model. 77 (2017) 143.
- [29] J. Sirijaraensre, J Limtrakul, Appl. Surf. Sci. 364 (2016) 241.
- [30] B.B. Mulik, B.D. Bankar, A.V. Munde, A.V. Biradar, B.R. Sathe, Chem. Eur. J. 26 (2020) 8801.
- [31] B.B. Mulik, A.V. Munde, B.D. Bankar, A.V. Biradar, B.R. Sathe, Catal. Today (2020).

- [32] A.V. Munde, B.B. Mulik, P.P. Chavan, B.R. Sathe, Electrochim. Acta 349 (2020), 136386
- [33] B.B. Mulik, B.D. Bankar, A.V. Munde, P.P. Chavan, A.V. Biradar, B.R. Sathe, Appl. Surf. Sci. 538 (2021), 148120.
- [34] Q. Cui, G. Qin, W. Wang, L. Sun, A. Du, Q. Sun, Beilstein J. Nanotechnol. 10 (2019) 540.
- [35] M.D. Esrafili, N. Saeidi, Struct. Chem. 27 (2016) 595.
- [36] S. Lin, X. Ye, J. Huang, PCCP 17 (2015) 888.
- [37] S. Lin, X. Ye, R.S. Johnson, H. Guo, J. Phys. Chem. C 117 (2013) 17319.
- [38] X. Liu, T. Duan, C. Meng, Y. Han, RSC Adv. 5 (2015) 10452.
- [39] X. Liu, T. Duan, Y. Sui, C. Meng, Y. Han, RSC Adv. 4 (2014) 38750.
- [40] Z. Lu, P. Lv, J. Xue, H. Wang, Y. Wang, Y. Huang, C. He, D. Ma, Z Yang, RSC Adv. 5 (2015) 84381.
- [41] E.N.C. Paura, da Cunha, W. F., L.F. Roncaratti, J.B. Martins, G.M. Silva, R Gargano, RSC Adv. 5 (2015) 27412.
- [42] J. Zhao, Z Chen, J. Am. Chem. Soc. 139 (2017) 12480.
- [43] W. Zhu, Z. Wu, G.S. Foo, X. Gao, M. Zhou, B. Liu, G.M. Veith, P. Wu, K.L. Browning, H.N. Lee, Nat. Commun. 8 (2017) 1.
- [44] B.R. Sathe, X. Zou, T. Asefa, Catal. Sci. Technol. 4 (2014) 2023.
- [45] E. Ruiz, D. Cillero, P.J. Martínez, Á. Morales, G. San Vicente, G. de Diego, J. M. Sánchez, J. CO2 Utilization 8 (2014) 1.
- [46] N.M. Martin, P. Velin, M. Skoglundh, M. Bauer, P.-A. Carlsson, Catal. Sci. Technol. 7 (2017) 1086.
- [47] Y. Ding, F. Torres-Davila, A. Khater, D. Nash, R. Blair, L. Tetard, MRS Commun. 8 (2018) 1236.
- [48] T. Oku, I. Narita, N. Koi, A. Nishiwaki, K. Suganuma, M. Inoue, K. Hiraga, T. Matsuda, M. Hirabayashi, H. Tokoro, BCN Nanotubes and Related Nanostructures, Springer, 2009, p. 149.
- [49] L. Vel, G. Demazeau, J Etourneau, Mater. Sci. Eng. 10 (1991) 149.
- [50] C. Jin, F. Lin, K. Suenaga, S. Iijima, Phys. Rev. Lett. 102 (2009), 195505.
- [51] W. Sun, Y. Meng, Q. Fu, F. Wang, G. Wang, W. Gao, X. Huang, F. Lu, ACS Appl. Mater. Interfaces 8 (2016) 9881.
- [52] K. Mao, L. Li, W. Zhang, Y. Pei, X.C. Zeng, X. Wu, J Yang, Sci. Rep. 4 (2014) 5441.
- [53] Z. Lu, P. Lv, Z. Yang, S. Li, D. Ma, R. Wu, PCCP 19 (2017) 16795.
- [54] Y. Liu, L.-M. Yang, E. Ganz, Condensed Matter 4 (2019) 65.
- [55] L.-y. Feng, Y.-j. Liu, J.-x. Zhao, J. Power Sources 287 (2015) 431.
 [56] C. Deng, R. He, W. Shen, M. Li, T. Zhang, PCCP 21 (2019) 6900.
- [57] A. Du, Y. Chen, Z. Zhu, R. Amal, G.Q. Lu, S.C. Smith, J. Am. Chem. Soc. 131 (2009)
- [57] A. Du, Y. Chen, Z. Zhu, R. Amai, G.Q. Lu, S.C. Smith, J. Am. Chem. Soc. 131 (2009) 17354.
- [58] X. Tan, H.A. Tahini, H. Arandiyan, S.C. Smith, Adv. Theory Simul. 2 (2019), 1800094.
- [59] B. Delley, J. Chem. Phys. 92 (1990) 508.
- [60] B. Delley, J. Chem. Phys. 113 (2000) 7756.
- [61] J.P. Perdew, K. Burke, M. Ernzerhof, Phys. Rev. Lett. 77 (1996) 3865.
- [62] B. Delley, Phys. Rev. B 66 (2002), 155125.
- [63] W.J. Hehre, Acc. Chem. Res. 9 (1976) 399.
- [64] A. Tkatchenko, M. Scheffler, Phys. Rev. Lett. 102 (2009), 073005.
- [65] F.L. Hirshfeld, Theor. Chim. Acta 44 (1977) 129.
- [66] I.A. Filot, R.A. Van Santen, E.J. Hensen, Angew. Chem. 126 (2014) 12960.
- [67] I.A.W. Filot, E. v. N., R. van den Berg, E.J.M. Hensen.
- [68] P. Nitoń, A. Żywociński, M. Fiałkowski, R. Hołyst, Nanoscale 5 (2013) 9732.
- [69] W. Paszkowicz, J. Pelka, M. Knapp, T. Szyszko, S. Podsiadlo, Appl. Phys. A 75 (2002) 431.
- [70] D. Xu, Y.-j Liu, J.-x Zhao, Q.-h. Cai, X.-z. Wang, J. Phys. Chem. C 118 (2014) 8868.
- [71] G.Y. Gou, B.C. Pan, L. Shi, Phys. Rev. B 76 (2007), 155414.
- [72] M.S. Si, D.S. Xue, Phys. Rev. B 75 (2007), 193409.
- [73] A. Zobelli, C.P. Ewels, A. Gloter, G. Seifert, O. Stephan, S. Csillag, C. Colliex, Nano Lett. 6 (2006) 1955.
- [74] A. Zobelli, A. Gloter, C.P. Ewels, G. Seifert, C. Colliex, Phys. Rev. B 75 (2007), 245402.
- [75] Abdel Aal, S. Surf. Sci. 644 (2016) 1.
- [76] H. Valencia, A. Gil, G. Frapper, J. Phys. Chem. C 119 (2015) 5506.
- [77] B. Qin, S. Li, PCCP 22 (2020) 3390.
- [78] N. Yodsin, C. Rungnim, S. Tungkamani, V. Promarak, S. Namuangruk, S. Jungsuttiwong, J. Phys. Chem. C 124 (2020) 1941.
- [79] S. Moret, P.J. Dyson, G. Laurenczy, Nat. Commun. 5 (2014) 4017.
- [80] Z. Zhang, L. Zhang, S. Yao, X. Song, W. Huang, M.J. Hülsey, N. Yan, J. Catal. 376 (2019) 57.
- [81] J.H. Lee, J. Ryu, J.Y. Kim, S.-W. Nam, J.H. Han, T.-H. Lim, S. Gautam, K.H. Chae, C.W. Yoon, J. Mater. Chem. A 2 (2014) 9490.
- [82] L.T.M. Nguyen, H. Park, M. Banu, J.Y. Kim, D.H. Youn, G. Magesh, W.Y. Kim, J. S Lee, RSC Adv. 5 (2015), 105560.
- [83] Y. Chen, H. Li, W. Zhao, W. Zhang, J. Li, W. Li, X. Zheng, W. Yan, W. Zhang, J. Zhu, Nat. Commun. 10 (2019) 1.
- [84] Y. Yang, C.A. Mims, D. Mei, C.H. Peden, C.T. Campbell, J. Catal. 298 (2013) 10.
- [85] W. Zhang, L. Wang, H. Liu, Y. Hao, H. Li, M.U. Khan, J. Zeng, Nano Lett. 17 (2017) 788
- [86] M.U. Khan, L. Wang, Z. Liu, Z. Gao, S. Wang, H. Li, W. Zhang, M. Wang, Z. Wang, C. Ma, Angew. Chem. Int. Ed. 55 (2016) 9548.
- [87] S. Bai, Q. Shao, Y. Feng, L. Bu, X. Huang, Small 13 (2017), 1604311.
- [88] L. Zhang, M. Zhou, A. Wang, T. Zhang, Chem. Rev. 120 (2019) 683.
- [89] C. Mondelli, B. Puértolas, M. Ackermann, Z. Chen, J Pérez-Ramírez, ChemSusChem 11 (2018) 2859.